SOLIDIFICATION AND MICROSTRUCTURE-MECHANICAL BEHAVIOR OF Al-Si-Mg(Cu) ALLOYS WITH Ti, Zr, V, Cr, and Cu ADDITIVES

LAURA WAMBANI SIMIYU

MASTER OF SCIENCE

(Mechanical Engineering)

JOMO KENYATTA UNIVERSITY OF AGRICULTURE AND TECHNOLOGY

2019

Solidification and Microstructure-Mechanical Behavior of Al-Si-Mg(Cu) Alloys with Ti, Zr, V, Cr and Cu Additives

Laura Wambani Simiyu

A thesis submitted in partial fulfillment for the degree of Master of Science in Mechanical Engineering in the Jomo Kenyatta University of Agriculture and Technology

2019

DECLARATION

This thesis is my original work and has not been presented for a degree in any other University.

Signature..... Date.....

Laura Wambani Simiyu

This thesis has been submitted for examination with our approval as the University Supervisors

Signature..... Date.....

Dr. Bruno R. Mose, PhD

JKUAT, Kenya

Signature..... Date.....

Dr. Thomas O. Mbuya, PhD

University of Nairobi, Kenya

Signature..... Date.....

Eng. Prof. Stephen M.Maranga, PhD

JKUAT, Kenya

DEDICATION

To my loving husband, Calvine

&

my beloved parents Mr. Ndombi Simiyu and Mrs. Violet Nabangala Simiyu

ACKNOWLEDGEMENTS

Very importantly, I am grateful to God for this research work which was a journey full of learning and problem solving. This research would have been impossible without the invaluable efforts of the following:

My supervisors Dr. Mbuya, Dr. Bruno and Prof. Maranga for their advice and direction during the entire research period. Their interaction with me made it possible for me to understand research in a broader sense. I thank Jomo Kenyatta University of Agriculture and Technology (JKUAT) for paying for the MSc sponsorship that included fees and research funding support. National Research Fund (NRF) also provided additional funding to support this project to completion. To Dr. Ing. Mile Djurdjevic of Nemak Company in Austria for his guidance on thermal analysis experiments. I extend my gratitude to the Department of Mechanical and Manufacturing Engineering, University of Nairobi (UoN) for allowing me to use their laboratory facilities. Mr. Mwai at the foundry workshop at JKUAT for provided support during thermal analysis experiments. Eng. Aduol, Jackton, Njogu, Macharia and Jackline were all helpful to me while conducting my experiments at UoN. Finally, I thank my husband, parents, siblings, my friend Cynthia Mulaku, and my colleagues for their prayers and support.

TABLE OF CONTENTS

LIST OF TABLES

LIST OF FIGURES

LIST OF APPENDICES

LIST OF ABBREVIATIONS

AR	Aspect ratio
BSE	Backscattered electron
CR	Cooling rate
CCA	Cooling curve analysis
DAS	Dendrite arm spacing
DCP	Dendrite coherency point
DCT	Dendrite coherency temperature
EDS	Energy dispersive spectroscopy
FCC	Face centered cubic
HIP	Hot isostatic pressing
HT	High temperature
NMC	Numerical Machining Complex
OES	Optical emission spectroscopy
OM	Optical microscopy
OPS	Oxide particle suspension
PM	Permanent mold
RT	Room temperature
SDAS	Secondary dendrite arm spacing
SE	Secondary electron
SEM	Scanning electron microscopy
TA	Thermal analysis
UTS	Ultimate tensile strength
YS	Yield strength

LIST OF NOMENCLATURES

α	Alpha phase
β	Beta phase
D_{eq}	Equivalent diameter
T	Temperature (^{o}C)
t	Time (seconds)
T_c	Centre thermocouple temperature (^{o}C)
T_w	Near-wall thermocouple temperature (^{o}C)
$\triangle$T	T_w– T_c (^{o}C)
wt.%	Weight percent
θ	Theta
El%	Percentage elongation

ABSTRACT

Most secondary aluminium alloys have varying chemical compositions due to presence of various elements that are added deliberately (such as through alloying) and or accidentally (such as through tools or equipment used). The desirable or undesirable effects of these elements make it inevitable to determine how secondary alloy properties are affected by their individual and combined additions. It is through such researches that secondary aluminium alloys, characterized by light weight, excellent castability and formability, and recyclability, can also be considered the de-facto standard for the manufacture of premium components. In this research, the effect of some transition elements on the mechanical performance (Ti, Zr, V and Cr)and the solidification characteristics (Ti, Zr, V, Cr and Cu) of 356 Al-Si alloys that are HIPed and T6 heat treated and as-cast respectively are investigated. The base alloy, alloy 356, was developed followed by preparation of five of its variants through adjustment of transition elements, whose effects were under investigation. The alloy variants were named 356X, 356XCr, 356X0.5Cu, 356X3.5CuCr, and 356TiSr based on their chemical composition. X denoted 0.15%Ti + 0.15%Zr + 0.25%V + 0.015%Sr, Cr $\equiv$ 0.15%Cr and TiSr = 0.15%Ti + 0.015%Sr. The tests performed were: microscopy (optical and scanning electron microscopy), thermal analysis, fatigue, and tensile. Microscopy was used to: identify the best statistical probability plots for the alloys' particle area, determine the relationship between various particle shapes characteristics and in the prediction of microstructure-mechanical performance properties on combined addition of some transition elements to alloy 356. Microcopy tests revealed that (AlSi)x(TiZr)Fe intermetallics together with other phases containing Zr, Ti, V, Zr, and Cu additives were present. Fractography conducted on tensile specimens showed that fracture occured in a brittle-ductile manner as characterized by occurence of both dimples and cracked intermetallics. It was clear that the 3-parameter Lognormal plot gave the best distribution plot both for the entire particle area and for 0.1% of the largest particle areas. Quantitative microscopy revealed that: the relationship between maximum Feret dimensions and deq is not perfectly linear, a strong correlation existed between circularity and maximum Feret dimension/or area and that aspect ratio and maximum Feret dimension/or area had no clear relationship. These microscopy results can help in the prediction of future related properties. Thermal analysis tests were conducted on all the six alloys at a cooling rate of 0.87 ^{o}C/s so as to identify solidification characteristics of the alloys (α-Al, DCT, Al-Si, Al-Si-Cu and solidus temperatures). The range of these temperatures was typical to most 356 alloys. It was also evident that X and ZrV additions decreased solidus temperatures while all other additions (XCr, TiSr, X0.5CuCr and X3.5CuCr) increased it. Also, X, ZrV and TiSr decreased α-Al nucleation temperature and DCT with the decrease by X being greatest followed by ZrV and finally TiSr. XCr increased: α-Al nucleation temperature, Al-Si and solidus temperatures while X+Cu+Cr addition decreased DCT with a higher decrease registered at lower Cu contents. From these results, optimum process temperatures such as solution heat treatment temperatures (500 ^{o}C) and

pouring temperatures informed by start of solidification temperatures were recommended. Fatigue and tensile tests were also conducted on alloys 356, 356X and 356XCr at room (25 °C) and at both room and high (237 °C) temperature respectively. Fatigue strengths were obtained at 10^7 cycles (60 Hz and R = -1). High fatigue strengths obtained (>65 MPa) were associated with hipping, heat treatment, grain refinement, modification and alloying using strength forming precipitates such as Cr-related ones in α-Al matrix. Generally, addition of XCr to 356 improved tensile and fatigue performance of 356 alloys than TiSr or sole X. X addition to alloy 356 was considered unfavourable for cases where high ductility is a prerequisite while XCr was termed unsuitable for high temperature elongation applications. Lastly, X and XCr additions would be ideal for high strength applications both at room temperature and at 237 °C. From these tensile and fatigue test results, efficient designs can be made out of alloys with a similar chemical composition to those investigated. Overall, this research contributes to thermal analysis softwares by providing data specific to the tested set of alloys whose composition has not been tested before. Additionally, it also gives tensile and fatigue performance of unique alloy-compositions, as far as the intentional combination and quantities of Ti, Zr, V, and Cr are concerned. This research thus adds to the body of knowledge.

CHAPTER ONE

INTRODUCTION

1.1 Background

Alloying is widely used in industries to improve the inferior properties of materials or to maintain good properties at desired working conditions while ensuring proper quality and functionality at a reasonable cost. Of all the commonly applied commercial foundry alloys, aluminium alloys are fast-paced at becoming the most universally acceptable and prominent alloys with Al-Si alloys being at the forefront. They are taking the lead among the commercial aluminium foundry alloys because they possess many desirable properties among which are: high corrosion resistance, excellent castability, low thermal expansion, excellent thermal conductivity, high strength to weight ratio, good wear resistance, recyclability and are relatively inexpensive (Tillova, Chalupova, & Hurtalova, 2012; Jana, Mishra, Baumann, & Grant, 2009). For these reasons, they are applicable in the automotive, aerospace and general engineering application industries (Tillova et al.; Nicoletto, Anzelotti, & Konecna; Mattos, Uehara, Sato, & Ferreira, 2010).

Much as Al-Si alloys have acquired increased significance owing to their desirable properties, a consequence of which is their wide range of applications, they have several disadvantages. These include but are not limited to: low reliability due to varied fatigue strength and tensile properties (Tagirov, Lashina, & Kaibyshev, 2012) due to inherent casting defects such as pores and inclusions and softening at high temperatures leading to deteriorated mechanical properties hence limited working temperature ranges.

Recycling of aluminium alloys has been on a global increase due to the numerous advantages associated with it such as: 1.) Energy saving by taking a shorter route to obtain aluminium alloys rather than going all the way from ore extraction to the desired alloy chemistry and 2.) Reduced pollution and greenhouse emissions from disposal and extraction respectively. However, recycling is faced with many challenges including insufficient knowledge on the effect of transition elements on properties of specific Al-Si alloy compositions.

Some power train components operating at elevated temperatures are made of Al-Si alloys. The present world seeks ways and means of reducing vehicle emissions and increasing fuel efficiency. Fuel efficiency can be improved by reducing

the overall mass of the vehicle such as by using lightweight alloys for automotive components and by applying better processing and manufacturing technologies. These approaches are expected to lead to high strength light weight components. However, as earlier mentioned, these alloys are characterized by a decrease in strength above 200°C as a result of coarsening and dissolving of strengthening precipitates. With this detriment to performance, these alloys find limited application in premium components. To curb this problem, there have been efforts to improve the properties of these alloys through development of new alloys with high thermal performance and through modification of existing alloys such as 319 and 356. For instance, the most prominent approach has been through addition of nickel though nickel is expensive (Lee & Chen, 2005). There is an attempt to substitute Ni with other less costly transition elements such as Zr, V and Ti. These form high temperature strengthening intermetallic phases.

1.2 Problem statement

There is an increasing demand for high performance passenger automotive engines. This has prompted the need for continuous research and development of improved cast aluminium alloys for power-train components that possess desirable properties such as high fatigue and tensile performance both at room and high temperature. Transition elements are often added to cast Al-Si alloys to improve their high temperature performance. There is published data on the effects of some elements such as Ti, Zr and Cu on recycled Al-Si alloy microstructure and mechanical properties. However, the effectiveness of adding these elements in improving high and low temperature properties and processing conditions, is not well understood (Jovid, Timelli, & Bonollo, 2016; Rana, Purohit, & Das, 2012. This is mainly due to insufficient knowledge on casting, optimal alloy chemistry and heat treatment parameters necessary to ensure precipitation of sufficient quantities of high temperature stable precipitates. The increasing need for aluminium recycling also implies a likely increase in the uptake of secondary cast aluminium alloys in automotive applications. These alloys inherently possess higher impurity levels that are likely to influence solidification characteristics, microstructure and mechanical properties. Therefore, there is need to optimize alloying additions and heat treatment parameters or casting temperatures of Al-Si alloys for desired microstructure-property relationships for specific applications.

1.3 Justification of the study

Most premium quality products are not manufactured from secondary alloys and this has been attributed to the high impurity levels in these alloys which detrimentally affect alloy properties. Their levels in these alloys therefore need to be closely investigated so that optimal additions of their sole and combined additions lead to better microstructure-property development. Therefore, the effects of addition elements cannot be overlooked since this is a fundamental aspect in performance of any alloy. Additionally, research has shown that in 2015, aluminium scrap from Nairobi, Mombasa and Nakuru was at 37.3% with the rest constituting extruded and rolled scrap (Wangombe, Maranga, Mose, & Mbuya, 2017). However, only 31.6% of the cast scrap is being consumed with the rest being exported without value addition. Existence of these high levels of cast aluminium alloys in Kenyan prompts the need to fully utilize these alloys for better economical use in an attempt to meet the market needs.

Recycling has many associated advantages making secondary Al-Si alloys a good choice for component manufacturing. However, most Al-Si alloys cannot operate at elevated temperatures since high temperature exposure leads to coarsening of microstructural constituents leading to lowered mechanical performance. Since most powertrain components need to operate optimally at both room and high temperature, there is need to develop alloys that suit this function and are cost effective. This research therefore involves tests to demonstrate the combined effects of Ti, Zr, V, Cr and Cu alloying additions on 356 alloys. This is especially so with regard to solidification characteristics (for as-cast alloys) and both low and high temperature mechanical application (for those that have undergone hot isostatic pressing (HIP) and T6 heat treating). From this study therefore, an analysis of the performance of developed Al-Si-Mg(Cu) alloys, that are cost effective, for operation at both room and elevated temperature will be provided. The results will offer useful information to predict microstructural-mechanical performance and solidification behavior of similar alloys.

1.4 Objectives of the study

1.4.1 Main objective

This work aims at characterizing the effect of Ti, Zr, V, Cr and Cu on 356-type secondary cast Al-Si alloys for room and high temperature load bearing applications.

1.4.2 Specific objectives

The specific objectives were:

1.) To establish the effect of transition elements on the microstructure evolution during solidification of 356-type secondary alloys using thermal analysis

2.) To characterize the effect of transition elements on the type and properties of microstructure features of the 356-type secondary alloys

3.) To evaluate the effect of transition elements on the tensile and fatigue performance of the 356-type secondary alloys

1.5 Thesis outline

Chapter one describes the research title and provides details of the research work. Chapter two briefly reviews the literature in the areas of study i.e. microstructure of 356-type cast aluminium alloys, thermal analysis, heat treatment and a summary at the end. Chapter 3 describes the methods used to obtain results and Chapter 4 present the results and discussions in relation to available literature and the actual alloys tested. Chapter 5 gives the conclusions of the findings and recommendations for future studies. This is then followed by a reference list and finally the Appendices.

CHAPTER TWO

LITERATURE REVIEW

2.1 Introduction

This section covers a brief review of various topics relevant to cast 356-type aluminium alloys. More specifically, it touches on microstructure, thermal analysis, heat treatment and tensile performance. Finally, a summary of the literature review is provided at the end of the chapter.

2.2 Microstructure of 356-Type Cast Aluminium Alloys

2.2.1 The 356 Cast Aluminium Alloy

This is a cast aluminium alloy based on the Al-Si binary system (Fig. 2.1 - Mazahery and Shabani, 2014) with a hypoeutectic silicon composition of ∼7 wt.% and a magnesium content of ∼0.3 - 0.5 wt.% (Davis, 1993). The typical microstructure of this alloy contains the α-Al primary dendrites, which is a solid solution of aluminium with dissolved Si (1.65 %), Mg (∼14.9 %), and other minor or impurity elements such as Ti, for grain refinement, and Sr, for silicon particle size and shape modification, (Hatch, 1984).

The α-Al primary dendrites may also contain various elements in the form of nanoscale particles that are precipitated either during solidification or during subsequent heat treatment (Elhadari, Patel, Chen & Kasprzak, 2011). The type, size, and amount of these particles present depend on the chemical composition of the alloy, solidification conditions, and heat treatment.

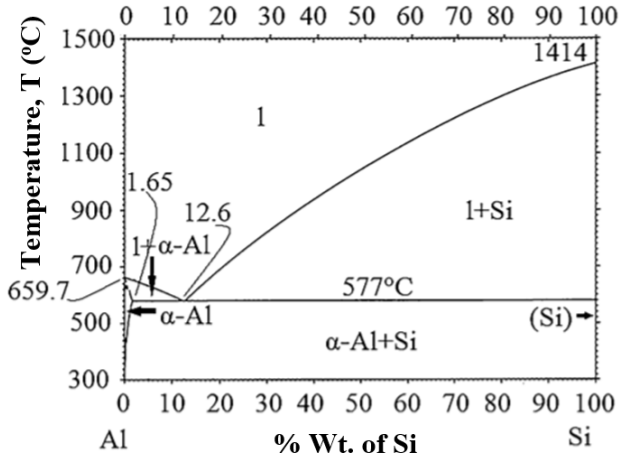

Figure 2.1: Binary Al-Si phase diagram (Mazahery & Shabani, 2014)

In addition to the α-Al primary dendrites, the microstructure of 356-type al-

loys typically contain eutectic silicon particles and various types of intermetallic compounds that form during solidification. These phases form during the later stages of solidification and are therefore segregated to the regions in between the α-Al dendrites (Javidani & Larouche, 2014). Micrographs showing the typical microstructure of Sr-modified and T6 heat treated A356 and A357 alloys solidified at a cooling rate of 0.2 °C/s are shown in Fig. 2.2 (β is the Al_5FeSi phase and π is the $Al_9FeMg_3Si_5$ phase) (Wang & Davidson, 2001).

Silicon is the main alloying element in these alloys and appears as brittle acicular platelets in the as-cast unmodified state. Iron impurities result in the formation of intermetallics such as β-Al_5FeSi with a platelet morphology and π-$Al_8Mg_3FeSi_6$ (in the presence of higher levels of Mg) and α-$Al_{15}Fe_3Si_2$ with Chinese script morphology (Mbuya, 2003). The π phase sometimes occurs in the non-stoichiometric form such as the $Al_9FeMg_3Si_5$ phase shown in Fig. 2.2 (Wang & Davidson, 2001). Addition of Cu to Al-Si-Mg alloys leads to formation of Cu-containing phases such as blocky or eutectic Al_2Cu particles during solidification. Upon heat treatment of Al-Si alloys in the presence of Cu and Mg, strengthening precipitates such as β'-Mg_2Si (or β"-Mg_2Si), θ'-Al_2Cu, S'-Al_2CuMg or Q-$Al_4Cu_2Mg_8Si_7$ phases form. However, these precipitates tend to coarsen rapidly when the material is held for long at high temperatures leading to the formation of non-coherent phases such as θ-Al_2Cu, β-Mg_2Si and S-Al_2CuMg (Mbuya, 2011). The cooling rate has a marked effect on the size, morphology and distribution of all microstructural constituents. For example, a fast cooling rate is associated with refined microstructural features, decreased size of intermetallics, and secondary dendrite arm spacing (SDAS), and changed Si eutectic morphology from large and elongated plates to small and rounded Si particles (Mbuya, 2011).

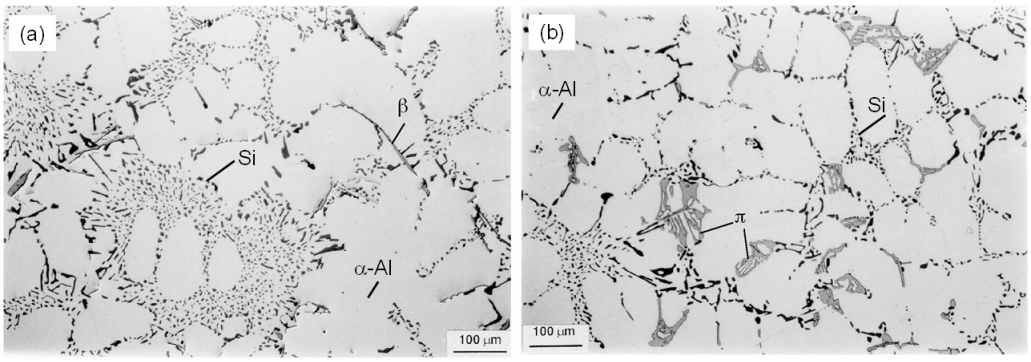

Figure 2.2: Typical microstructures of Sr-modified and T6 treated: (a) A356 and (b) A357 (Wang & Davidson, 2001)

2.2.2 Modification of 356-Type Cast Aluminium Alloys

The coarse acicular Si particles are undesirable in these alloys because their platelet morphology causes stress concentration that leads to crack initiation. To transform this Si morphology to a fine fibrous or globular form, rapid cooling, heat treatment, mould vibration, melt agitation, and use of modifying agents such as Sr, Sb, Sc, Na, and Ca can be used (Rao, Murty, Das & Chakraborty, 2008). Addition of Sr is the most popular industrial technique used for modification followed by rapid cooling where possible. Fig. 2.3 shows the effect of Sr (300 ppm Sr) and Sb (2400 ppm Sb) on hypoeutectic Al-Si alloys (Miresmaeili, Campbell, Shabestari & Boutorabi, 2005).

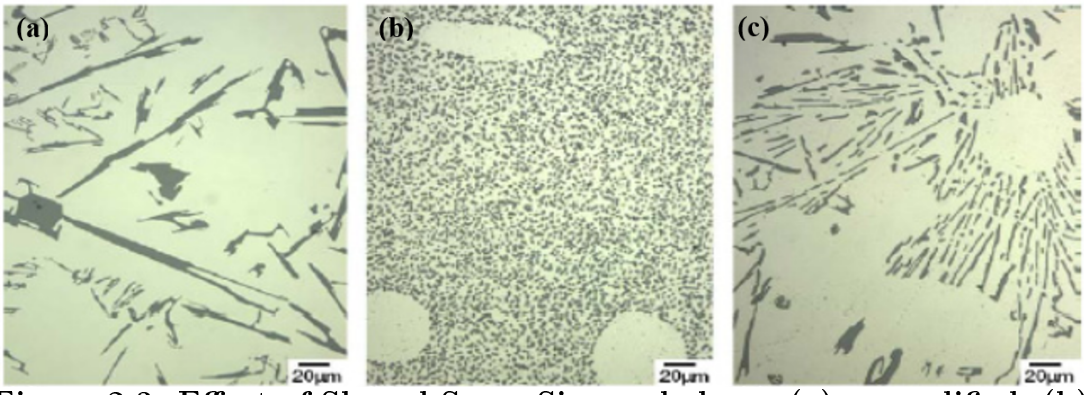

Figure 2.3: Effect of Sb and Sr on Si morphology: (a) unmodified; (b) Sr-modified; and (c) Sb-modified hypoeutectic Al-Si alloys (Miresmaeili, Campbell, Shabestari & Boutorabi, 2005)

Strontium is added to Al-7Si alloys in form of Al-Sr or Al-Si-Sr master alloys and most researchers concur that 0.015 % Sr addition leads to a desired fine fibrous Si structure (Davis, 1993). However, the optimum addition level can be varied depending on the alloy composition. For example, presence of P, Bi, Sb, and Mg can nullify the modifying effect of Sr. Additionally, Mose (2009) noted that refinement of the Al-Si eutectic phase by Sr additions above the optimum may result in increased microporosity. Metallographic studies, thermal analysis (TA), and alloy physical properties can assess the level of modification (Zamani, 2015).

2.2.3 Grain Refinement of 356-Type Cast Aluminium Alloys

Metals and alloys typically solidify with a coarse columnar grain structure but to achieve high strength, fine equiaxed grains are desired as enshrined in the Hall-Petch equation. Grain refinement is associated with an altered casting morphol-

ogy composed of a uniform distribution of second phases and well redistributed micropores in small amounts and sizes (Cordero, Knight & Schuh, 2016). It also improves feeding by delaying the onset of dendrite coherency. Methods of obtaining fine equiaxed grains in Al-Si alloys include rapid cooling rate, melt agitations during solidification, and use of chemical grain refining agents (Murty, Kori & Chakraborty, 2002). The major approach for refining grains is based on heterogeneous nucleation whereby foreign particles form nucleation sites then grain growth proceeds slowly in the melt.

Fig. 2.4 shows microstructural effects of grain refinement on aluminium (0.01 %Ti) (Murty, Kori & Chakraborty, 2002). Grain refinement using inoculants is achieved with the use of elements such as B, Ti, Zr, Nb, V, W, Ta, and Ce. Boron was reported by Sigworth and Kuhn (2007), to be a better refiner than Ti, which is more effective than Zr and V, since it produces an efficient AlB_2 nucleus. However, it dissolves readily in Al leading to its reaction with Sr and this limits the modification efficiency of Sr. On the other hand, when Ti is added in excess of 0.10 % in 356 alloys for prolonged periods, it may form insoluble $Ti(Al,Si)_3$ crystals sludge in holding furnaces. Murty, Kori & Chakraborty, 2002 reported that Al-Ti-Si and Al-Ti-Be had a lower grain refining efficiency than Al-Ti-B which was comparable to Al-Ti-C but more efficient than binary Al-Ti. However, Al-Ti-C based grain refiners become particularly useful when the presence of Boron, in forms such as TiB_2, is undesirable (Murty, Kori & Chakraborty, 2002). Al-Ti-B based grain refinement master alloys have gained wide acceptance with Al-5 %Ti-1 %B being the most popular due to its excellent refining capability.

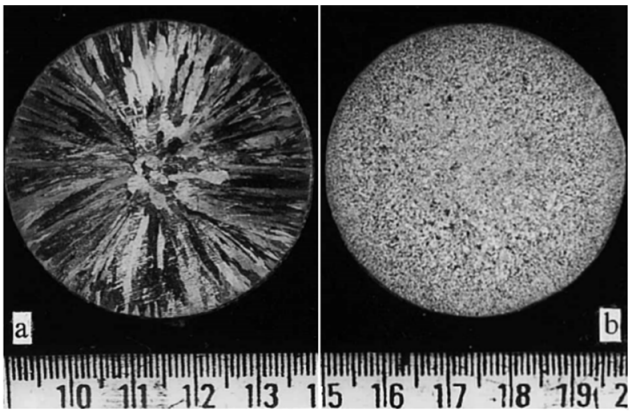

Figure 2.4: Macrographs of aluminium showing; (a) unrefined coarse columnar grains (b) grain refined fine equiaxed grains (Murty, Kori & Chakraborty, 2002)

2.2.4 Effect of additives on 356-Type Cast Alloys' Microstructure

a) Effect of Fe, Mn and Cr

Iron levels increase from ∼0.1 % in primary alloys up to 1 % or more in secondary cast Al-Si alloys. When present, Fe leads to the formation of various iron-bearing intermetallic phases; β-Al_5FeSi, π-$Al_8Mg_3FeSi_6$, α-Al_8Fe_2Si and δ-Al_4FeSi (Javidani & Larouche, 2014; Mbuya et al., 2003). Some of these are shown in Fig. 2.5 (Gustafsson, Thorvaldsson & Dunlop, 1986). β-Al_5FeSi phase possesses a platelet morphology (Svensson & Seifeddine, 2009) unlike π-$Al_8Mg_3FeSi_6$ and α-Al_8Fe_2Si phases that possess Chinese script morphology. β-phase seems stable at low Mg containing 356 alloys while the π-phase is stable in high Mg containing 357 alloys. However, π-phase dissolves in 356 alloys and is considered less harmful than in 357 alloys where it does not dissolve, forming $Al_{10}FeMg_4Si_4$ phase (Wang & Davidson, 2001). The quantity of Fe-phases, particularly β-phase, increases with Fe content while their morphology depends on: alloy composition, solidification rate, and heat treatment. Javidani & Larouche (2014), reported that optimal additions of Mn, Cr and Ni chemical modifiers, high solidification rate, and melt superheating promoted formation of the α-iron phase whereas a low Mn and Cr concentration at a low cooling rate of ∼0.8K/s favored crystallization of the β-phase. Insoluble Fe-phases such as Al_3Fe, Al_6FeMn, and α-$Al_{15}FeSi$ are essentially thermally stable which imparts high temperature strength (Long, Chen, Liu, Li & Li, 2013). However, AlFeSi intermetallics do not offer positive strengthening on mechanical properties at room temperature in Al-Si alloys due to their adverse effects on casting considerations including: flowability and feeding. Consequently, they cause excessive shrinkage porosity since they may serve as effective pore nucleation sites, depending on their size and cooling rate employed (Tillova et al., 2012). Fig. 2.6 shows shrinkage pores due to β-Fe phase blockage during metal feeding (Genualdi, 2001).

It was reported by Mbuya et al. (2003), that iron also played a role in grain refinement in that: at low concentrations it contributes to the growth restriction factor by cooperating with other elements in promoting grain refinement. Additionally, it ameliorates the poisoning effect of Zr on grain refinement by Al-5Ti-1B master alloy at concentrations of about 0.1 %. However, at higher concentrations it hinders grain refinement by Al-5Ti-1B master alloy and when individually used for grain refinement it fades fast on holding.

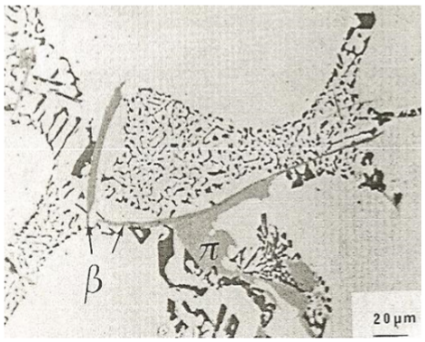

Figure 2.5: β-Al_5FeSi and π-$Al_8Mg_3FeSi_6$ Fe-phases in as-cast Al-7Si-0.3Mg-0.52Fe alloy (Gustafsson et al., 1986)

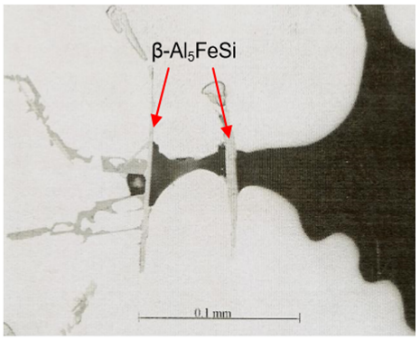

Figure 2.6: Shrinkage porosity due to blockage by β-Al_5FeSi phase (Genualdi, 2001)

The effects of β-Al_5FeSi particles can be suppressed by addition of Cr, V, Ni, Sr, Mn, Be, Co, Mo, Cu or rare earth elements such as La and Ce. A ratio of 2:1 for Fe:Mn is the most prominent for this purpose since it promotes formation of less harmful α-Fe Chinese script phases such as α-$Al_{15}(FeMn)_3Si_2$ and α-$Al_{13}(Fe,Mn)_4Si_2$ (Tillova et al., 2012). It was also reported (Kim, Park, Han & Lee, 2006) that combined Mn and Cr addition was more effective in modification of the β-phase. This was because it led to precipitation of α-Al(Mn,Cr,Fe)Si nanoparticles in the microstructure of A356 Al alloy. However, Javidani and Larouche (2014), reported that an undesirable amount of Mn in AlSiCu/Mg alloy may lead to precipitation of Al-Cu-Mn particles (T-$Al_{20}Cu_2Mn_3$ phase) during solution heat treatment that decreased the Cu content in the α-Al matrix.

Acceptable Cr addition levels to Al-7Si-0.3Mg are usually less than 0.35 % above which it forms coarse constituents with other additions such as Mn and Ti (Rambabu, Prasad & Kutumbarao, 2017). Cr addition is known to modify β-Al_5FeSi platelet inclusions to α-$Al_{13}(Fe,Cr)_4Si_4$ fish-bone like phase and is also more effective in decreasing the volume fraction of β-phases and increasing α-phases than Mn (Yang et al., 2015. Coarse π-$Al_8Mg_3FeSi_6$ phase particles and the fine α-(bcc)

precipitates (i.e., α-Al(Fe,Cr)Si phase) may also result when 0.002 - 0.35 % Cr exists in A356 alloys. Excess additions of Mn and Cr can lead to formation of hard intermetallic phases such as $Al_{15}(FeMnCr)_3Si_2$ which can form sludge that adversely affect casting properties (Tillova, 2012).

Combined addition of Fe, Mn and Cr to Al-Si alloys offers high temperature properties in Al-Si piston alloys by forming thermally-stable phases. This is preferred to the high-cost of traditionally used Ni (Li, Yang, Wu, Wei & Liu, 2011).

b) Effect of Ti, Cu, Zr, and V

Conventionally, Ti acts as a grain refiner in as cast Al-Si alloys through formation of potent nucleant particles (e.g., TiB_2, and $TiAl_3$) and providing the required solute to promote heterogeneous nucleation of primary Al dendrite grains. When solely used, effect of Ti as a grain refiner decreases with holding time in molten state and with remelting but its effect is enhanced in the presence of Boron or when added as a combination of Boron such as TiB_2 (Rambabu, 2017). While addition of 0.015 % Ti is effective for grain refinement of 356 alloys (Majed & Torbjorn, 2005), addition of higher levels of Ti (e.g., up to 4 % Ti) leads to precipitation of large Al_3Ti and TiAlSi intermetallic particles (Saheb et al., 2001). Ti addition (up to 0.2 %) to an Al-6.5Si-0.44Mg-0.9Cu alloy (T6) also promotes formation of finer and denser θ' phases (Choi, Cho & Kumai, 2016).

The addition of Cu leads to solidification of Copper-rich phases in three distinct forms: massive or blocky (primary Al_2Cu phase containing $\sim$ 40 % Cu), eutectic type (fine dispersed eutectic Al-Al_2Cu particles interspersed within Al matrix containing $\sim$ 24 % Cu) and ultra-fine eutectic $Al_5Mg_8Cu_2Si_6$ phase. The fine or ultrafine eutectic tend to form in the presence of nucleation sites such as $FeSiAl_5$ or high solidification rates while a distinct Al_7Cu_2Fe forms in the presence of Fe. Fig. 2.7 (Li, Samuel, Samuel, Ravindran & Valtierra, 2003) depicts eutectic and blocky Al_2Cu in as-cast 319 alloys. Cu addition is also associated with increased microporosity in as-cast 356 alloys, a scenario attributed to reduced solidification temperature which extends the freezing time and eutectic mushy zone leading to liquid blockage during feeding (Xu-gang, Jie, Yao-Jun & Bin, 2012).

Cu addition, together with Mg addition, is primarily used to offer strength both in as cast and heat treated states through formation of various strengthening phases such as θ'(Al_2Cu) blocky phase and Q'($Al_5Mg_8Cu_2Si_6$) fine Chinese-script mor-

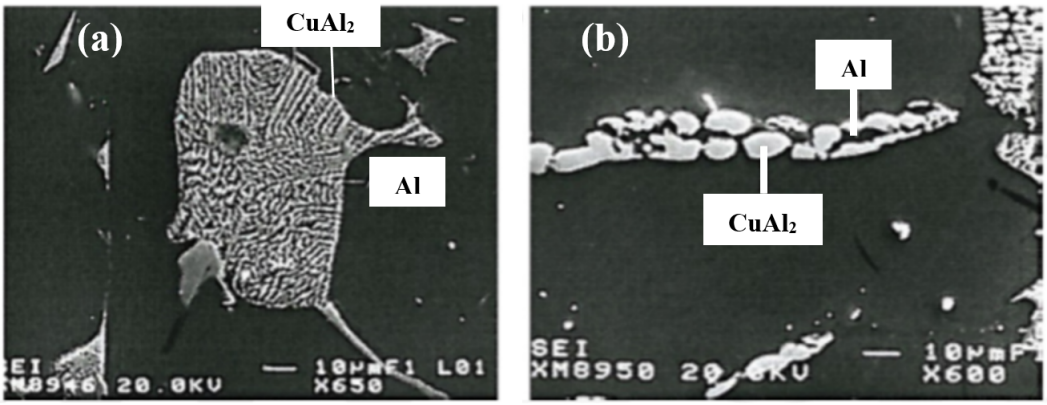

Figure 2.7: Cu-rich Al_2Cu phases in 319 alloys (a) eutectic (b) blocky (Li, Samuel, Samuel, Ravindran & Valtierra, 2003)

phology phase in the eutectic solidification region depicted in Fig. 2.8 (Caceres, Djurdjevic, Stockwell & Sokolowski, 1999).

Unfortunately, Cu-strengthened alloys are disadvantaged by their low strength at temperatures above 200 °C due to coarsening of strengthening phases. At times, this limits application of 356 alloys with Cu addition in high temperature applications. However, 356+Cu alloys have found extensive use in automotive cylinder heads and there is ongoing research to optimize Cu additions for high thermal strength applications (Javidani & Larouche, 2014).

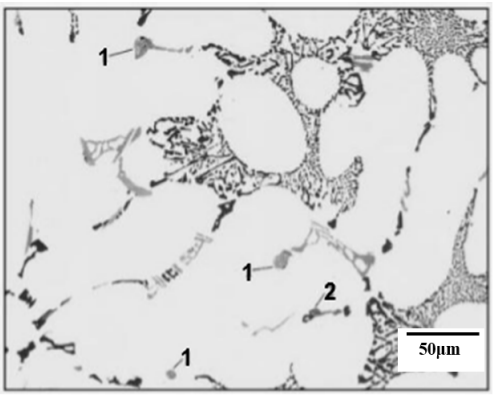

Figure 2.8: Microstructure of an Al-Si-Mg alloy containing 0.22 % Cu where: (1) Q-$Al_5Mg_8Cu_2Si_6$ and (2) θ-$CuAl_2$ (Caceres, Djurdjevic, Stockwell & Sokolowski, 1999)

Zirconium addition is primarily associated with grain refinement of Al-Si alloys. Fig. 2.9 shows micrographs of Zr grain refined A356 alloys at 0 % Zr in as-cast alloy (average grain size of 0.9 mm) and at 0.3 % Zr after 24h solution treatment (average grain size of 0.7 mm), Baradarani and Raiszadeh (2011). In their study (Baradarani & Raiszadeh, 2011), grain refinement was attributed to formation of $L1_2$-Al_3Zr particles which nucleate and grow as a primary phase

during solidification and also act as preferred sites for heterogeneous nucleation of α-Al particles. However, it tends to reduce the grain refining effect of Ti plus Boron additions such that it becomes necessary to use more Ti and B to grain refine Zr-containing alloys (Rambabu, 2017.

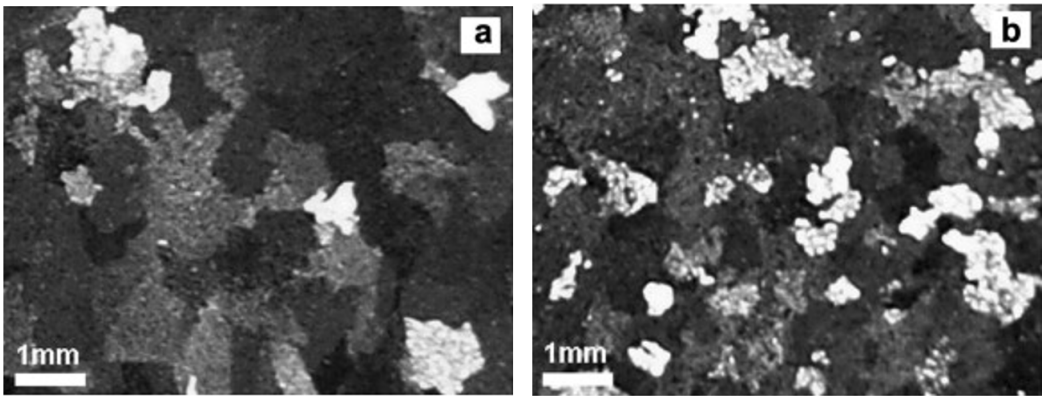

Figure 2.9: Micrographs of Zr grain refined A356 alloys showing addition of: (a) 0 % Zr and (b) 0.3 % Zr (Baradarani & Raiszadeh, 2011)

Zr addition leads to formation of Al_3Zr precipitates which are relatively inert and coarsening resistant in the matrix at temperatures in the order of 275 - 425 ^oC (Knipling, Dunand & Seidman, 2007; Devore & Farnum, 1999 thus ensuring high thermal stability. Low solubility of finely dispersed Zr-rich second phase particles which can resist overaging and growth preserves mechanical properties to a greater extent even at high temperatures (Donovan, Fortune & Trout, 2015). They also act as hard pinning points in the matrix which inhibits dislocation motion thus ensuring general improvement in strength relative to the shape of intermetallic particles, their volume fraction, and contiguity with eutectic Si.

Vanadium acts as a grain refiner through formation of phases such as Al_3V (Meng, Cui, Zhao & Zuo, 2013). Al_3V phase has a high thermal stability and thus minor additions of V improves high temperature strength of cast Al-Si alloys (Elhadari et al., 2011). In a study by Prasada (2011), vanadium addition to A319 alloy changed the morphology of Fe-rich phases from coarse platelets to near equiaxed by forming complex intermetallics with Fe. Additionally, V aided in the spheroidisation of eutectic Si and other Fe-rich phases during solutionizing.

Zr, V and Ti combined addition leads to the formation of thermally stable trialuminide precipitates that promote interaction between nano-sized particles and dislocations. For example, in a study by Shaha, Czerwinski, Kasprzak, Friedman & Chen (2015), combined addition of 0.56Zr, 0.32V, and 0.20Ti to Al-7Si-1Cu-0.5Mg alloy led to formation of micro-sized AlSiTiVZr and AlSiTiZrFe phases that maintained their stability even upon heat treatment. It also resulted in improved mechanical properties such as tensile and low cycle fatigue strength due to the presence of $(AlSi)_2(TiZr)Fe$ instead of β-Al_5FeSi phase. Similar findings have been noted and reported by other researchers (Elhadari et al., 2011; Shaha, Czerwinski, Kasprzak, Friedman & Chen, 2014).

2.3 Thermal analysis

2.3.1 Introduction

Thermal analysis (TA) involves studying material properties by heating or cooling it, recording the change in temperature with time and interpreting the variation and the shape of the resulting curves. It is based on the fact that any event that occurs during cooling affects the shape of the cooling curve and that of its derivatives. This is because of microstructure transformations and the accompanying heat releases in the course of solidification. When TA results are analyzed, a lot of information can be obtained including but not limited to: level of modification, alloy composition, SDAS, grain size and the temperature at which different phases precipitate (Djurdjevic, Sokolowski & Odanovic, 2012). However, TA results may vary from one experiment to another, even for identical alloys, for reasons such as: differing cooling rates (Djurdjevic & Manasijevic, 2014), melt and crucible temperatures before and after experimenting, and differing alloy compositions. Regardless, TA results can be used to give an improved understanding of various important properties of castings prior to processing. This can improve processing and quality of castings and can ensure effective material use. Further, these results can be fed into simulation software to improve on their accuracy and to predict the properties of non-existing alloys. Thus, TA has gained increasing acceptance and application in most aluminium foundries for its applicability, ease of use, affordability, and ability to provide consistent results (Djurdjevic et al., 2012; Djurdjevic, Manasijevic, Odanovic & Radisa, 2013).

2.3.2 Solidification process and sample characteristic temperatures of Al-Si alloys

In hypoeutectic Al-Si alloys, general solidification sequence begins with nucleation of primary α-aluminium dendrites from which secondary and tertiary dendrites grow. The grown dendrites then begin to impinge on each other leading to their coherency. After this, Fe-containing phases solidify both before and after Al-Si eutectic nucleation. Following this is usually the rigidity point which marks transition from interdendritic to burst feeding (Djurdjevic and Manasijevic, 2014). Thereafter, the Mg-related phases solidify followed by the Cu-rich phases and finally, solidification comes to an end when the last liquid solidifies. These nucleation temperatures can be obtained from the following curves:

(a) Temperature (T) versus time (t)

(b) ΔT (Change in temperature between the wall, T_w, and the centre thermocouple, T_c, i.e., (T_w – T_c) vs. t

(c) First derivative of temperature versus time ($\frac{dT}{dt}$) vs. t

(d) Second derivative of temperature versus time ($\frac{d^2T}{dt^2}$) vs. t

(e) A combination of the four plots above

(f) Superimposed $\triangle$T versus T or t and $\frac{dT}{dt}$ versus T or t curves

Basic identification of some metallurgically strong reactions can be done based on slope changes and turning points in the aforementioned curves (Farahany, Ourdjini & Idris, 2012).

The liquidus temperature is of paramount importance since it defines the preheating temperature by allowing the foundry engineer to decide on a suitable difference between the initial melt temperature, pouring, and liquidus temperature (Djurdjevic et al., 2013). The α-Al dendrite network formation occurs in three stages: α-Al dendrite nucleation temperature, ($T_N{}^{\alpha\text{-Al}}$), α-Al dendrite minimum temperature, ($T_{Min}{}^{\alpha\text{-Al}}$), and α-Al dendrite growth temperature, ($T_G{}^{\alpha\text{-Al}}$). The start of nucleation (alpha-nucleation or $T_N{}^{\alpha\text{-Al}}$) is usually accompanied by a change in slope of the cooling curve and a slight deviation from linearity of the $\frac{dT}{dt}$ vs. t curve (Cruz, Gonzalez, Juarez, Herrera & Juarez, 2006). Alpha - minimum ($T_{Min}{}^{\alpha\text{-Al}}$) is a local minimum on the cooling curve that is coincident with the first point at which the first derivative curve intersects the zero line ($\frac{dT}{dt}$

= 0). Lastly, Alpha - growth ($T_G{}^{\alpha\text{-Al}}$) is a local maximum on the cooling curve and it correspond to the second zero point that comes after the one signifying $T_{Min}{}^{\alpha\text{-Al}}$ on the first derivative. In cases where the $\frac{dT}{dt}$ curve does not intersect the zero line, $T_{Min}{}^{\alpha\text{-Al}}$ and $T_G{}^{\alpha\text{-Al}}$ would be considered identical and they would corresponds to the maximum point on the first derivative curve (Djurdjevic et al., 2012; Farahany, Ourdjini, Idrsi & Shabestari, 2013). Appendix 2 exemplifies these temperature readings (Farahany, Ourdjini, Idrsi & Shabestari, 2013). Free dendrite growth depends on Cu and Si amounts in the melt and it increases concentration of alloying elements such as Si, Cu, and Mg in the remaining melt.

During dendrite coherency, the tips of the once separate and freely growing dendrites come in contact forming a coherent dendritic network. The dendrite coherency point or temperature (DCP/DCT) can be determined using mechanical (or rheological methods) and using thermal detection methods. In TA, it is identified as the point where the difference in temperature between the near wall and center thermocouple is minimum. This point is projected from the minimum change in temperature between the near-wall, T_w, and the centre thermocouple, T_c, i.e., $\triangle T = T_w - T_c$ vs. t curve and read off on the centre thermocouple temperature (T_c) vs. time (t) curve. This technique is reported by several researchers to have been developed by Backerud (Backerud and Chalmers, 1969; Backerud, Chai & Tamminen, 1990). An example of how DCT was obtained in literature is shown in Appendix 3. It is reported by Barlow and Stefanescu (2002) that this minimum was used because forward dendrite growth proceeded from the wall towards the center and as the dendrites grew in the entire casting, the $\triangle T$ curve tended to go back to 0 °C. DCT indicates transition from mass feeding to interdendritic feeding and it is after its occurrence that casting defects such as macrosegregation and shrinkage porosity develop. Several factors affect the occurrence of this point. For example; Djurdjevic et al. (2013), reported that faster cooling rates postponed coherency to lower temperature while elements having a high solubility in Al tended to be less effective in reducing SDAS.

The beginning of Al-Si eutectic nucleation is marked as the point where there is a sudden increase in the $\frac{dT}{dt}$. Appendix 2 exemplifies this reading as obtained by Farahany et al. (2013). When nucleation of Al-Si eutectic occurs, the eutectic mixture of Si and α-Al leads to a further increase in concentration of Cu and other alloying elements that have remained in the residual liquid. Just prior to this but after DCT is usually the precipitation of Fe-containing phases such as Al_5FeSi and

$Al_{15}(FeMn)_3Si_2$. Al-Si eutectic solidification follows rigidity temperature which is followed by precipitation of Mg-related phases such as Mg_2Si and $Al_8Mg_3FeSi_6$. At times, detection of Fe-rich and the Mg-related phases is impossible on cooling curves due to weak signals and minor quantities in the alloy.

Cu-rich phases are usually detected as one or two distinct peaks towards the end of the $\frac{dT}{dt}$ vs. t curves (Djurdjevic et al., 2013; Djurdjevic, Odanovic, & Talijan (2011); Djurdjevic, Huber & Odanovic (2012). Those that nucleate during solidification are majorly the massive or blocky Al_2Cu, fine Al-Al_2Cu phase or the ultra-fine $Al_5Mg_8Cu_2Si_6$ phases as discussed in Section 2.2.4. It was reported by Djurdjevic et al. (2013) that $Al_5Mg_8Cu_2Si_6$ copper eutectic occured as branched crystals or fine eutectic strings growing out from Al_2Cu blocky or Al-Al_2Cu eutectic types during the final stage of solidification. They also reported that at times, blocky Al_2Cu may have formed together with β-Al_5FeSi platelets. The solidification temperatures of Cu-rich phases can help define the maximum possible temperature that the castings can be exposed to during solution heat treatment with an aim of minimizing the incipient melting of these phases (Djurdjevic, Manasijevic, Odanovic, Dolic & Radisa, 2014). Several researchers have pointed this out but it has not been pursued further. This information is of paramount importance because the same phases play a crucial role in precipitation during artificial aging and this inevitably affects mechanical performance. However, the noticeability of some Cu-phases on TA curves depends on the quantity of Cu in the alloy and the related latent heat released during solidification. Appendix 4 shows how Cu-rich phases were identified by Djurdjevic et al. (2014).

Solidification ends at the point which the liquid portion (all intermetallics) has totally solidified and beyond which an entirety of stable solid phase exists. The solidus temperature is identified at the region closest to the last distinct minimum on the $\frac{dT}{dt}$ curve and at a point where a tangent drawn on the $\frac{dT}{dt}$ curve just begun to stabilize (Barlow & Stefanescu, 2002; Tamminen, 1988). Appendix 5 shows how this temperature reading was obtained by Barlow & Stefanescu, 2002.

2.3.3 Effect of additives on Solidification behavior of Al-Si alloys

Chemical composition, brought about by varying alloying additions, exert a strong influence on solidification characteristics and resultant microstructures. Some sole and combined impacts of various elemental additions on the solidification behavior of Al-Si alloys are discussed below.

Strontium addition increases the quantity of blocky Al_2Cu and ultra-fine $Al_5Mg_8Cu_2Si_6$ phases compared to the fine Al-Al_2Cu phase (Pelayo, Sokolowski & Lashkari, 2009) and this increases with increase in Sr content. Increased blocky Cu-phase shifts the ratio of the various amounts of Cu-rich phases present consequently leading to an increase in nucleation temperature of Cu-rich phases (Djurdjevic, Byczynski, Schechowiak, Stieler, & Pavlovic, 2009).

Sr addition is also associated with a reduction in eutectic Al-Si nucleation temperature and a lengthened eutectic plateau. This has been confirmed by several researchers such as: a decrease of 8.7K when Sr was added to alloy Al–7Si–0.3Mg–0.8Fe (Kumari, Pillai, Rajan & Pai, 2007) and a decrease of 9.8 °C (from 562.4 °C to 552.6 °C) when Sr addition was increased from 1 to 210 ppm in alloy AlSi6Cu4 with a maximum increase noted at about 173 ppm (Djurdjevic et al., 2009). Also, Sr addition increased the end of solidification temperature.

Copper addition has been shown to lower liquidus, dendrite coherency, Al-Si and Al-Si-Cu nucleation temperatures when both cooling curve analysis and commercial software such as Pandat (Scheil mode), JMatPro, and FactSage are used (Djurdjevic, 2013; Backerud, 1990, Djurdjevic, 2014). Fig. 2.10 (a) shows the effect of adding 1 to 4 % Cu to alloy Al-5Si, solidified at a cooling rate of $6Kmin^{-1}$ on the liquidus, coherency, nucleation temperatures of Al-Si and Al-Si-Cu phases and the solidus temperatures (Djurdjevic, 2014). The depressions tend to be lower when commercial software are used since some of them are incapable of detecting the impact of small amounts of residual Sr (Djurdjevic, 2013). Much lower temperatures are obtained for alloys with lower Si than for those with higher ones (Djurdjevic, 2012). Decrease in temperature may also be due to other factors such as high concentration of alloying elements (increased by Cu addition) which deters dendrite growth, thus postponing coherency (Djurdjevic, 2012).

Copper addition alters the shape of Cu-enriched phases' peaks in the cooling and derivative curves and this is associated with change in related temperatures. More specifically, there is an increase in solidification temperature interval and nucleation time of the Cu-rich phases with increase in the amount of Cu (Djurdjevic, 2014). Fig. 2.10 (b) exemplifies increase in solidification time of Cu-rich phases (as depicted by their peaks) interval from 1167 s to 1211 s and of total solidification from 31.4 °C to 65.4 °C for alloys Al-5Si-1Cu and Al-5Si-4Cu respectively. Consequently, other properties such as increase in microporosity.

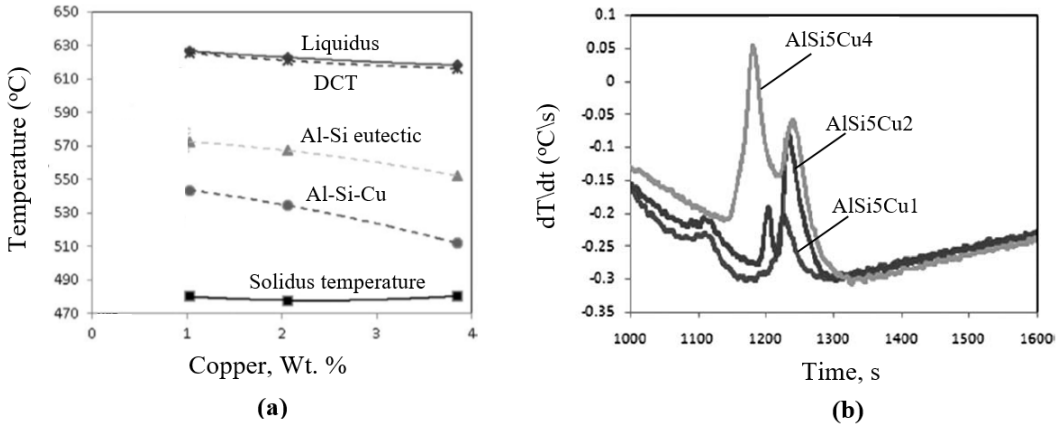

Figure 2.10: Alloy Al-5Si-(1-4)Cu: (a) Impact of 1-4 %Cu on solidification temperatures; (b) Part of $\frac{dT}{dt}$ curve showing precipitation of Cu-rich phases (Djurdjevic, 2014)

The effect of Mg on the solidification behavior of Al-Si related alloys has not been widely studied. However, Mg addition above 0.5 % in Al-Si-Cu alloys has been associated with precipitation of ultra-fine $Al_5Mg_8Cu_2Si_6$ copper eutectic (Doty, Samuel, Samuel, 1996). Increased Mg has been associated with decrease in Al-Si and Al-Si-Cu eutectic nucleation temperatures (Gowri & Samuel, 1994). Javidani and Larouche (2014) reported that presence of Mg, even in small amounts of about 0.06 %, led to transformation of Al_5FeSi phase to π-$Al_8FeMg_3Si_6$ phase. It also resulted in precipitation of Q-$Al_5Cu_2Mg_8Si_6$, which grew out of blocky or eutectic θ-Al_2Cu particles, and Mg_2Si phases during solidification.

Iron addition led to increase in liquidus and eutectic temperatures with this being more evident at a faster cooling rate (Gowri & Samuel, 1994). It was also reported that addition of low Fe quantities in A356 alloys caused lack of precipitation of some pre and post-eutectic Fe-phases such as $Al_8FeMg_3Si_6$ (Javidani & Larouche, 2014). However, Fe was strongly partitioned in liquid phase which may have resulted in Fe-phases' precipitation.

Addition of Na modifier was reported by Djurdjevic et al. (2013) to have depressed Al-Si temperature significantly in Al-Si-Cu alloys.

(c) Effect of Pb, Sn, Bi, and Cd on solidification

These low melting point elements in Al-Si-Cu alloys significantly extends their solidification range thus lowering their corresponding solidus temperatures (Djurdjevic et al., 2013). Extended solidification path makes the related alloys prone to shrinkage porosity. Fig. 2.11 illustrates how increased Sn addition from 0 - 500 ppm and Pb content from 0 - 1000 ppm decreased solidus temperatures from 500

to 491 °C and from 497 to 481 °C respectively in Al-Si-Cu alloys (Djurdjevic et al., 2012). However, high Sn and Pb addition to AlSiCu insignificantly impacted liquidus, Al-Si, and Al-Si-Cu temperatures (Djurdjevic, 2012).

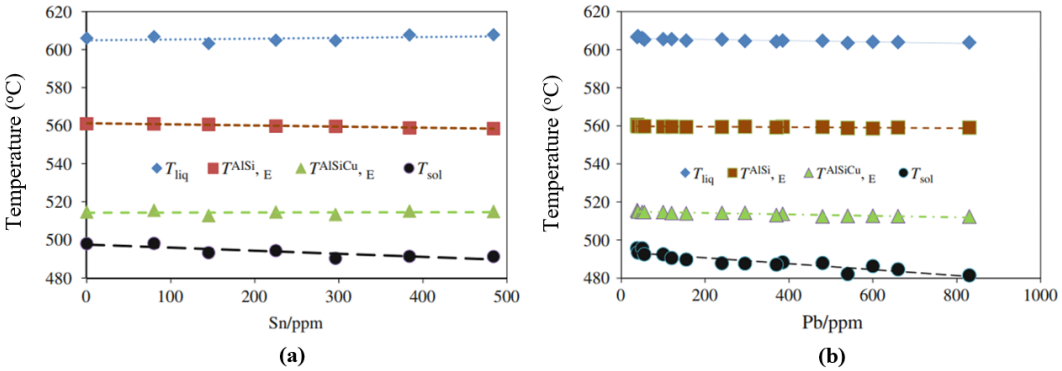

Figure 2.11: Impact of (a) Sn and (b) Pb on characteristics solidification temperature of AlSiCu alloys (Djurdjevic, 2012)

2.3.4 Typical Solidification Temperatures for Common Al-Si Cast Alloy solidification phases

Table 2.1 shows specific chemical composition in wt.% of alloys whose phase formation temperatures are shown in Table 2.2. The same serial numbers (see the first columns) are used to represent the same alloy in Tables 2.1 and 2.2.

- The last column of both Table 2.1and 2.2 represent the following references: A – Djurdjevic Manasijevic, 2014; B – Djurdjevic et al., 2013; C – Sreeja et al., 2007; D - Djurdjevic et al., 2009; E - Djurdjevic et al., 2012; F - Djurdjevic et al., 2011; G – Samuel, Ouellet, Samuel Doty, 1998; H - Dobrzanski, 2006).
- P S represents Pandat Program in Scheil Mode; CCA represents cooling curve analysis; AR is used to mean “as recorded” by the reference given alongside it.
- Note: the numbers titles “1” to “10” in Table 2.2 represent various temperatures as follows: 1- -Al dendritic network, 2 - DCT, 3 - Pre-eutectic Fe intermetallics, 4 - Eutectic Si (Al-Si), 5 - Rigidity, 6 – Post-eutectic Fe-phases i.e -Al5FeSi/transformation of -Al5FeSi to Al8Mg3FeSi6, 7 - Mg2Si, 8 - Cu-rich phases (Al-Si-Cu). Note that: * represents blocky/ massive Al2Cu (40 wt. %Cu) while ** represents fine Al2Cu eutectic (24 wt. % Cu), 9 - ultra-fine Al5Mg8Cu2Si6, 10 – Solidus, 11 – References.

Table 2.1: Chemical composition in wt.% of sample Al-Si alloys subjected to TA tests

S. No.	Si	Fe	Cu	Mg	Mn	Ti	Cr	Sr	Others	References
1	5.91	0.07	1.07	0.14	0.01	-	-	-	0.01 Zn	[A]
2	5.90	0.11	1.83	0.15	0.01	-	-	-	0.01 Zn	[A]
3	5.82	0.06	3.03	0.15	0.01	-	-	-	0.01 Zn	[A]
4	5.78	0.07	3.96	0.13	0.01	-	-	-	0.01 Zn	[A]
5	8.03	0.136	1.09	0.0006	0.0029	-	-	-	0.003 Zn	[A]
6	8.14	0.123	1.93	0.0007	0.0028	-	-	-	0.0025 Zn	[A]
7	8.03	0.141	2.96	0.0009	0.0032	-	-	-	0.0031 Zn	[A]
8	7.84	0.138	4.31	0.0008	0.0031	-	-	-	0.003 Zn	[A]
9	Al-Si-Cu									[B] - AR
10	7.13	0.12	0.96	0.28	0.01	0.056	-	0.0041	0.007 Ni 0.01 Zn	[B] - CCA
11	7.13	0.12	0.96	0.28	0.01	0.056	-	0.0041	0.007 Ni 0.01 Zn	[B] - P& S
12	7.05	0.13	1.98	0.28	0.01	0.079	-	0.0037	0.009 Ni 0.01 Zn	[B] - CCA
13	7.05	0.13	1.98	0.28	0.01	0.079	-	0.0037	0.009 Ni 0.01 Zn	[B] - P& S
14	6.95	0.14	3.05	0.26	0.01	0.081	-	0.0031	0.007 Ni 0.01 Zn	[B] - CCA
15	6.95	0.14	3.05	0.26	0.01	0.081	-	0.0031	0.007 Ni 0.01 Zn	[B] - P&S
16	6.75	0.12	4.38	0.29	0.01	0.091	-	0.0042	0.008 Ni 0.01 Zn	[B] - CCA
17	6.75	0.12	4.38	0.29	0.01	0.091	-	0.0042	0.008 Ni 0.01 Zn	[B] - P&S
18	7	0.8	-	0.3	-	-	-	-	-	[C]
19	7	0.8	-	0.3	-	-	-	-	0.2 Be	[C]
20	7	0.8	-	0.3	0.4	-	-	-	-	[C]
21	7	0.8	-	0.3	-	-	-	-	0.04 Ca	[C]
22	7	0.8	-	0.3	-	-	-	0.04	-	[C]
23	AlSi6Cu4									[D] - AR
24	AlSi8Cu (1–4)									[E]
25	5.0	0.09-0.1	1-4	0.14-0.26	0.01				0.007-0.09Ni 0.01 Zn	[F]
26	6.23	0.441	3.8	0.075	0.108	0.07	0.007	-	-	[G]
27	6.23	0.377	3.8	0.6	0.097	0.07	0.007	-	-	[G]
28	6.23	0.410	3.8	0.1	0.1	0.07	0.007	0.040	-	[G]
29	6.23	0.370	3.8	0.55	0.095	0.07	0.007	0.030	-	[G]
30	AlSiXCuX (3XX) alloys									[H]

2.4 Heat treatment of 356-type cast aluminium alloys

2.4.1 Heat treatment tempers

Various heat treatment tempers when applied impart different properties in different classes of Al-Si alloys. Basic temper designations are presented immediately following the alloy designation with a hyphen between the designation and the temper (e.g., 356-T6). The general class of treatment is indicated by the first character (a capital letter) in the temper designation. Examples of the general

Table 2.2: Chemical composition in wt.% of sample Al-Si alloys subjected to TA tests

S. No.	Si	Fe	Cu	Mg	Mn	Ti	Cr	Sr	Others	References
1	5.91	0.07	1.07	0.14	0.01	-	-	-	0.01 Zn	[A]
2	5.90	0.11	1.83	0.15	0.01	-	-	-	0.01 Zn	[A]
3	5.82	0.06	3.03	0.15	0.01	-	-	-	0.01 Zn	[A]
4	5.78	0.07	3.96	0.13	0.01	-	-	-	0.01 Zn	[A]
5	8.03	0.136	1.09	0.0006	0.0029	-	-	-	0.003 Zn	[A]
6	8.14	0.123	1.93	0.0007	0.0028	-	-	-	0.0025 Zn	[A]
7	8.03	0.141	2.96	0.0009	0.0032	-	-	-	0.0031 Zn	[A]
8	7.84	0.138	4.31	0.0008	0.0031	-	-	-	0.003 Zn	[A]
9	Al-Si-Cu									[B] - AR
10	7.13	0.12	0.96	0.28	0.01	0.056	-	0.0041	0.007 Ni 0.01 Zn	[B] - CCA
11	7.13	0.12	0.96	0.28	0.01	0.056	-	0.0041	0.007 Ni 0.01 Zn	[B] - P& S
12	7.05	0.13	1.98	0.28	0.01	0.079	-	0.0037	0.009 Ni 0.01 Zn	[B] - CCA
13	7.05	0.13	1.98	0.28	0.01	0.079	-	0.0037	0.009 Ni 0.01 Zn	[B] - P& S
14	6.95	0.14	3.05	0.26	0.01	0.081	-	0.0031	0.007 Ni 0.01 Zn	[B] - CCA
15	6.95	0.14	3.05	0.26	0.01	0.081	-	0.0031	0.007 Ni 0.01 Zn	[B] - P&S
16	6.75	0.12	4.38	0.29	0.01	0.091	-	0.0042	0.008 Ni 0.01 Zn	[B] - CCA
17	6.75	0.12	4.38	0.29	0.01	0.091	-	0.0042	0.008 Ni 0.01 Zn	[B] - P&S
18	7	0.8	-	0.3	-	-	-	-	-	[C]
19	7	0.8	-	0.3	-	-	-	-	0.2 Be	[C]
20	7	0.8	-	0.3	0.4	-	-	-	-	[C]
21	7	0.8	-	0.3	-	-	-	-	0.04 Ca	[C]
22	7	0.8	-	0.3	-	-	-	0.04	-	[C]
23	AlSi6Cu4									[D] - AR
24	AlSi8Cu (1–4)									[E]
25	5.0	0.09-0.1	1-4	0.14-0.26	0.01				0.007-0.09Ni 0.01 Zn	[F]
26	6.23	0.441	3.8	0.075	0.108	0.07	0.007	-	-	[G]
27	6.23	0.377	3.8	0.6	0.097	0.07	0.007	-	-	[G]
28	6.23	0.410	3.8	0.1	0.1	0.07	0.007	0.040	-	[G]
29	6.23	0.370	3.8	0.55	0.095	0.07	0.007	0.030	-	[G]
30	AlSiXCuX (3XX) alloys									[H]

heat treatment classes include: “F” for as fabricated, “O” for as annealed, “W” for as solution heat treated, and “T” for as thermally treated to produce stable tempers other than “F” or “O” (Davis, 1993). For Al-Si alloys, the T temper is the most commonly applied and especially the T6 temper because it results in peak strength. Table 2.3 shows some common standardized heat treatment tempers.

Table 2.3: Common applied standardized heat treatment T-temper designations

Code	Description
T4	Solution heat treated, quenched, and naturally aged to a substantially stable condition
T5	Cooled from an elevated temperature and artificially aged immediately after casting
T6	Solution heat treated, quenched, and artificially aged
T7	Solution heat treated, quenched, and overaged

2.4.2 T6 heat treatment of 356 cast aluminium alloys

(i) Introduction

Most cast Al-Si alloys of the 3xx series with Al-Si-Cu/Mg are heat treatable due to precipitation strengthening mechanisms (Mohamed & Samuel, 2012). T6 heat treatment of age-hardenable cast aluminium alloys involves solutionizing the alloys, quenching, and aging. Solution heat treatment is conducted at a temperature just below the eutectic temperature for a sufficiently long time for various roles such as dissolution of intermetallic phases (Sjolander, 2011).

Quenching involves cooling down the alloy from solution heat treatment temperature. Finally, aging allows for precipitate formation from the supersaturated solid solution, at room temperature (natural aging) and or at elevated temperature (artificial aging); Mohamed & Samuel, 2012.

(ii) Solution heat treatment

(a) Roles of solution heat treatment on microstructure and mechanical behavior

Solution heat treatment results in various microstructural changes which definitely affect mechanical performance. These are discussed below in detail:

First, dissolution of Cu- and Mg- rich particles formed during solidification occurs forming a solid solution. This avails more Cu for strengthening later during aging. Distribution of microconstituents also proceeds as dissolution does. Dissolution time is largely dependent on the size and nature of the primary solute particles within the alloy. It was reported by Mohamed and Samuel (2012) that, phases like Q-$Al_5Cu_2Mg_8Si_6$ were said to be insoluble while π-$Al_8Mg_3FeSi_6$ phases were difficult to dissolve during solutionizing. It was also reported by Apelian, Shivkumar & Sigworth (1990) that Fe-containing phases, such as α-$Al_{15}(Fe,Mn)_3Si_2$ and blocky Al_2Cu phase, unlike the fine eutectic Al-Al_2Cu phase that could dissolve within 2h of solid solution heat treatment, also had dissolution difficulties. This

Cu-phase dissolution difficulty was associated with the elongated uniform profile of the particles and its lower interfacial area with the matrix. Additionally, unlike fine Al-Al_2Cu particles that could disintegrate into smaller fragments that could spheroidise, blocky Al_2Cu dissolved through spheroidisation and diffusion. They also noted that dissolution tended to decrease noticeably as temperature decreased as exemplified by β-Al_5FeSi platelets that underwent fragmentation and slow dissolution, but only when subjected to higher temperatures for long.

Second, homogenization of microstructural alloying elements occurs upon dissolution. This is important since segregation of solute elements, resulting from dendritic solidification of alloying additions, may adversely effect mechanical properties. Homogenization time is determined by the diffusion rate and distance, which is directly affected by solutionizing temperature and dendrite arm spacing (DAS). Thus, homogenization improves fracture toughness and ductility.

Third, it changes the size and morphology of eutectic Si particles from a non-modified coarse, large, and plate-like shape to a modified fine fibrous coral-like shape. It was reported by Mohamed & Samuel (2012) in their review, that this occurs in two stages: first, fragmentation or dissolution of eutectic Si branches whereby Si particles undergo necking resulting in separate segments that tend to retain their original morphology. This thermal degradation may begin at crystal defects then govern the break-up process. Second, spheroidisation of fragmented Si particles which may occur concurrently with coarsening, especially on prolonged solutionizing. Several researchers have confirmed that chemical modifiers reduce spheroidisation time (Apelian et al., 1990; Shivkumar, Jr., & Apelian, 1990; Paray & Gruzleski, 1993). This is attributed to the vulnerability of fibrous eutectic Si particles to modification compared to plate-like structures. However, both modified and unmodified alloys experience faster spheroidisation at high cooling rates. Unlike big brittle fragments in unmodified alloys that are responsible for crack formation, fine fibrous Si particles improve ductility.

Fourth, transformation of Fe-rich phases such as Al_5FeSi and $Al_{15}(FeMn)_3Si_2$ is also a consequence of solution heat treatment especially when long holding times are employed (Long et al., 2013). More specifically, Al_5FeSi phase is dissolved into very small and difficult to observe needles while $Al_{15}(FeMn)_3Si_2$ phase is fragmented to smaller skeleton particles (unlike the compact skeleton-like form when untreated).

(b) Solution heat treatment parameters and their effect on microstructure-mechanical properties

To a great extent, solutionizing temperature and time depends on the as-cast microstructure; size, distribution, and type of intermetallics; extent of modification and desired level of spheroidisation and coarsening of eutectic Si (Sjolander, 2011; Ma, Maniruzzaman, MacKenzie & Sisson, 2007).

A high solutionizing temperature results in higher and faster dissolution, homogenization, and spheroidization and hence reduces solutionizing time (Javidani & Larouche, 2014; Sjolander, 2011). This translates to a high yield strength (YS) upon artificial aging (Sjolander, 2011). However, temperature increase is hindered by incipient melting of some phases, such as Cu-containing phases. This is associated with distortion and substantial reduction in mechanical properties but Sundman, Jansson & Andersson (1985), reported that a two-step solution heat treatment with carefully chosen holding times for both stages could be used to ensure increased strength and ductility. It was thus reported by Kasprzak et al. (2001), that conventional solutionizing temperature should be kept below the melting point of the Cu enriched phases but was to be high enough to facilitate dissolution of this phase and spheroidisation. Regardless, it was reported by Ma et al. (2007) that no significant change in ultimate tensile strength (UTS), hardness, and ductility was noted with a slight change in solutionizing temperature for Sr-modified alloys.

Solutionizing time should facilitate dissolution, homogenization, and modification of Si particles. However, too long a time causes overaging of microconstituents and negative impact on fracture elongation. For instance, time should be chosen carefully for alloys containing Al_2Cu phase which cannot undergo complete dissolution to avoid misuse of energy. Long solutionizing also leads to reduced hardening in as cast A356 alloys due to the enrichment of Mg on internal surfaces of pre-existing porosity since it reduces the volume fraction of Mg-Si containing strengthening precipitates (Long et al., 2013). Ma et al. (2007), reported that reducing solutionizing time from several hours to a few hours did not significantly affect mechanical properties of cast A356 alloys such as tensile strength. However, short solutionizing times of about 2 hours were generally associated with high hardness while high ductility had been obtained after longer solutionizing times of 8 hours (Yoshida & Arrowood, 1995).

Time needed for dissolution and homogenization strongly depends on coarseness of microstructure with coarser microstructures requiring more time than finer ones (Cupido, 2014). Time needed for spheroidization also majorly depends on solution heat treatment temperature and morphology and size of eutectic Si.

(iii) Quenching

(a) Roles of quenching on microstructure and mechanical behavior

Quenching prevents diffusion of elements and causes trapping of many thermal vacancies inside a material or within the atomic lattice structure (Sjolander, 2011; Zhang & Zheng 1996). It also leads to the concentration of solute atoms becoming greater than the equilibrium level consequently forming a supersaturated solid solution. While solute atoms should be maximally retained while suppressing precipitation, the supersaturated solid solution should hold at temperatures other than quenching temperatures. It was reported by Ma et al. (2007), that suppressed precipitation during quenching and retention of solute atoms and quenched-in vacancies in solution aided in controlling distortion and minimizing residual stresses.

(b) Quenching parameters and their effect on microstructure-mechanical properties

During quenching, there is a great temperature gradient that is experienced as a sample is moved from much higher temperatures to comparatively low temperatures. Most microstructure-mechanical properties of age hardenable Al-Si-Mg alloys thus depend on the cooling rate after solutionizing (Ma et al., 2007).

Transfer time period of the specimen from the furnace to the quench media should be short so as to pass quickly through the critical temperature range where very rapid precipitation can occur.

The quench rate should be chosen to ensure that desired microstructure can be obtained within the shortest time possible. It was reported by several researchers (Mohamed & Samuel, 2012; Ma et al., 2007; Cupido, 2014), that a sufficiently high quench rate was essential for high strength and ductility because it ensured a high concentration of vacancies and solutes in solid solution were retained (Ma et al, 2007), and it minimized premature precipitation (Javidani & Larouche, 2014). It also enabled high mobility of elements in the primary Al during aging (Cupido, 2014). However, this was associated with high residual internal thermal stresses and distortion, especially for cast components with thin sections and complex

shapes (Ma et al, 2007). On the other hand, a slow quenching rate results in less residual stresses consequently improving fatigue properties and minimizing distortion. However, it causes detrimental effects such as heterogeneous precipitation of particles during quenching at grain boundaries or dislocations, which lowers solute supersaturation. It was reported by Cupido (2014), that this led to localized overaging, reduction in grain boundaries, increased tendency for corrosion, and reduced aging treatment response such as lower maximum YS.

Quench media temperature affects end mechanical properties of cast Al-Si alloys with significant effect being on UTS and YS than on ductility. Zhang and Zheng (1996) reported that an increase in quenching temperature was associated with a decrease in density and a slight increase in size of β"-Mg_2Si precipitates and a rise in fine Si precipitates. On the other hand, slow quenching in air resulted in an increase in the Si and Mg diffusion consequently leading to a higher density of fine β"-Mg_2Si precipitates and an increase in coarse rod-like β'-Mg_2Si (Mohamed & Samuel, 2012). This reduced the supersaturation of Mg and Si in the matrix. Regardless, quenching conditions hardly affects size and shape of eutectic Si (Ma et al, 2007).

(iv) Aging

(a) Roles of aging on microstructure and mechanical behavior

It allows for precipitate formation (Javidani & Larouche, 2014; Sjolander, 2011) from the high supersaturation of solute atoms and vacancies obtained from solution heat treatment and quenching (Mohamed & Samuel, 2012). The strengthening precipitates retained upon quenching are then uniformly distributed for homogeneous and improved material properties (Cupido, 2014). Aging is also associated with relieving residual stresses.

(b) Aging parameters and their effect on microstructure-mechanical properties

High temperature leads to enhanced diffusion and accelerated aging since it increases nucleation and growth rates. Aging time to peak hardness is increased when low temperatures are involved. For example, it was reported by Javidani & Larouche (2004), that as much as aging time to attain peak hardness was generally longer for AlSiCu than AlSiCu(Mg) alloys, it was even longer when low temperatures (about 160 ^{o}C) were employed.

The first few minutes of aging are usually associated with a slight increase in elongation but as time increases, ductility decreases. This has been attributed to precipitation of Mg_2Si which hinders the dislocation motion during tensile loading (Ragab, Samuel, Al-Ahmari, Samuel & Doty, 2011). In a study by Lados, Apelian & Wang (2011), the effects of artificial aging time on mechanical properties of Al-Si-Mg cast alloys were studied on varying Si content (1 - 13 wt.%) in the unmodified and Sr-modified states. Within the first 2 hours, there was a low increase in UTS and YS which significantly increased after 2 hours to ∼10 hours beyond which UTS and YS remained almost constant. Increase in YS was greater than UTS over the same aging time. For elongation, decrease was noted from 2 hours to ∼14 hours beyond which no significant change was observed. At temperature greater than 180 °C, there was a rapid decrease in strength and no significant improvement in ductility was noted with prolonged aging. However, the alloys were majorly strengthened by GP zones and β phase.

2.5 Tensile Properties of 356-Type Alloys

2.5.1 Factors affecting tensile properties

When casting defects are minimal or barely present, tensile properties of A356 alloys are primarily dominated by microstructural characteristics strongly controlled by the solidification rate, chemical modification, and post solidification treatment or a combination of all these. These affect strain hardening behavior, development of internal stresses in the particles, and the rate of damage accumulation in the alloys (Wang, 2003). Other factors include: loading parameters, particle clustering, and alloying elements addition.

(i) Alloy composition

Si forms the major alloying element in Al-Si-Mg alloys but Si particles possess plate-like morphology which initiates cracks thus negatively impacting ductility. Morphology change towards a more fibrous form can be by: rapid solidification, heat treatment, using chemical modifiers or combining these processes.

(a) Solidification rate

Solidification rate is primarily affected by the casting process i.e., the melt treatment and pouring procedure. This in turn affects several aspects of the microstructure and hence the tensile behavior. Microstructural aspects include:

The texture of the microstructure affects tensile behavior of Al-Si alloys. Slow solidification is associated with large, coarse, and brittle intermetallics and this may initiate or link fracture paths leading to rapid particle cracking and this consequently decreases elongation to fracture and strength (Zamani, 2015). This however has an insignificant effect on YS and UTS (Sjolander, 2011; Rambabu et al., 2017; Wang, 2003). On the other hand, rapid solidification results in a refined microstructures whose progression of particle cracking is more gradual and generally lower (Wang, 2003). The resultant smaller and more rounded particles lead to improved tensile strength and ductility up to temperatures of about 280 °C (Zamani, 2015).

The fracture mode present in the alloy affects tensile properties. For example, in alloys showing intergranular fracture, increasing cooling rate improves ductility in unmodified and Sr-modified conditions while in transgranular fracture, increasing cooling rate is not necessarily beneficial for ductility (Wang, 2003).

Defect characteristics such as pore size, shape, distribution, and fraction are affected by the grain size which is a factor of the cooling rate (Sjolander, 2011). For instance, increasing cooling rate lowers defect sizes and vice versa. Similarly, particle size and aspect ratio will also decrease when the cooling rate is increased thus leading to a pronounced increase in ductility. However, when particle shape and size remain fairly constant, ductility decreases even with increase in cooling rate (Qasim, Jabbar & Hassan, 2017).

Distribution of secondary phases and size of SDAS have an impact on tensile properties. Smaller SDAS lead to finer and more even distribution of second phase constituents and this leads to a substantial improvement in tensile strength and elongation (Zamani, 2015). Usually, large iron needles (usually unaffected by Sr addition) dominate fracture and so do large Si particles with flake-like morphology (Zamani, 2015). In addition, small SDAS usually have microcracks whose linkage occurs by ductile fracture of eutectic matrix between microcracks while large SDAS usually have larger microcracks in the cell boundaries that tend to link with adjacent cracks by the shear tearing of aluminium dendrites.

(b) Sr modification

Sr modifies eutectic Si from coarse plate-like into fine fibrous texture and this changes the fracture mode from transgranular and brittle to intergranular and interdendritic. This affects both strength and ductility positively but elongation

is improved to a greater extent than tensile strength (Zamani, 2015). However, Sr addition may not improve alloy ductility when size and morphology of Fe-bearing phases are not controlled (Wang, 2003). Also, Sjolander (2011), reported that presence of some alloying elements such as Mg could negate Sr modification.

(c) Post solidification treatment

This is mostly aimed at inhibiting dislocation motion. Deformation begins when applied stress is great enough to activate dislocation sources and stops only when back stress from dislocations, piled up at obstructions, exceeds the applied stress. Dislocation motion can be inhibited using fine dispersion of precipitates, especially for alloys that do not respond to heat treatment, and through precipitation hardening for heat treatable ones (this obstructs dislocation movements) (Rambabu et al., 2017). Hindered dislocation motion increases tensile strength but decreases elongation. However, Si spheroidisation increases ductility.

(d) Alloying solutes

Tensile strength tends to decrease at temperatures above 300-500 °C due to solute concentration e.g., Cu and Mg in the dendrites. At temperatures below 300 °C, Al-Si alloys tend to be brittle due to accumulation of high volume fraction of damaged particles such as Cu-Fe phases and Si particles (Zamani, 2015).

(ii) Test temperature

Tensile performance heavily depends on test temperature and exposure time. It is well known that increase in temperature increases ductility and toughness but lowers yield stress and modulus of elasticity and vice versa. One major reason is easy dislocation movement which causes a decrease in strength.

(iii) Particle clustering

According to Wang (2003), clustered particles lead to high particle cracking and an early occurrence of microcracks linkage during damage process thus lowering ductility. Decreasing SDAS, refining eutectic particles and applying solution heat treatment helps reduce the number of clustered particles.

(iv) Minor additions of alloying elements

(a) Effect of addition of Fe, Mn, and Cr

Increase in Fe content decreases ductility significantly with a further increase reducing tensile strength (but less severely than ductility) (Sigworth, 2011). This

has been associated with formation of brittle β-Al_5FeSi phase which possesses a harmful plate-like morphology (Zamani, 2015). However, the α-$Al_{15}(Fe,Mn)_3Si_2$ phase has a compact Chinese script morphology making it less susceptible to causing failure. Generally, Fe-bearing compounds are easily fractured under tension than the Al-matrix or modified Si (Javidani & Larouche, 2014).

Combined addition of Mn and Cr can be used effectively to modify the β-Fe phase in 356 alloys. This improves tensile properties (UTS and El %) due to precipitation of α-Al(Mn,Cr,Fe)Si nanoparticles in the microstructure (Javidani & Larouche, 2014).

(b) Effect of addition of Zr, V, and Ti

Addition of Zr does not necessarily lead to an increase in tensile properties. It was reported by Jovid et al. (2016), that addition of 0.11 % Zr to Al-Si piston alloys led to a moderate increase in tensile properties at 350 °C while 0.46 % Zr addition decreased these properties. The improvement was attributed to strengthening effect of Zr while deterioration to the formation of ZrAlSi intermetallics which possessed a harmful morphology. Additionally, in a study by Javidani & Larouche (2014), 0.15 % Zr addition to AlSiMg alloy (Al–7Si–0.4Mg–0.15Fe–0.15Ti + 0.15 % Cu) had an insignificant influence on tensile properties. Similar results were obtained by Mohamed, Samuel & Kahtani (2013) for alloy 354 subjected to tensile tests at 25, 190, 250, 300 °C in T6 heat treated state.

It was reported by Jovid et al. (2016) that introduction of V and Zr to A356 alloy led to improved yield point but UTS was not significantly changed. Shaha et al., (2015) associated combined addition of V, Zr, and Ti with increased alloy strength at the expense of ductility in Al-Si-Cu-Mg alloys.

(c) Effect of addition of Sr, Cu, and Mg

Sr addition, just like solution heat treatment, does not affect SDAS but it significantly reduces size and aspect ratio of Si particles by as much as 50-100 % through modification and spheroidisation effects. This significantly increases ductility (Wang, 2003) but slightly lowers YS. Sr modification also tend to increase ductility in A356 alloys more than in A357 alloys. It was also reported by Ragab et al. (2011), that some authors claimed that Sr addition increased tensile strength through increased nucleation rate of Mg_2Si.

0.5 % Cu addition to AlSiMg alloy (Al–7Si–0.4Mg–0.15Fe–0.15Ti) improved YS

and UTS both at ambient and high temperatures with insignificant change in elongation (Javidani & Larouche, 2014). Cu addition led to presence of Cu-bearing phases associated with high temperature strength (to 200 °).

Mg addition, even in small amounts of 0.1 to 0.2wt.%, to AlSiCu alloys improves room temperature tensile strength. However, low Mg alloys may be characterized by low tensile strength due low density of Mg_2Si hardening precipitates formed and which are related to the amount of vacancies present (Ma et al., 2007).

According to the literature review by Sjolander (2011), combined addition of Cu and Mg leads to increased alloy strength, especially when Cu and Mg exist as small precipitates upon heat treatment, but at the expense of ductility. However, resultant strength and ductility are affected by factors such as whether the Cu and Mg exist as coarse phases upon solidification or as atoms in solid solution or as GP zones formed at room temperature or as precipitates formed upon artificial aging. Sjolander (2011) exemplifies this by coarse solidification phases such as Al_2Cu and Q-$Al_5Mg_8Si_6Cu_2$ in Al-Si-Cu-Mg alloys, and π-$Al_8Mg_3FeSi_6$ and Mg_2Si formed in Al-Si-Mg alloys that do not contribute to strength. Their degree of influence on ductility is said to depend on their distribution and size relative to the Si particles. In addition, Cu and Mg lead to formation of bands of coarse Si particles and increased risk for shrinkage porosity due to increased solidification interval, which may adversely affect elongation to fracture.

2.5.2 Fracture during tensile loading and failure

Tensile loading may results in two modes of failure which may be brittle or ductile in nature. Brittle fracture is dominated by silicon particles and is associated with the crack. On the other hand, ductile fracture is characterized by dimples (macroscopic voids) especially at high temperature (Donovan et al., 2015). These voids are associated with fracture of intermetallics in the Al-Si alloys and particle cracking features depend on localized conditions such as particle size, shape, orientation, and activation of dislocation source. Fracture is associated with events of void nucleation and growth with nucleation occurring at coarse constituent particles and secondary phases present in the microstructure (Donovan et al., 2015). Brittle to ductile transition is of importance in the prediction of lifetime of engineering components e.g., transition from transgranular to intergranular fracture is usually followed by a dramatic reduction in ductility and fatigue lifetime. Brittle to ductile transition can occur due to effect of change in

temperature, say from low to high temperature (Donovan et al., 2015). In some coarse microstructures, hard and brittle Fe phases whose bond strength to the matrix is low lead to intergranular fracture failure mode (Zamani, 2015).

2.6 Summary of literature review

Transition metals such as V and Zr have low diffusivity and solubility in Al and have been found to maintain high temperature strength (up to 350 ^{o}C) by forming thermally stable trialuminide compounds. These trialuminides are said to possess an FCC structure which possess high coherency with the matrix at high temperatures. However, trialuminides lower some mechanical properties at room temperature such as ductility. This probes the researcher to want to find out whether addition of other elements, in addition to trialuminides forming transition elements can improve mechanical properties at both room and high temperatures. Additionally, some element's optimal addition levels are known, though not concisely and this even possess a bigger problem when the effect of their combinations is considered. This research therefore seeks to fill this gap by adding Ti, Zr, V, Cr, and Cu to 356 alloys so as to identify their effects on microstructure, tensile properties and fatigue performance.

Modern trends in Al-Si alloys involve addition of elements to suitably alter microstructure, consequently affecting solidification of Al-Si alloys. Some elements promote nucleation of some phases over others while the level of alloying additions, such as the level of Fe, determines the presence or absence of some pre- and post-eutectic phases. Some additions have been found to alter the solidification characteristic temperatures relative to the unmodified base alloys and this may have an effect on the shape of the cooling and derivative curves considerably thus affecting processing temperatures. So far, effects of alloying element additions on solidification characteristics of Al-Si alloys have been studied for Cu, Sr, Mg, Zn, Fe, Na, and low melting point elements. However, while some transition elements added solely and in combination affect solidification behavior considerably, there is no cumulatively tangible mention of their effects on 356 alloys. Regardless, a comprehensive understanding of the interaction between alloying additions is important for simulation, optimal heat treatment schedules and achievement of excellent casting properties. Additionally, most TA software do not have properties of most Al-Si alloys, especially when the additions are customized for a given application. Hence, there is need to update the TA software databases. Again,

since available softwares such as Pandat and FactSage are not able to account for the effect of small quantities of some elements such as Sr, there is need to conduct the actual TA experiments for actual alloys. This study therefore evaluates the sole and combined effects of Ti, Zr, V, Cr, and Cu within the specification limit and solidification rate of ∼0.87 °C/s on the solidification characteristics of Al-7Si-Mg (Cu) alloys.

Mechanical properties of Al-Si-Mg alloys depend on various heat treatment tempers. Some of them include: solution heat treatment temperature and time, quench rate, quench media, and aging time and temperature. High solutionizing temperature leads to higher and faster dissolution, homogenization, and spheroidization and hence reduces solutionizing time. On the other hand, solutionizing time should facilitate dissolution, homogenization, and modification of Si particles. However, too long a time means coarsening of microconstituents and negative impact on fracture elongation and hardening. During quenching, transfer time period of the specimen from the furnace to the quench media should be as short as possible and the quench rate should be chosen to ensure that desired microstructure can be obtained within the shortest acceptable time possible. A slow quenching rate causes detrimental effects such as heterogeneous precipitation of particles during quenching at grain boundaries. Aging temperatures lead to enhanced diffusion and accelerated aging since it increases nucleation and growth rates with low aging temperatures increasing the aging time to peak hardness. Thus, optimum heat treatment parameters and alloying additions are key for desired microstructure-mechanical properties.

Routes to improve tensile properties of A356 alloys include: size and shape modification of eutectic Si particles through: rapid solidification, addition of chemical modifiers, heat treatment or precipitation hardening and a combination of these processes. All tensile test temperatures from 0 - 500 °C register better properties for fine microstructures than for coarse ones (Wang, 2003). Additionally, strength decreases with increase in temperature while ductility increases. Alloying element additions significantly affect microstructural properties and consequently mechanical behavior. For example, increased addition of Fe, combined addition of Ti, V, and Zr and combined Cu and Mg leads to decreased ductility while Mn, Cr, and Sr additions increase elongation. However, literature does not discuss the effect of combined additions of Ti, Zr, V, Cr, and Cu to AlSiMg alloys.

CHAPTER THREE

METHODOLOGY

3.1 Introduction

This research is part of a wider research which involved the following processes: permanent mold (PM) preparation, cast alloys preparation, hot isostatic pressing, T6 heat treatment, tensile, and fatigue tests, microscopy, optical emission spectroscopy (OES), and thermal analysis. Fig. 3.1 diagrammatically depicts these processes and their interrelationship.

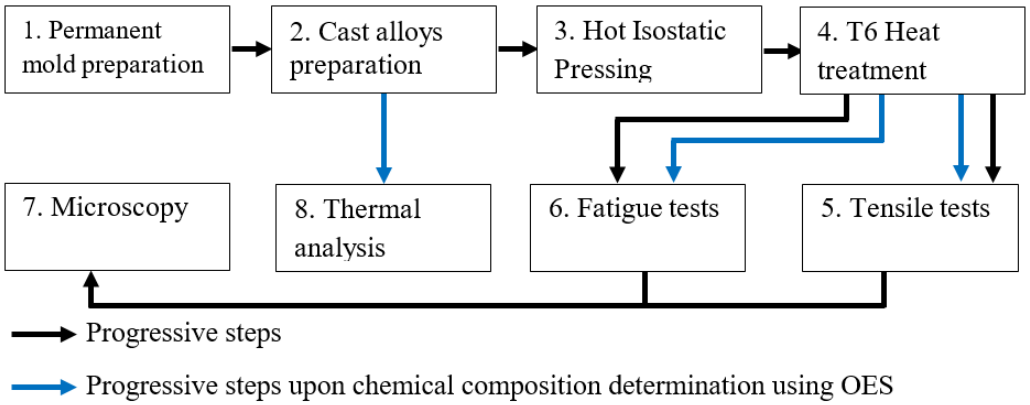

Figure 3.1: Processes undertaken in this research and its wider research

3.2 Experimental procedures

3.2.1 Materials

This research involved conducting OES, microscopy, tensile tests, fatigue tests, and thermal analysis. The alloys investigated were supplied from foregoing work (Ngigi, 2018). More specifically, alloys tested for thermal analysis were provided in as-cast state while those tested for mechanical performance existed as permanent molds that had undergone HIPing and T6 temper heat treatment. OES was conducted to ascertain the chemical compositions of the alloys before any machining or tests. The foregoing work had some similarities to the current work especially on the microscopy, tensile, and fatigue test procedures but these tests were conducted on different alloys in both researches. Thermal analysis was not conducted in the foregoing work but was conducted on as-cast specimens of the alloy types used both in this and the foregoing research. The base alloy 356 was the same for each research but each work's tests and results were analyzed independently. The results of alloy 356 in this research were useful for compar-

ison with test results obtained from its variants. Fatigue and tensile tests were conducted on three alloys unlike TA tests. This was due to shortage of alloys for use but this was not a limitation since the number of specimens used were satisfactory to give a good representative sample of the alloy behavior.

3.2.2 Permanent mold preparation

A computer numerically controlled (CNC) milling machine was used to machine a cast iron permanent mold. The mold design had two halves with a stepped profile and was assembled using screws, see Fig. 3.2.

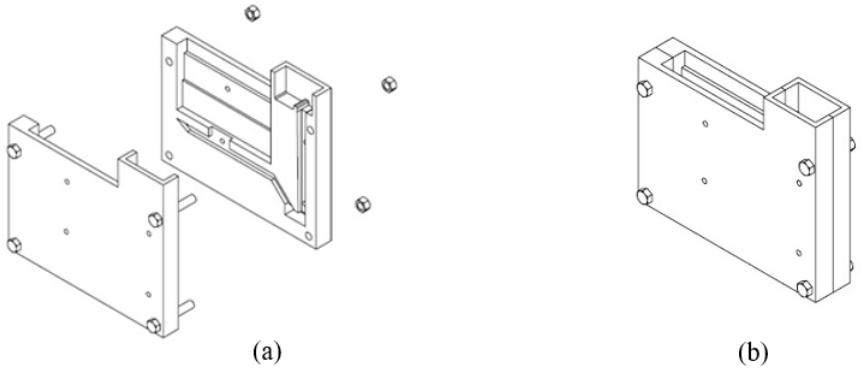

Figure 3.2: Permanent mold: a) Constituent halves b) Assembly (Ngigi, 2018)

3.2.3 Cast alloys preparation

(i) Melting of after-life components, base alloy preparation and chemical composition analysis

The base cast alloy was obtained by melting 70 Kg of selected and cleaned aluminium wheels scrap. The melting was carried out in an oil fired graphite crucible. Cover flux was used during ingot melting, which was done to a temperature of 740 °C. The melt was then skimmed and poured from a preheated ladle into mild steel ingot molds where it was left to solidify for further use.

Table 3.1: Average chemical compositions of 356 alloy's compositions

Alloy	Si	Cu	Mg	Fe	Mn	Cr	Ti	Zr	V	Sr	Others
Base alloy	6.95	0.0887	0.445	0.210	0.158	0.0174	0.0589	0.00403	0.00723	0.0094	-
LM25	6.5-7.5	0.1 max	0.2-0.45	0.5 max	0.3 max	-	0.2 max	-	-	-	-
AC4CH	6.5-7.5	0.1 max	0.2-0.4	0.2 max	0.1 max	0.05 max	0.2 max	-	-	-	-
A356.0	6.5-7.5	0.1 max	0.25-0.45	0.2 max	0.1 max	-	0.2 max	-	-	-	0.1 Zn

*Note: All compositions are in wt.%, single values are maximum limits and the balance is Al and other trace elements such as Pb and Sn in negligible amounts.

Chemical analysis (using Spark OES according to American Society for Testing and Materials (ASTM) standard E1251-17a) involved obtaining a portion of the

molten metal, solidifying it rapidly in cold water in a copper mold based on ASTM specifications E716-94. This was conducted at Numerical Machining Complex (NMC) in Nairobi, Kenya. Table 3.1 shows the chemical composition obtained for the base alloy. It closely resembled a 356 Al-Si alloy as seen in the same table where 356-specimen-alloy compositions are included for confirmation.

The bar casting of the base alloy was prepared by re-melting an ingot in a 5 Kg graphite crucible in an electric muffle furnace. Degassing was achieved by bubbling nitrogen gas through the melt for 15 minutes using a ceramic tube. The melt was then allowed to settle for about 20 minutes after which it was skimmed and poured at 740 ^{o}C into a cast iron mold (see Fig. 3.2) preheated to 495 ^{o}C. A 30 pores per inch ceramic foam filter was used in the filling system of the permanent mold to trap inclusions and minimize on turbulence commonly experienced during pouring. The molten metal then solidified in the PM and Fig. 3.3 shows the bar casting obtained.

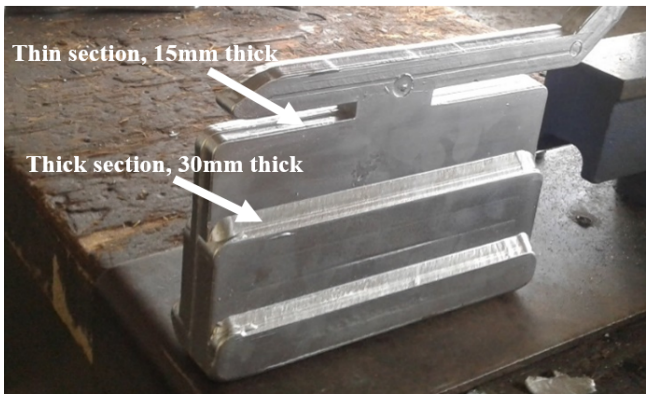

Figure 3.3: Bar casting after melt solidification in permanent mold

(ii) Alloy variants preparation and composition analysis

Initial stages of preparing the bar castings of the alloy variants involved adding master alloys to the base alloy melts and stirring gently to ensure complete dissolution and homogenization. Its important to note that the added elements were supplied in form of Al-50 wt. % Cu, Al-15 wt. % Ti, Al-5 wt. % V, Al-10 wt. % Zr master alloys, Al-10 wt. % Cr briquettes form and Al-10 wt. % Sr rods. The weight of the master alloys that were added was obtained as a division of the product of the percentage of the additive desired multiplied by the weight of the melt divided by the percentage of the element in the master alloy. A sample calculation showing how much Cu- master alloy was added to the base alloy melt is shown in Appendix 1. As was in the base alloy, similar procedures were fol-

lowed till the bar castings of the various base alloy variants were obtained. OES was similarly used to obtain the chemical composition of the alloys. Table 3.2 shows the chemical composition of the base alloy and its variants (obtained by addition of Ti, Zr, V, Cr, and Cu). The codes used to name the base alloy and its variants throughout this research are: 356 = base alloy, X = 0.15%Ti + 0.15%Zr + 0.22%V + 0.015%Sr, TiSr = 0.15%Ti + 0.015%Sr and Cr ≡ 0.15%Cr.

Table 3.2: Chemical composition of the alloys investigated

S. No.	Alloy code	Experimental alloys with the total composition of each additive element in the alloy (wt. %).
1	356	6.95%Si + 0.0887%Cu + 0.445%Mg + 0.210%Fe + 0.158%Mn + 0.0174%Cr + 0.0589%Ti + 0.00403%Zr + 0.00723%V + 00094%Sr
2	356X	356 + 0.15%Ti + 0.15%Zr + 0.25%V + 0.015%Sr
3	356XCr	356 + 0.15%Ti + 0.10%Zr + 0.25%V + 0.015%Sr + 0.15%Cr
4	356TiSr	356 + 0.15% Ti + 0.015%Sr
5	356X0.5CuCr	356 + 0.50%Cu + 0.15%Ti + 0.15%Zr + 0.25%V + 0.015%Sr + 0.15%Cr
6	356X3.5CuCr	356 + 3.50%Cu + 0.15%Ti + 0.15%Zr + 0.25%V + 0.015%Sr + 0.15%Cr

3.2.4 Hot Isostatic Pressing

This process was conducted in a QIH21 uniform rapid cooling (URC^{TM}) machine. It involved subjecting the material to an argon pressurized atmosphere of 150 MPa at a temperature of 500 °C for 3 hours. HIPing was aimed at reducing porosities in the castings to a minimum level such that they would almost be rendered impotent during fatigue testing. This would result in improved mechanical properties.

3.2.5 T6 Heat treatment

The 30 mm thick sections of the bar castings of the alloys produced (Section 3.2.3) were subjected to T6 heat treatment in the Nabertherm® electric muffle furnace (Nabertherm Limited, Germany). The alloys containing copper were solution heat treated for 6 hours at 500 °C to avoid incipient melting of the Cu-rich phases. The non-Cu-containing alloys were solution heat treated at 540 °C for 6 hours. For both cases, upon solutionizing, quenching was done in water at 60 °C followed by immediate aging at 190 °C for 100 hours. Thereafter, the alloys were allowed to cool in air. Heat treatment parameters were informed by literature (Sjolander, 2011; Apelian et al., 1990; Shaha et al., 2015).

The heat treated bar castings were then machined such that the tensile, fatigue, and thermal analysis, not to mention microscopy, samples were obtained from the 30mm thick section.

3.2.6 Fatigue tests

Fatigue tests were conducted at room temperature (25 °C) using an SM1090 rotating-bending fatigue machine and its VDAS (TecQuipment Limited, UK).

The standard for machining fatigue test specimen and the procedure for obtaining the fatigue strength are discussed below.

(i) Specimen preparation

Fatigue specimen blanks were obtained from permanent mold castings of alloys 356, 356X, and 356XCr. Specimens were machined to the ASTM E606 standard using a CNC lathe machine located at Numerical Machining Complex (NMC). The specimen dimensions are depicted in Fig. 3.4. Eight specimens, for each alloy tested, were precisely machined from the respective bar castings.

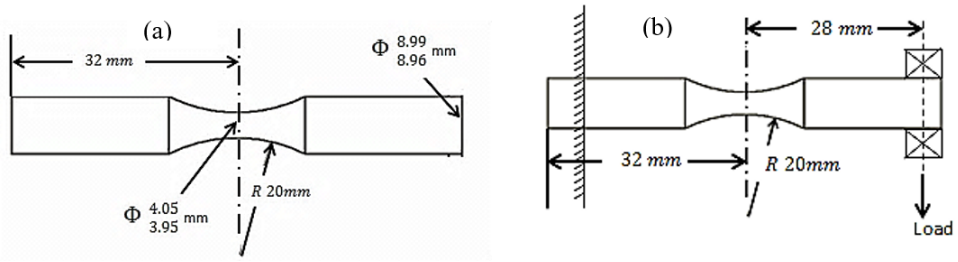

Figure 3.4: Fatigue test specimen: (a) dimensions; (b) upon mounting between fixed end near the motor and free end at bearings.

(ii) Fatigue strength measurements

Each fatigue specimen was clamped as a cantilever beam whereby the end towards the motor offered a fixed end with the bearing side acting as the free end. This is illustrated in Fig. 3.4(b). The consequence of a rotation on a cantilever beam was alternating compressive and tensile stresses at any point along the unclamped portion of the specimen. Each cycle was composed of a point moving from zero stress to a maximum tension followed by a zero stress to a maximum compression and finally back to the zero stress leading to a repeated cycle (two reversals).

The staircase method, whose evaluation is a fail or pass criteria, was adopted for these set of tests. First, a limit of the number of cycles to be covered to warrant a survival or a failure was decided upon as 10^7 cycles. This made it possible to determine the fatigue strength of these alloys at 10^7 cycles. Specimens were tested one after the other with the first test stress chosen based on a median stress estimated by Ngigi (2018) following the alloy similarities in chemical composition and the desirable results obtained using staircase method. In this case, initial stress used was $\sim$75 MPa for all alloys tested (356, 356X, and 356XCr). This was a close approximation aimed at avoiding recurrent failures due to overestimation of stress and to minimize recurrent runouts over a couple of tests due to under-

estimation of the mean fatigue strength. A uniform stress interval (increment or decrement value) of 9 MPa was also chosen based on experiments performed previously on a similar set of alloys (Ngigi, 2018). If the first specimen failed before the stipulated 10^7 cycles, the next was tested at a stress one increment (step size) lower and if it survived the set number of cycles (runout), it was discarded and the next tested at a stress one increment higher. This was done for the subsequent specimen with the one tested prior to the next being the basis of judgment for the test stress of the next specimen. This was such that the number of specimens (8 per alloy), was a sum of the number of failures and runouts.

It is important to note that fatigue tests of all specimens were conducted at a frequency of 60 Hz which was sufficient to conduct the high cycle fatigue tests of a threshold of 10 million cycles. This choice has no effect on the stress levels investigated. Rather, it only affects the speed of conducting the tests. The conditions that the test results should fulfill for this method to be eligibly used are clearly reported by Pollak (2005), making it fruitless to repeat them here. Fig. 3.5 illustrates the fatigue testing procedure which is outlined thereafter. Fig. 3.6 shows specimens that failed before reaching 10^7 cycles while Fig. 3.7 illustrates the fatigue tests set-up.

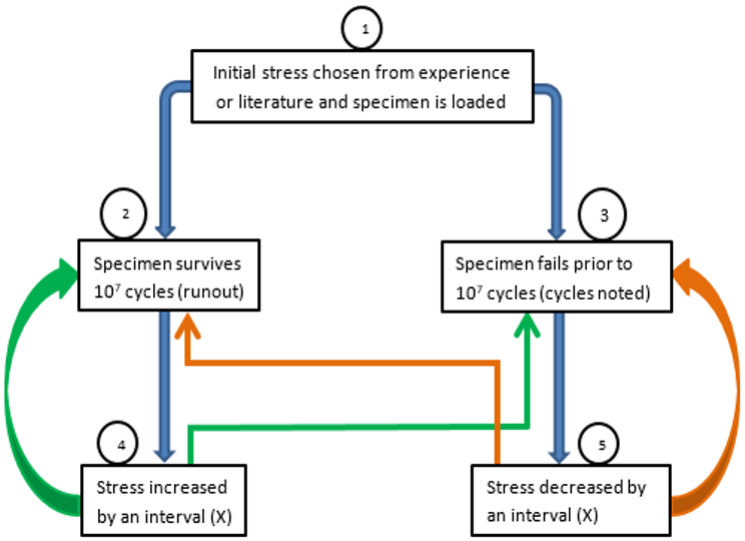

Figure 3.5: Block diagram of the staircase method

1: Initial stress is chosen and specimen is loaded.
Outcome: Specimen survives 10^7 cycles and moves to 2 or fails prior to 10^7 cycles and moves to 3.

2: Upon specimen outcome being a runout at 2, stress is increased by an interval.

Outcome: Specimen either survives 10^7 cycles (runout) and goes back to step 2 and back to 4 or specimen fails prior to 10^7 cycles and goes to step 3 then 5.

3: Upon specimen outcome being a failure, stress is decreased by an interval. Outcome: Specimen either survives 10^7 cycles (runout) and goes from step 5 to 2 then to 4 or specimen fails prior to 10^7 cycles and goes from step 5 and back to 3.

These sequences of steps are followed accordingly till all the specimens of a given alloy are tested with all alloy tests beginning at step 1.

Figure 3.6: Failed specimens before 10^7 cycles during the experiment

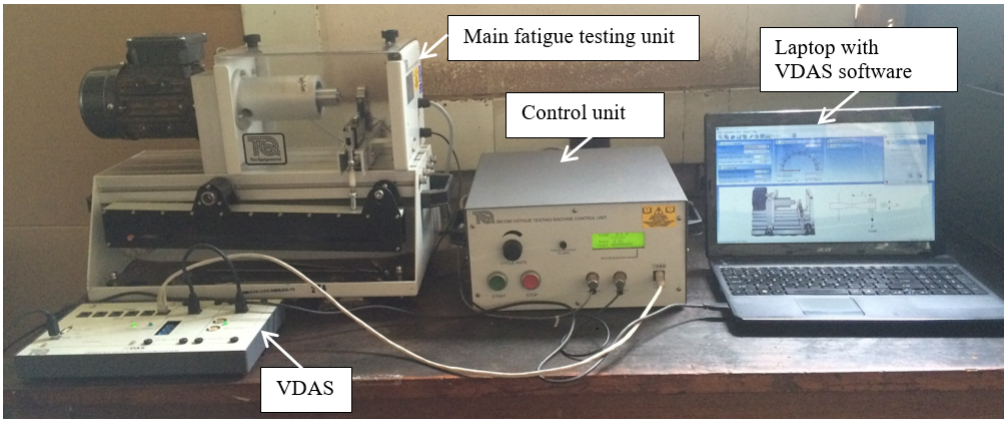

Figure 3.7: Rotating fatigue testing setup

3.2.7 Thermal analysis

TA specimens (the base alloy 356 and its variants) were obtained from permanent mold castings of alloys listed in Table 3.2 (serial number 1 to 6). 100 g of the as-cast alloys were tested. These alloys were melted in an ELSKLO s.r.o. electric resistance furnace (Elsklo Limited, Czech Republic) see Fig. 3.8, each in turn, to a temperature of 730 $\pm$ 5 ^{o}C (most precipitates have dissolved).

K type thermocouples (each 5 mm outside sheath diameter and 50 mm probe length) were tempered for at least 15 minutes in the furnace before use to minimize

on inaccuracies observed in most new thermocouples. The thermocouples were calibrated several times using 99.999% pure aluminium before any measurement was taken to ensure consistency, accuracy, and reliability of the results. In order to conduct calibration, the thermocouples were inserted in molten aluminium °C and solidification temperatures from the resultant cooling curve were noted. The deviation between the thermocouple reading and the theoretical value gave the error margin which stated the thermocouple accuracy.

Figure 3.8: ELSKLO s.r.o. furnace

A graphite crucible (inner diameter 60 mm, height 65 mm, and thickness 5 mm) characterised by high refractoriness, was preheated to 300 - 350 °C for 15 minutes. This was done simultaneously while the melt approached 730 °C ± 5 °C . This way, thermal equilibrium upon pouring of the melt was possible since preheating reduced nucleation instances before thermal balance of the entire setup.

The molten aluminium was then poured inside the preheated graphite crucible that was placed on top of a 6 mm thick ceramic insulation material (Fig. 3.9). The specimen size was such that only one reaction occurred at a time and this was confirmed by the change in temperature between the near wall (T_w) and the centre (T_c) thermocouple i.e; $\triangle T = T_w - T_c$, that was consistently less than 8 °C. This inhibited insufficient resolution caused by overlapping reactions that would cause difficulty in distinguishing the different reactions.

A specimen size of more than 10 mm was chosen since the region of non-steady state hardly exceeds 5 mm radially. Similarly, for a small crucible, the thermocouple provides a sink around it which disturbs the readings. Further, decreasing specimen size increases sensitivity for disturbance and limits possibility to approach steady state growth because wall temperatures quickly approach central region temperature. The graphite crucible was also covered at the top with the 6 mm thick ceramic insulating material upon pouring of the molten alloy, setting, and inserting of the thermocouples in the melt. The thermocouples were

clamped in such a manner that one was located at the center and the other near the wall of the graphite crucible. These thermocouples were connected to a high resolution data logger which was connected to a laptop installed with DATAQ Instruments Software Manager to facilitate recording of temperature decrease with time during solidification of each alloy.

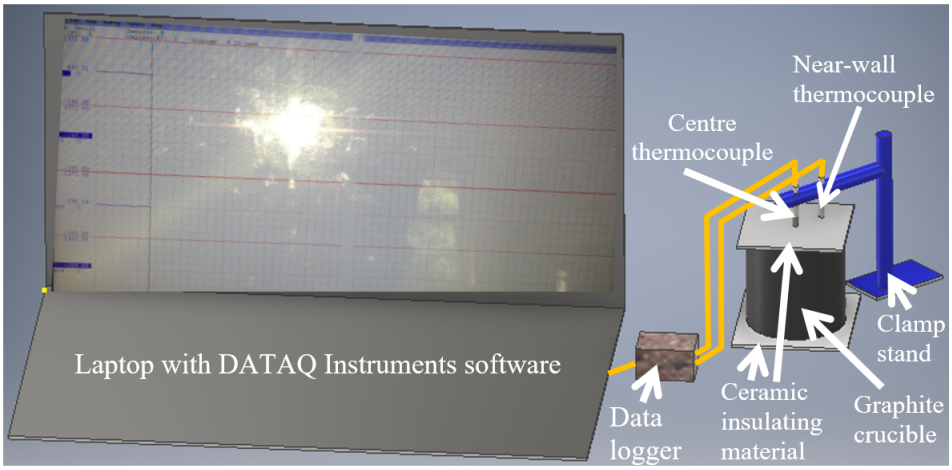

Figure 3.9: Experimental set up for thermal analysis

3.2.8 Tensile tests

Both room temperature (25 °C) and high temperature (237 °C) tests were conducted using an Instron® 300DX universal testing machine (Instron, Canada - USA). The tensile testing machine was interfaced with a computer that converted the information obtained from the tests to a form that can be analyzed (load and extension). The standard used to prepare tensile specimens and the procedure followed for tests are discussed in the subsections below.

(i) Specimen preparation

Tensile specimen blanks obtained from permanent mold castings of alloys 356, 356X, and 356XCr were machined to ASTM B557M-02a standard (Fig. 3.10). Six tensile specimens, for each alloy tested, were precisely machined from the respective bar castings. Of the six specimens available from each alloy, three were tested at room temperature (RT) and three at high temperature (HT). The reduced uniform section along the entire gauge length of the standard specimen facilitated fracture occurrence within this gauge rather than within the gripping threaded ends which may be high stress concentration points ideal for premature tensile failure. The specimen was threaded at the ends (M10x1.25) to prevent sliding or fracture at the gripped section. The machine had holding grips used

to mount the specimen by its ends. Loading constantly elongated the specimen with the measure of the instantaneous applied load and the consequent elongation measured by the load cell and the extensometer respectively.

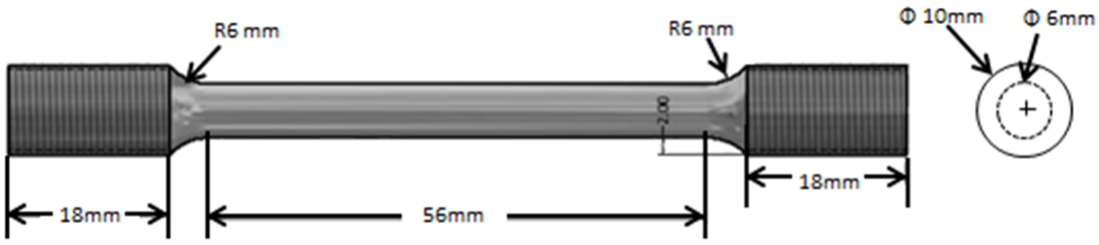

Figure 3.10: Tensile test specimen

(ii) Room temperature tests (25 °C)

Each threaded specimen was placed in the threaded holders of the machine for a firm grip during tests. A crosshead speed of 1 mm/min was employed. The specimen temperature was sensed by a thermocouple whose tip was located in a hole on the smallest cross-section of the specimen. This was done for one representative specimen based on the assumption that for each specimen, isothermal properties existed both lengthwise and circumferentially.

(iii) High temperature tests (237 °C)

This test was similar to that conducted at low temperature. However, for high temperature tests, an SF-16 split furnace, with a heat zone of up to 1200 °C, was first heated for 30 minutes from room temperature to a set maximum temperature of 300 °C. Thermocouples attached to the gauge section of the specimens were employed in temperature determination. Upon attainment of this set temperature, the test specimen was mounted. The test commenced 20 minutes after mounting to allow for: reference temperature determination and ascertaining of the isothermal characteristic of the entire specimen. Strains at high temperature tests were obtained using an Instron model RT-214 high-temperature extensometer. This way, tensile properties were obtained and recorded.

3.2.9 Microscopy

Specimens used were obtained from tensile and fatigue specimens.

(i) Optical microscopy (OM)

The specimens were cut along the cross section using a South Bay Technology low speed diamond wheel cutter (Model 650 CE), Fig. 3.11(a). Cutting was done

at a low speed (micrometer feed of 0.01 mm increments) to minimize structural deformations and a coolant was used to prevent overheating.

Upon cutting, the specimens were cold mounted, each in turn, in epoxy resin. This was aimed at facilitating easy handling of the small-sized specimens (Fig. 3.11(b)). This was followed by grinding and polishing which was conducted on the Leco Spectrum system ^{TM} 1000) machine (Leco Corporation, USA) shown in Fig. 3.12. Grinding was done using successively finer grits of the Silicon carbide paper i.e. 800, 1000, and 1200 grit so as to remove material from the specimen surfaces. This was accomplished using the largest possible grain size interval to reduce time used and to minimize material damage. Care was taken to ensure scratches from each previous step was completely eliminated before the next step with preparation times made as short as possible. Table 3.3 shows parameters used as advised by Struers website; www.struers.com/en (Struers).

Table 3.3: Specimen metalogram

	Grinding		Polishing			
Surface	SiC paper	SiC paper	MD/DP -Mol/Dur /Sat/Floc/Dac	MD/DP -Mol/ Dur/Sat/Floc/Dac	MD/DP - Nap	MD/DP - Nap
Abrasive	SiC	SiC	Diamond	Diamond	Diamond	OPS
Grain size	800 grit	1200 grit	6 μm	3 μm	1 μm	0.04 μm
Lubricant	Water	Water	Blue	Red	Red	None
rpm	300	300	150	150	150	150
Force (N) /specimen	30	30	35	25	25	8
Time (Min)	Until plane	3	5	3	3	15

Polishing cloths impregnated with 6 μm, 3 μm, 1 μm and finally 0.25 μm diamond pastes were then used. Hands and specimens were washed using clean flowing water after each step. The finest polish was obtained using 0.04 μm oxide particle suspension. The specimen was then dried using a drier followed by dirt elimination by swabbing the surface with cotton wetted with methanol.

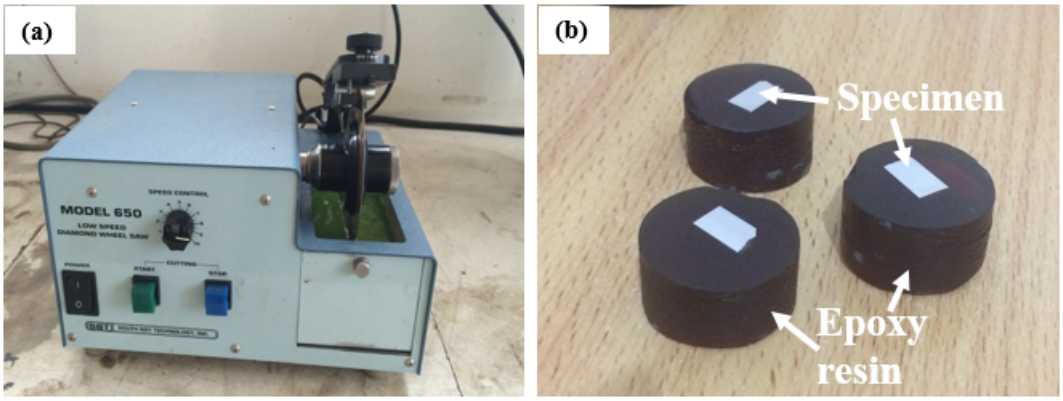

Figure 3.11: (a) South Bay Technology low speed diamond wheel cutter; (b) Specimens mounted in epoxy resin

Figure 3.12: Leco machine used for automatic grinding and polishing

A BX 41M Olympus microscope (Olympus, Tokyo - Japan) was used to obtain optical micrographs at desired magnifications. Optical images were taken with an aim of facilitating: basic microstructural characterization, quantitative particle analysis and SDAS determination. Basic microstructural characterization was conducted on the micrographs obtained at various magnifications. ImageJ software was used for particle characterization, more specifically to obtain the particle area, maximum Feret dimensions, circularity, and aspect ratio (AR) of 10 images per alloy specimen. Minitab was used to analyze ImageJ data. The micrographs were calibrated using a graticule (a scale of 1 division = 0.01 mm) to increase accuracy of measures obtained. The SDAS was determined using the linear intercept method whereby a straight line was randomly drawn across a calibrated micrograph with several dendrites lying along the line. The length of the line was then divided by the number of dendrites lying along the line to give the SDAS. The micrographs used for SDAS determination and quantitative analysis were obtained at a magnification of 50X.

(ii) Scanning Electron Microscopy

Mounting of specimens for fractography was done in bakelite resin followed by cutting perpendicular to the fractured surface. This was followed by grinding and polishing to 0.04 μm OPS finish as was in OM.

Scanning Electron Microscopy (SEM) was conducted using a A Carl Zeiss LEO 1525 Field Emission Gun SEM (Carl Zeiss Microscopy Limited, Germany). The

parameters used were: an accelerating voltage of 20 kV, a beam current of 10 μA and a working distance of 15 mm. An Oxford Aztec Energy dispersive spectroscopy (EDS) detector (Oxford Instruments, UK) was used for detection of x-rays produced from the specimens, creation of elemental maps and for secondary phase analysis using the spot analysis technique.

CHAPTER FOUR

RESULTS AND DISCUSSION

In this section, results and relevant discussions on microstructural, mechanical and solidification characteristics of the alloys in Table 3.2 are presented. First, the microscopy results are presented followed by thermal analysis findings, tensile, and finally fatigue.

4.1 Microscopy

In this section, the microscopy results of alloys 356, 356X, and 356XCr are presented together with their discussion. First, OM and SEM microstructures, elemental maps, spot analysis and EDS spectra are presented followed by quantitative microstructural analysis.

4.1.1 OM and SEM

Basic microstructural features were observed from OM micrographs. The elemental maps were used to show the elements present in each respective mapping (using color codes) and these maps were in-turn used to confirm presence of alloying additions and OM constituents such as intermetallics. Some spots on SEM micrographs were identified and their EDS spectra generated to facilitate chemical characterization of phases. However, the exact stoichiometry of the intermetallics was not determined because the SEM used was devoid of known composition databases against which the identified phases could be compared for accuracy. However, this did not limit this research since the elemental maps gave sufficient information on elements present. The effects of the constituents of the micrographs are discussed in detail under fatigue and tensile performance.

(i) Alloy 356

Primary α-aluminium matrix formed the largest portion of the microstructure. Si particles assumed a coarse plate-like appearance and were randomly distributed within the Al-matrix in interchanges with intermetallics as in Figs. 4.1 and 4.2. Some specific chemical compositions of these intermetallics are clearly delineated in the SEM images presented hereafter. The alloy was unmodified and lack of well-defined dendrite arms that resulted made it impossible to measure SDAS.

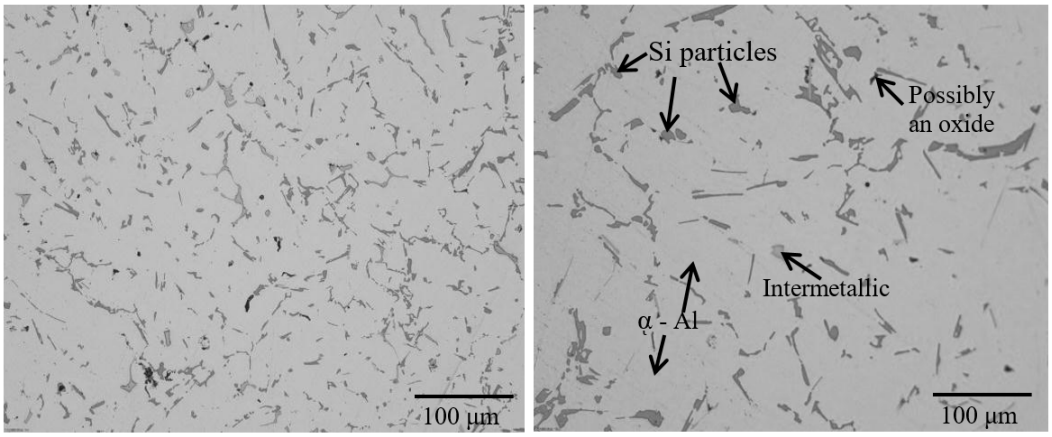

(a) (b)

Figure 4.1: Optical micrographs depicting the constituents of alloy 356's unmodified microstructure: (a) 10X; (b) 20X

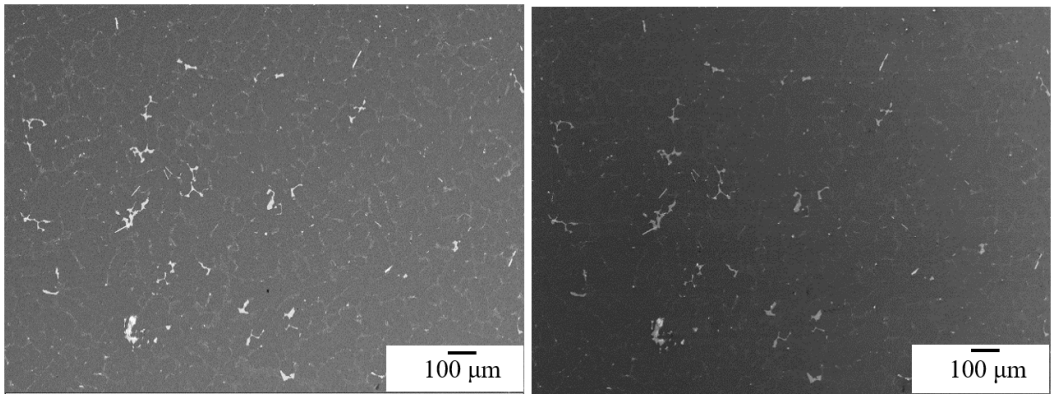

(a) (b)

Figure 4.2: SEM micrographs of alloy 356 in BSE and SE mode: (a) 150X – BSE; (b) 150X – SE

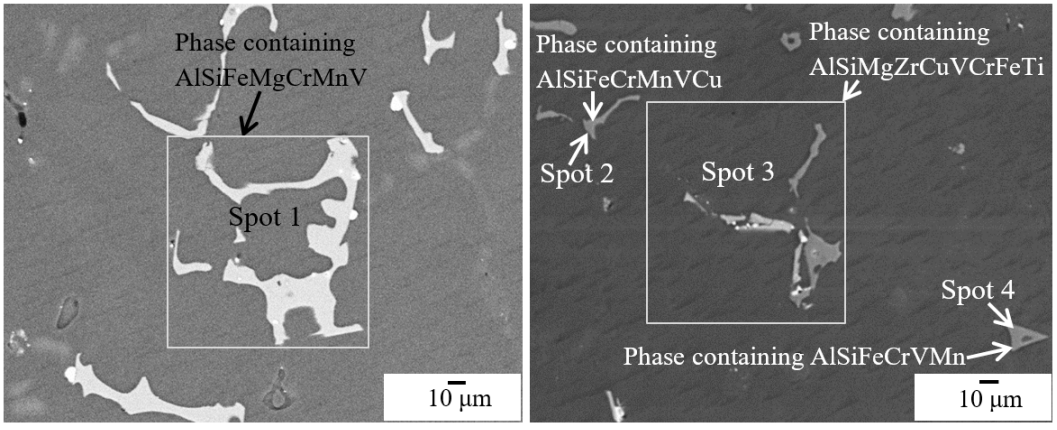

(a) (b)

Figure 4.3: SEM micrographs showing some phases identified by EDS spot analysis (1000X) for alloy 356

The SEM images in Fig. 4.3 show some phases identified by EDS spot analysis. The EDS spectra for the spots identified in Fig. 4.3 are shown in Fig. 4.4 with each having details of each spot's elemental composition in form of peaks as identified by SEM spot analysis.

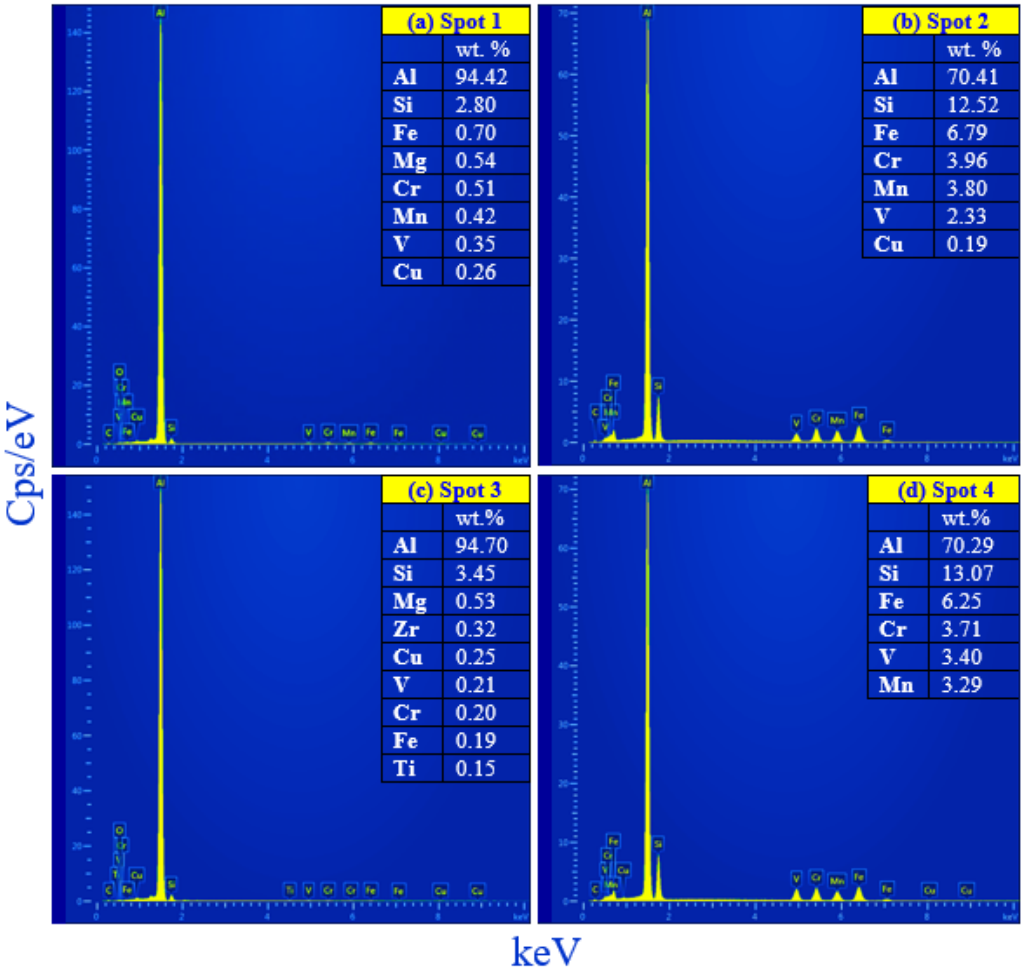

Figure 4.4: EDS spectra of alloy 356 showing compositions of the various elemental phase constituents in form of peaks as identified by SEM spot analysis.

Examples of phases present, in terms of their decreasing order of elemental components, include: Al-Si-Fe-Mg-Cr-Mn-V-Cu, Al-Si-Fe-Cr-Mn-V-Cu, Al-Si-Mg-Zr-Cu-V-Cr-Fe-Ti, and Al-Si-Fe-Cr-V-Mn. Based on this representative sample, it can be deduced that some Fe-, V-, and Cr-containing phases are present in this alloy. Some Mg- and Cu-containing phases are also present indicating the effect of solutionizing. Its important to note that for the randomly analyzed spots, the elemental compositions are higher in some spots compared to others. This is due to the area of the analyzed spots whereby seemingly larger areas (spot 1 and 3)

contained higher elemental quantities than smaller one (spot 2 and 4). However, this does not affect the analysis since the alloy constituents were homogeneously prepared as it was discussed in section 3.2.3.

(ii) Alloy 356X

This alloy differed from alloy 356 by additional alloying elements, cumulatively denoted as X. Si particles were modified (large coarse platelets transformed to fine acicular particles) due to addition of Sr whereas Ti and Zr addition promoted formation of small regularly shaped grains. This alloy was dominated by well-defined dendrite arms with intermetallics coexisting within the α-Al dendritic matrix (Figs. 4.5 and 4.6). This alloy had an SDAS of 45μm.

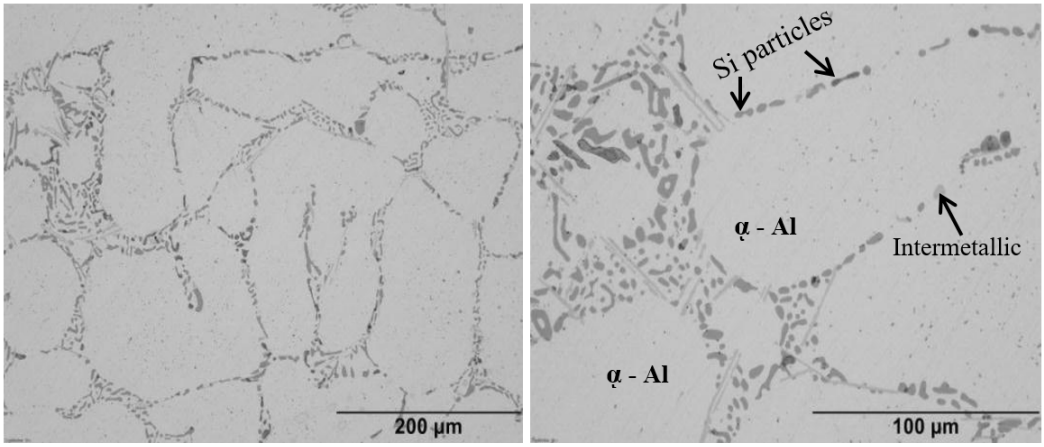

(a) (b)

Figure 4.5: Optical micrographs of alloy 356X depicting its defined dendrite arms and other features (a) 20X; (b) 50X

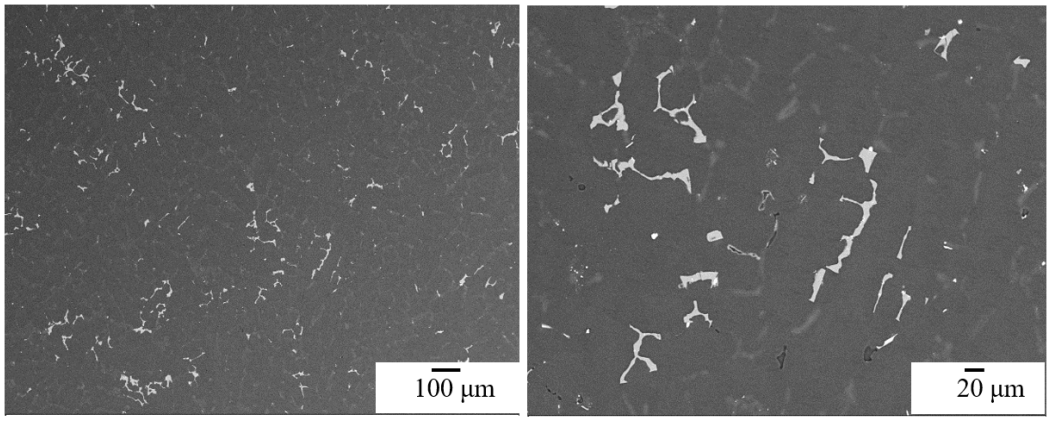

(a) (b)

Figure 4.6: SEM micrographs of alloy 356X taken in BSE and SE mode: (a) 150X – BSE; (b) 500X – BSE

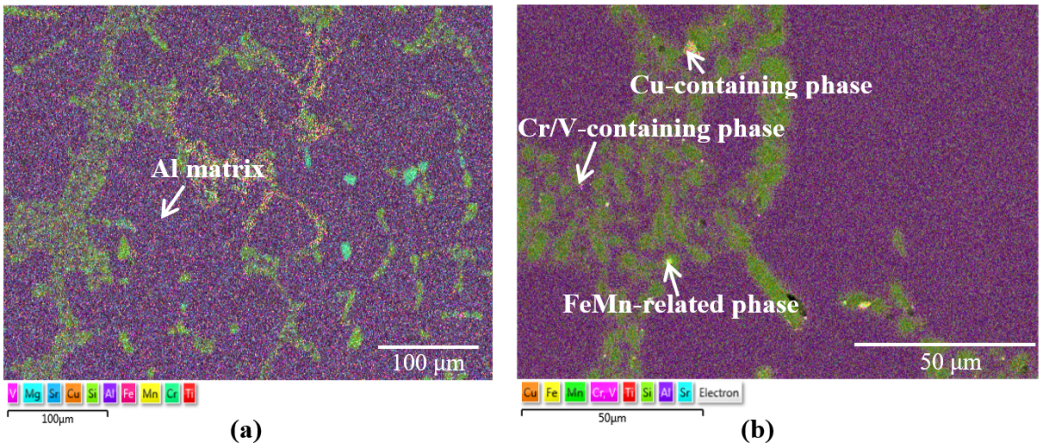

(a) (b)

Figure 4.7: Elemental EDS maps delineating some elemental phase compositions in investigated portions of alloy 356X.

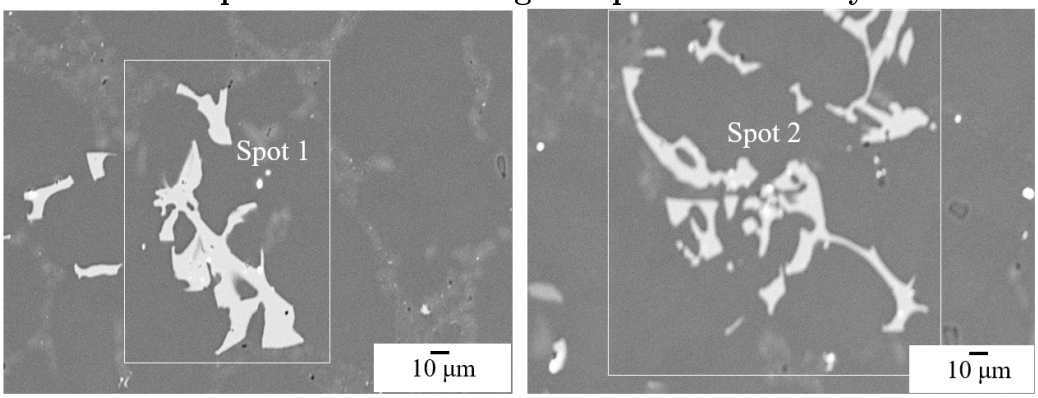

(a) (b)

Figure 4.8: Spot analysis of an SEM micrographs of alloy 356X taken in BSE mode: (a) 1000X; (b) 1000X

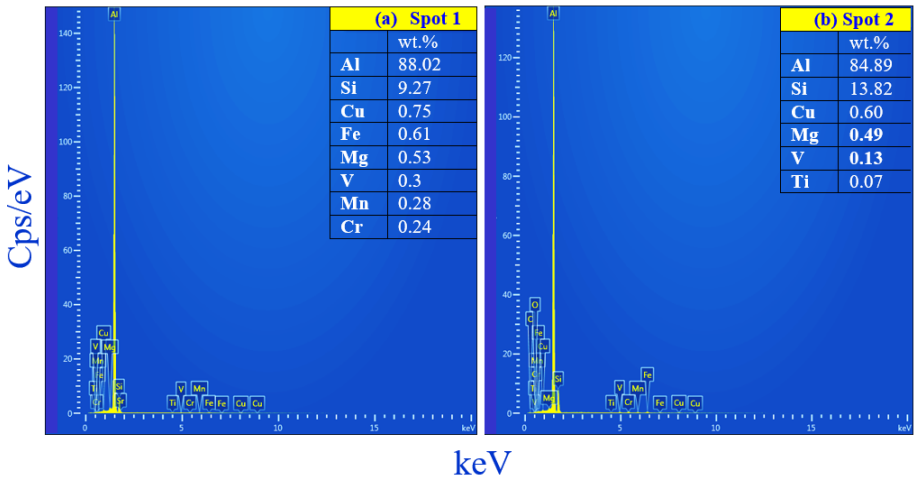

Figure 4.9: EDS spectra of alloy 356X showing compositions of elemental phase constituents identified by SEM spot analysis.

The elemental maps in Fig. 4.7 show the presence of some alloying elements such as V. Based on SEM images in conjunction with EDS spot analysis as shown in Figs. 4.8 and 4.9, Al-Si-Cu-Fe-Mg-V-Mn-Cr and Al-Si-Cu-Mg-V-Ti containing phases exist in alloy 356X. Thus, Cu-, Mg- and V- containing phases are present and so are Ti- and V- but in relatively small quantities.

(iii) Alloy 356XCr

This alloy differs from alloy 356X, in chemical composition, by an additional 0.15%Cr. Its microstructure is governed by intermetallics and eutectic silicon particles with fine fibrous morphology within an α-Al dendritic matrix. The alloy had a modified microstructure due to the effect of Sr in the alloy and was also grain refined. This alloy had an SDAS of 40μm. Its optically identified microstructural features are illustrated in Fig. 4.10 while its SEM micrographs in BSE and SE mode are shown in Fig. 4.11. Fig. 4.12 shows the elemental EDS map with various color codes indicating the existence of various elements present in alloy 356XCr. Existing elements in addition to the basic Al and Si include but are not limited to: Ti, V, and Mg. Figs. 4.13 and 4.14 show the phases identified in alloy 356XCr with the elemental composition indicated for each spot. Existing elements in addition to the basic Al and Si include but are not limited to: Ti-, V-, and Zr-. However, Cr-containing phases are not noticed despite its addition to this alloy. This is due to the randomness in obtaining the spots.

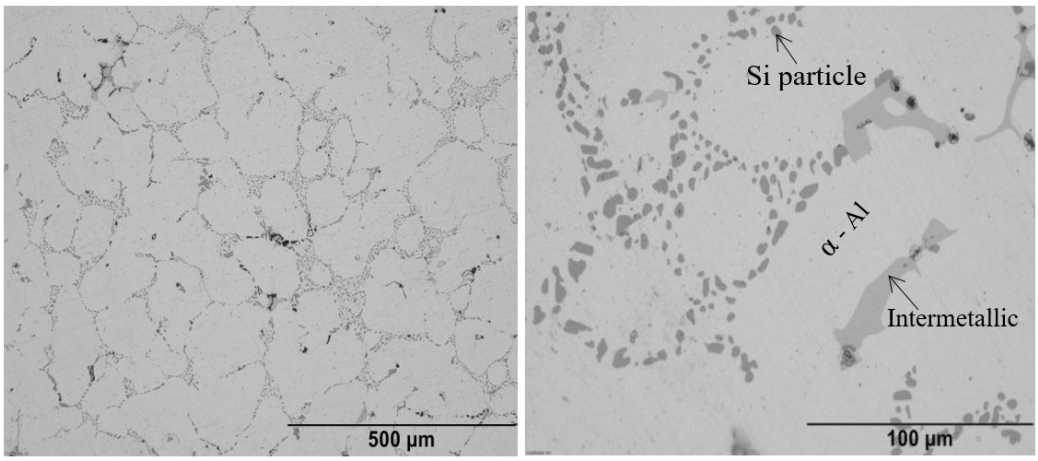

Figure 4.10: Optical micrographs of alloy 356XCr depicting its microstructural features including its well-defined dendrite arms: (a) 10X (b) 50X

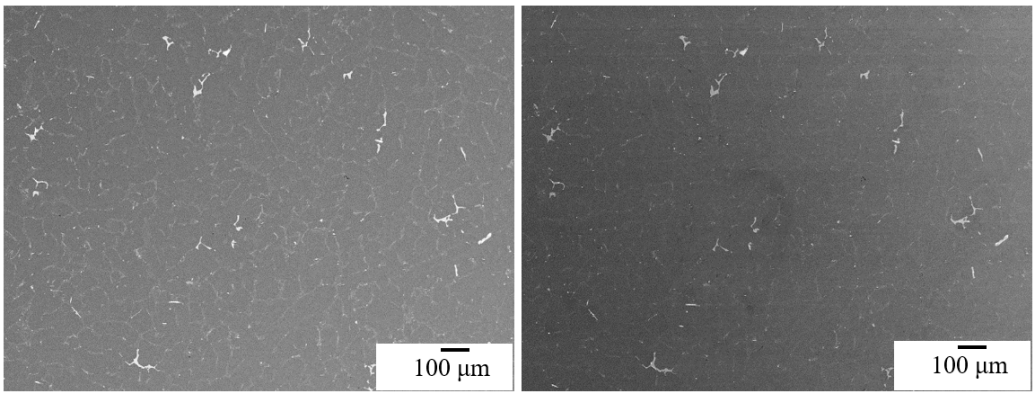

(a) (b)

Figure 4.11: SEM micrographs for alloy 356XCr in BSE and SE mode: (a) 150X-BSE; (b) 150X-SE

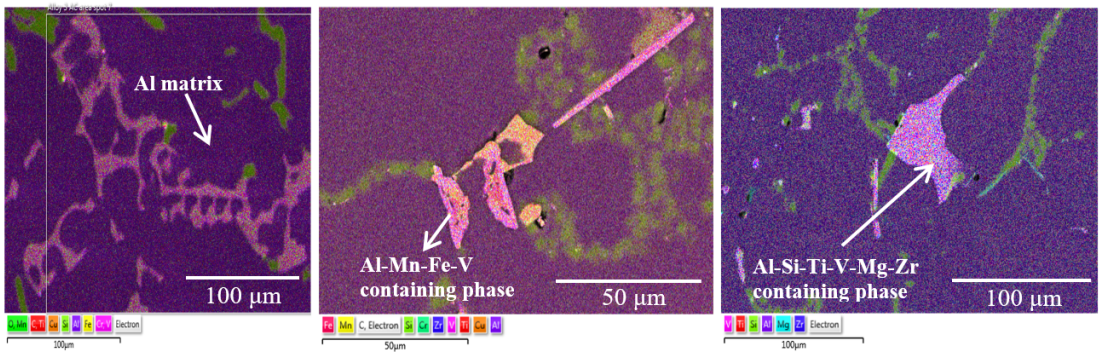

(a) (b) (c)

Figure 4.12: Elemental EDS map delineating the various elemental phase compositions present in alloy 356XCr.

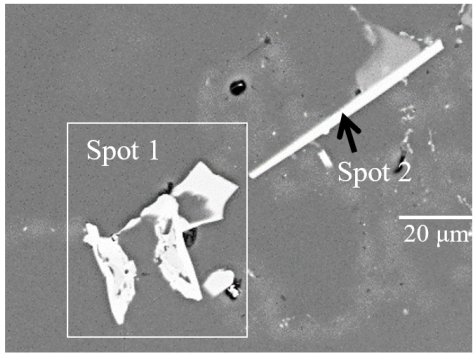

Figure 4.13: SEM micrograph of alloy 356XCr, showing some phases identified by EDS spot analysis at 2000X

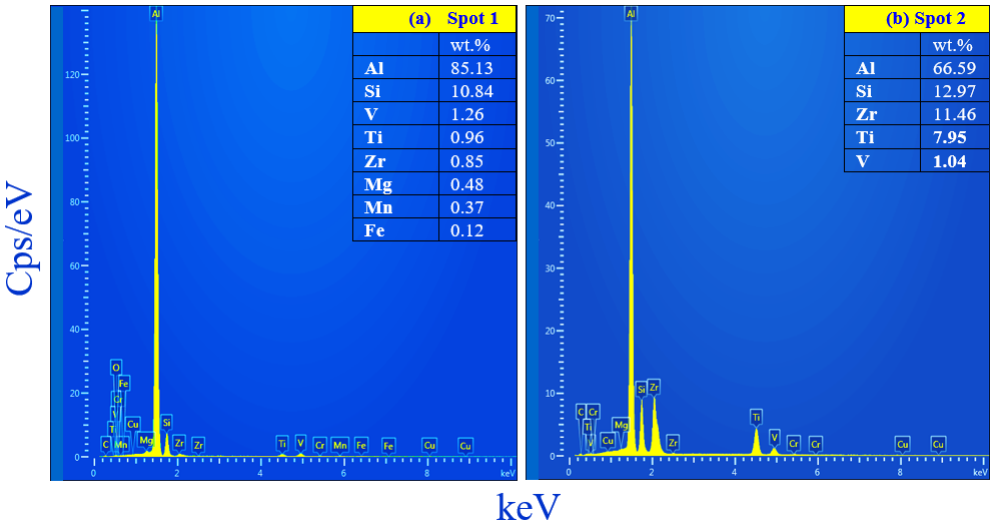

Figure 4.14: SEM spectra for alloy 356XCr showing elemental phase constituents identified by SEM spot analysis and their individual elemental composition

4.1.2 Quantitative microstructural analysis

This section covers the discussion on probability plots and scatter plots of alloys 356, 356X, and 356XCr. Optical micrographs of these alloys taken at X50 were used to obtain particle characteristics in conjunction with "ImageJ" software. Particle area data was fitted in three statistical distribution plots namely 3-Parameter Lognormal, 3-Parameter Weibull, and Largest extreme value probability plots as illustrated in Figs. 4.15 to 4.17. Cumulative distribution plots of various shape aspects were plotted (Fig. 4.18). Scatter plots were also plotted to show the correlation between various shape aspects (Figs. 4.19 to 4.24).

(i) Probability plots

Using the criteria reported and discussed by Ngigi (2018), the particle data was not normally distributed. This made it necessary to make probability plots of the particle area, a particle characteristic that significantly affects fatigue and tensile properties. Three probability plots were chosen: 3-Parameter Lognormal, 3-Parameter Weibull, and Gumbel probability plots. These extreme value distributions were used because it is reported by Mbuya (2011) and Tiryakioglu (2008), that the larger the particle, the higher its potency in initiating cracks. Upon fitting the particle area data to the mentioned statistical distributions, the best fit was determined based on the Anderson Darling (AD) goodness of fit Mbuya (2011), value (preferably be less than unity). This was so because as much as probability plots can have their axes transformed to provide a linear relationship

for data suited for a given distribution, they are subjective and inadequate to approve a hypothesis that a particular data set came from a particular distribution. This called for a complement like the AD goodness–of-fit. The AD value was also used as a recommended test static because of its sensitivity to the tails of distributions and its superiority to other goodness of fit tests for a variety of distributions as reported by Tiryakioglu (2008).

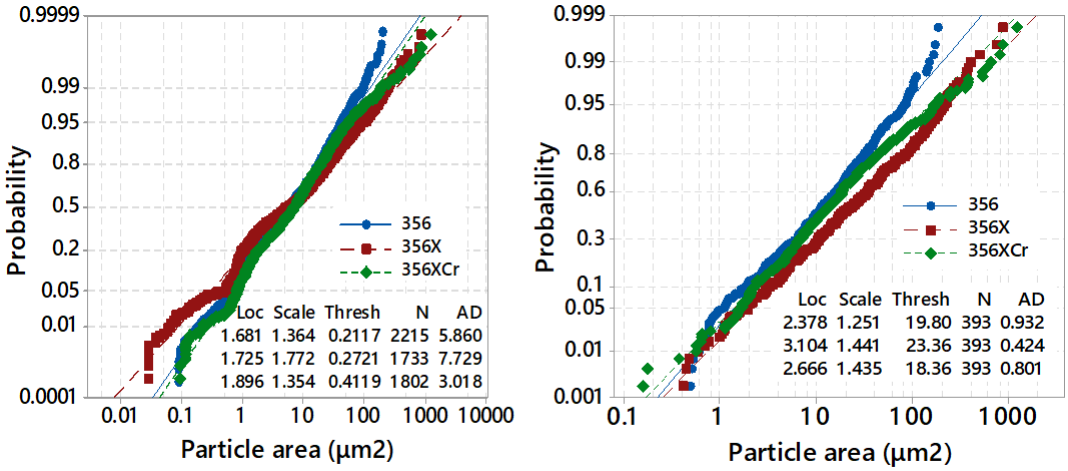

Figure 4.15: 3-Parameter Lognormal probability plots: (a)for all alloy particles; (b) for intermetallic particles that lie within 0.1% of the largest particle areas

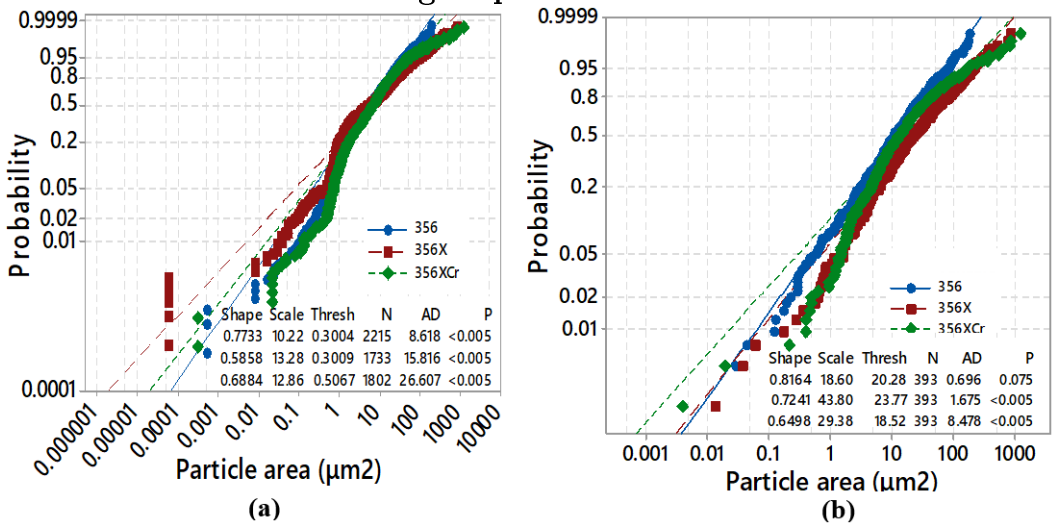

Figure 4.16: (a) 3-Parameter Weibull probability plots for: (a)all alloy particles; (b)intermetallic particles that lie within 0.1% of the largest particle areas

The whole population of the particle area data for alloys 356, 356X, and 356XCr fitted best in the 3-parameter lognormal distribution plot. It also fit perfectly for 0.1% of the largest particle areas. 3-parameter Weibull and largest extreme

value statistical distribution plots did not provide acceptable fits for both cases. The AD values of the 3-parameter lognormal distribution are closest to unity compared to those of the 3-parameter Weibull and largest extreme value (Figs. 4.15 to 4.17). The AD values for the 3-parameter lognormal probability plots are less than 1 for 0.1% of the largest particle areas making it the most suitable plot to represent the particle area population of these set of alloys.

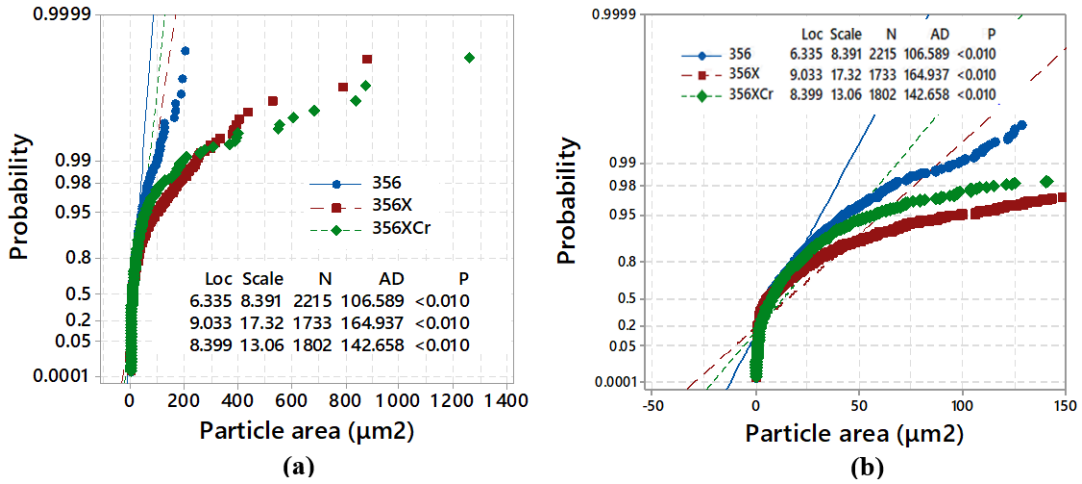

Figure 4.17: (a) Largest extreme value probability plots for:(a)all alloy particles; (b) intermetallic particles that lie within 0.1% of the largest particle areas

(ii) Cumulative distribution plots

Particle aspects used to make these plots and others are: circularity, AR, d_{eq}, and maximum Feret dimension (described by equations 4.1 to 4.3). Equations 4.1 and 4.3 are reported by Mbuya (2011), while 4.2 is derived from 4.1.

$$Circularity = \frac{4\pi A}{p^2} \tag{4.1}$$

$$Equivalent\ particle\ diameter\ (d_{eq}) = 2\sqrt{\frac{A}{\pi}} \tag{4.2}$$

$$Aspect\ ratio\ (AR) = \frac{a}{b} \tag{4.3}$$

Where: A, and p are the particle area and perimeter respectively; a and b are major and minor axes of an ellipse that a particle can fit into respectively.

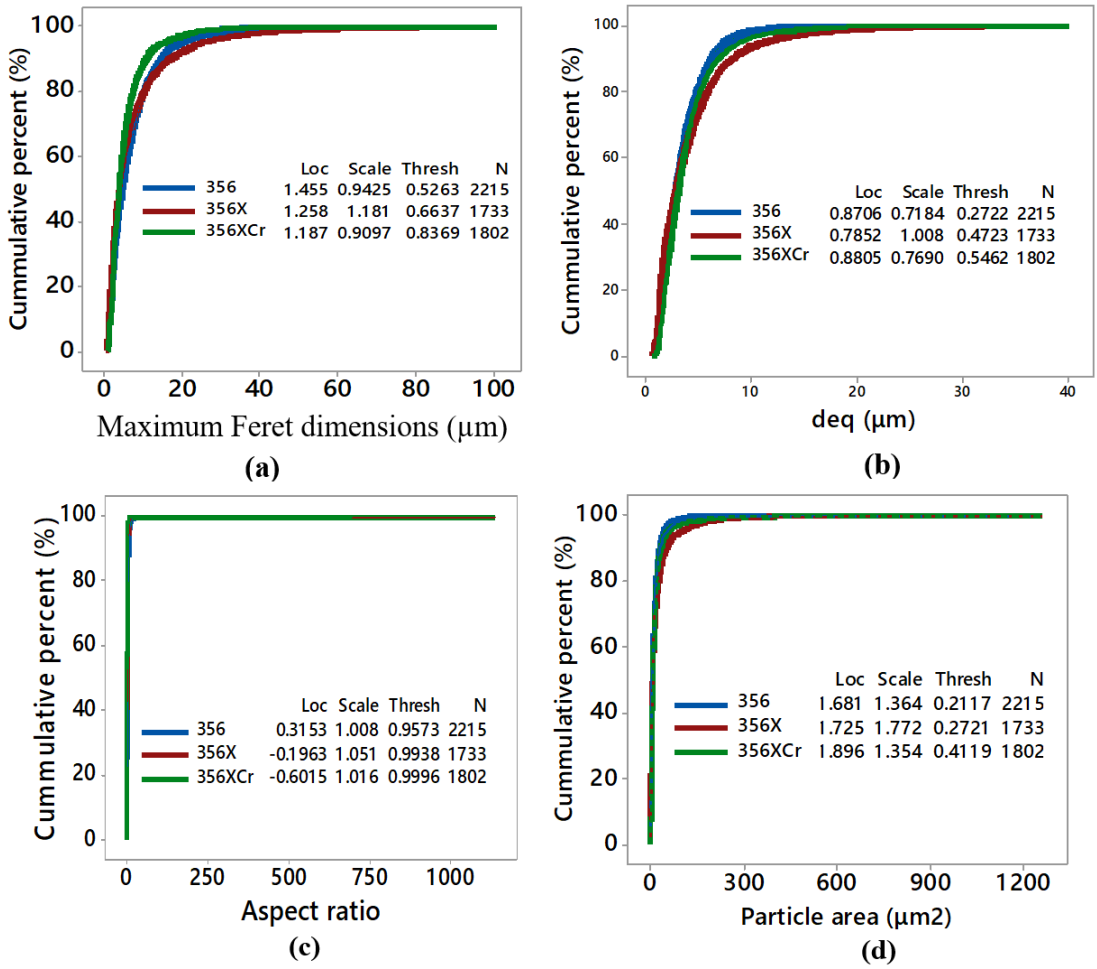

Figure 4.18: Cumulative distribution plots of: (a) Maximum Feret dimensions; (b) equivalent particle diameters; (c) aspect ratio values; (d) particle areas

Cumulative distribution plots were made to show the behavior of some shape aspects as a percentage of the entire particle population. They showed that most of the particle population, for all the three alloys, tended to be oriented towards minimum values of the following shape aspects: d_{eq}, maximum Feret dimensions, AR values, and particle areas. Fig. 4.18 shows that particles at the tail end (100%) of the distribution, for the maximum values, are less in number compared to those located at lower values. The particles of the three alloys are characterized by close AR values at any instant, as seen in Fig. 4.18 (c). This can be attributed to HIPing which tends to minimize porosities thus making AR values, which do not take into consideration features like pores, to be fairly uniform. Solution heat treatment also plays a role in the resultant uniform morphologies that cause the particles to have a close values of AR throughout.

(iii) Scatter plots

Scatter plots were made for various shape characteristics for the entire particle population of each alloy. These plots were necessary for determination of the relationship between various particle characteristics. These relationships are important in the discussion of the effect of microstructure particle-properties to mechanical performance. The scatter plots presented included: circularity vs. Maximum Feret dimension, circularity vs. Particle area, AR vs. Maximum Feret dimension, AR vs. Particle area, circularity vs. AR, and maximum Feret dimension vs. Equivalent particle diameter (d_{eq}).

(a) Circularity vs. Maximum Feret dimension/or area: Circularity has a strong correlation with the Maximum Feret dimension as seen in Fig. 4.19. Circularity tends to drop in a convex manner from 1.0 to approximately 0.3 (to a minimum value of the maximum Feret dimension of between 20-40 μm) after which it drops gradually to a minimum value of ~0 at the maximum Feret dimension. Therefore, this data can be modeled with a convex asymptote regression line as seen in the best lines of fit of the graphs in Fig. 4.19 (show a similar trend for all the three alloys). Similar observations are made for a relationship between Circularity vs. Particle area just that for this case, circularity drops sharply from 1.0 to ~0.1 when particle area is increased slightly with further increase in particle area simultaneously dropping circularity gradually (Fig. 4.20).

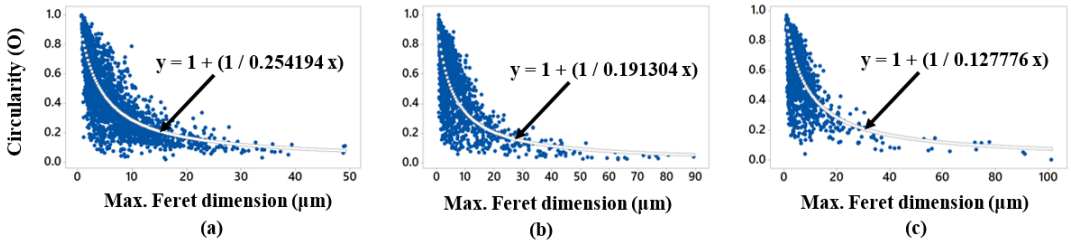

Figure 4.19: Circularity vs. maximum Feret dimensions for alloys: (a) 356; (b) 356X; (c) 356XCr; (d) 356X – showing circularity and maximum Feret dimensions having been modeled using a convex asymptote regression line

Also, as anticipated, a near perfect circular shape is achieved for the smallest particle sizes or areas with the circularity dropping as the particle size or area increases. This is generally because particles tend to assume greater irregularity in shape with increase in size or area. Particles' sizes and areas are also heavily oriented towards small sizes. Mbuya (2011) attributed this to fragmentation of Si particles due to high HIPing and solution heat treatment temperatures.

(b) Circularity vs. AR: Generally, a circularity approaching unity is achieved for

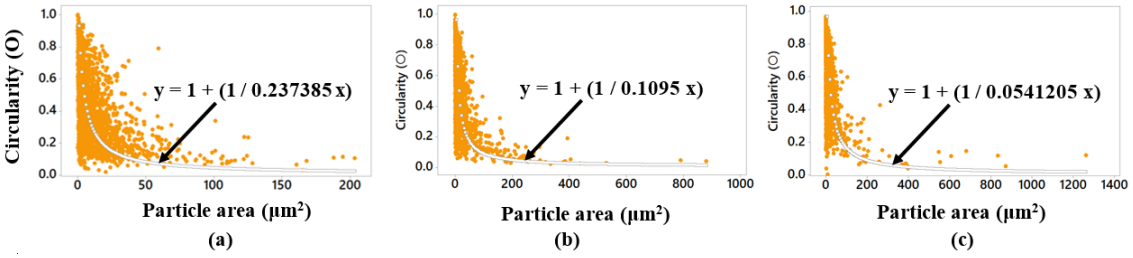

Figure 4.20: Circularity vs. particle area

particles with small values of AR and vice versa. More specifically, majority of the perfectly circular particles have a small aspect ratio of approximately 1 - 2 while the near perfect circular ones have AR values of 2 - 2.5 (Fig. 4.21).

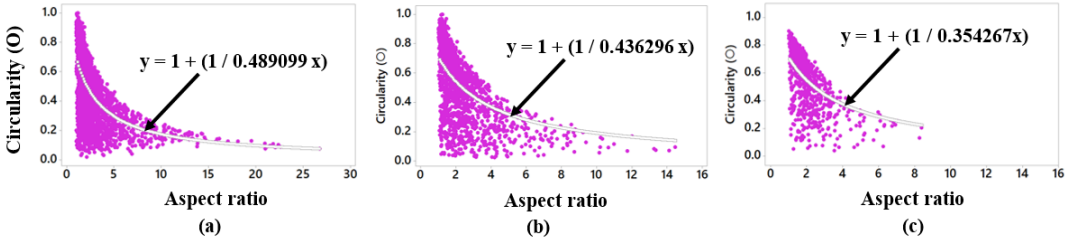

Figure 4.21: Circularity vs. AR for alloys: 356; 356X; 356XCr

(c) Maximum Feret dimension vs. Equivalent particle diameter: Contrary to expectations, the relationship between the maximum Feret dimensions and equivalent particle diameter is not perfectly linear i.e. scatter plots of the two aspects do not overlap but scatter about their linear relationship's plot (Fig. 4.24).

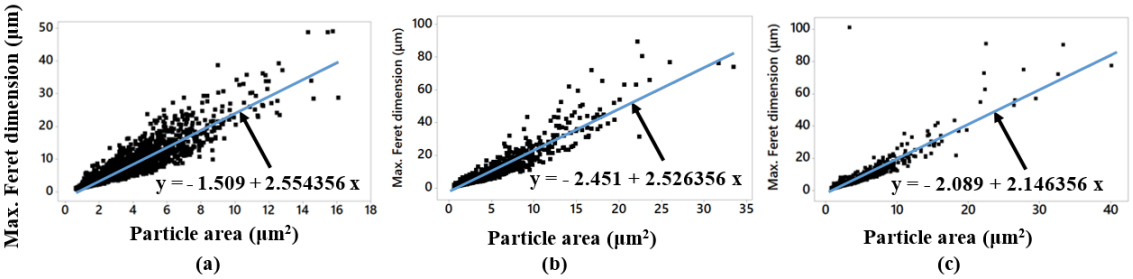

Figure 4.22: Maximum Feret dimensions vs. d_{eq}

(d) AR vs. Maximum Feret dimension/or area: There seems to be no perfectly describable trend observed between AR and maximum Feret dimension/or area. For instance, from Figs. 4.22 and 4.23, it can be seen that both small and large sized particles possess high and low values of aspect ratios in no defined manner. The AR values also generally ranged from ∼27 - 1 for the three alloys with the highest value of aspect ratio noted in alloy 356.

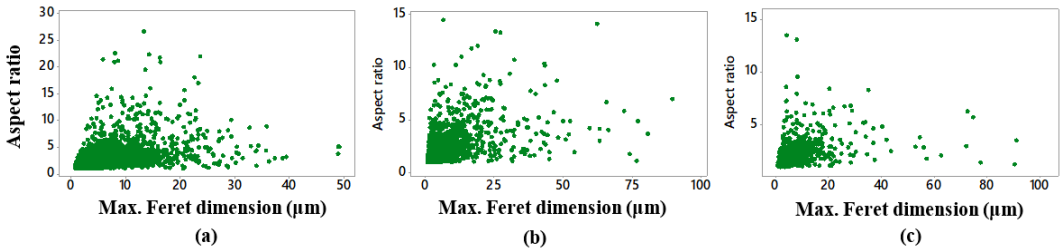

Figure 4.23: AR vs. maximum Feret dimensions

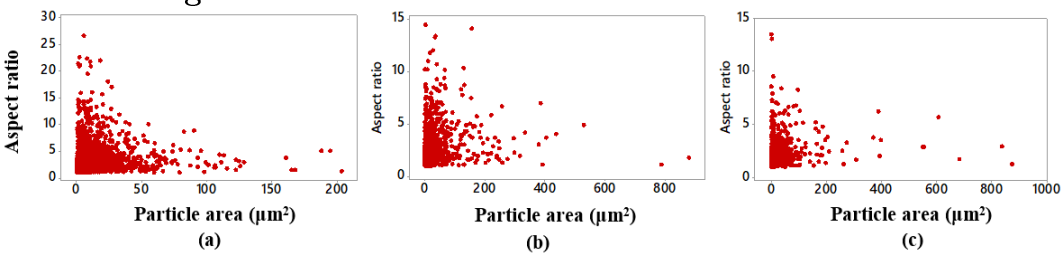

Figure 4.24: AR vs. particle area

4.2 Thermal analysis

4.2.1 Calculation of cooling rate

The cooling rate (CR) was obtained using equation (4.4) - (Farahany et al., 2012; Djurdjevic et al., 2001). The CR of Al-Si melt in the graphite crucibles was ~0.87 ^{o}C s^{-1} for all alloys (see Table 4.1).

Table 4.1: Cooling rate calculations for alloys subjected to TA

Alloy	T_p (^{o}C)	T_l (^{o}C)	$\lvert t_p - t_l \rvert$ (s)	CR (^{o}C)/s)
356	721.2	622.9	113.3	$\frac{721.2-622.9(^0C)}{113.3(s)} = 0.8676$
356X	634.1	603.6	35.5	$\frac{634.1-603.6(^0C)}{35.5(s)} = 0.8591$
356XCr	686.0	628.8	66.7	$\frac{686.0-628.8(^0C)}{66.7(s)} = 0.8576$
356X0.5CuCr	709.0	626.0	95.5	$\frac{709.0-626.0(^0C)}{95.5(s)} = 0.8691$
356X3.5CuCr	702.9	624.7	89.5	$\frac{702.9-624.7(^0C)}{89.5(s)} = 0.8740$
356TiSr	634.1	618.2	18.2	$\frac{634.1-618.2(^0C)}{18.2(s)} = 0.8750$

Note that, cooling rate was calculated as follows:

$$CR = \frac{T_p - T_l(^oC)}{|t_p - t_l|(s)} \tag{4.4}$$

Where: T_p and T_l are the pouring and liquidus temperatures respectively

t_p and t_l are the time recorded at pouring and beginning of nucleation

4.2.2 Solidification characteristic temperatures

Temperature and time data was used to calculate the $\triangle$T (°C) and $\frac{dT}{dt}$ (°C/s). Combined plots of T vs. t, $\triangle$T vs. t and $\frac{dT}{dt}$ vs. t for the alloys tested (Figs. 4.25 to 4.32) were interpreted to give the solidification temperatures.

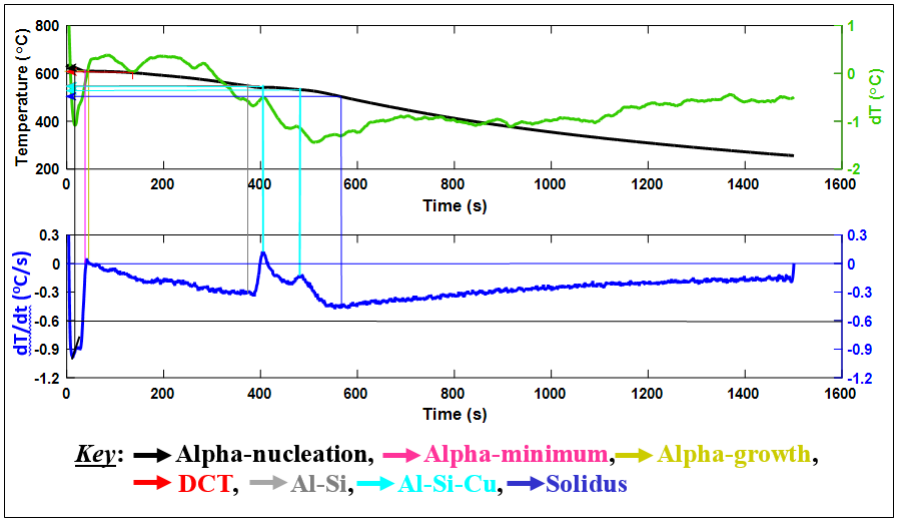

Figure 4.25: Phases' nucleation temperatures of alloy 356

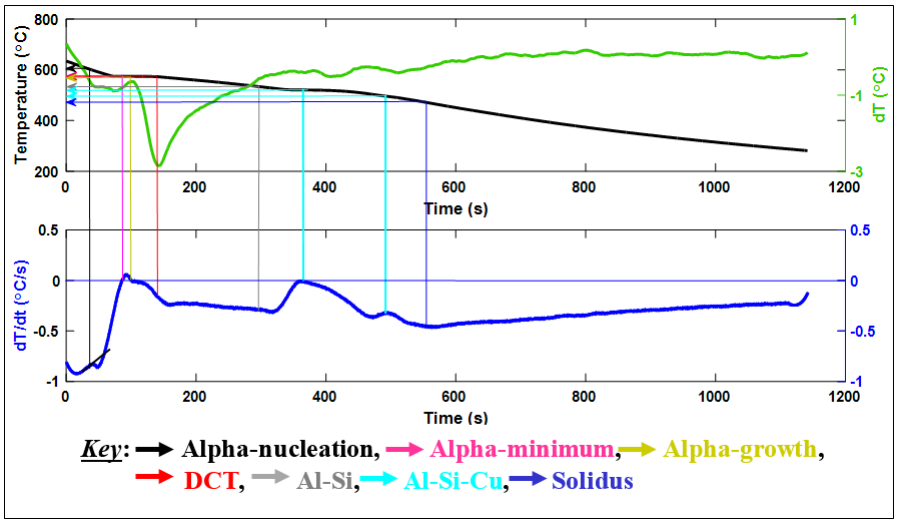

Figure 4.26: Phases' nucleation temperatures of alloy 356X

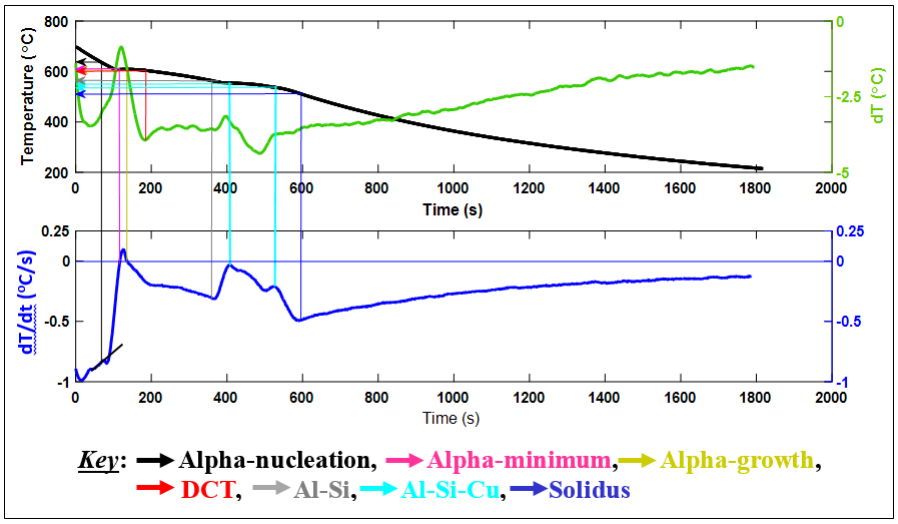

Figure 4.27: Phases' nucleation temperatures of alloy 356XCr

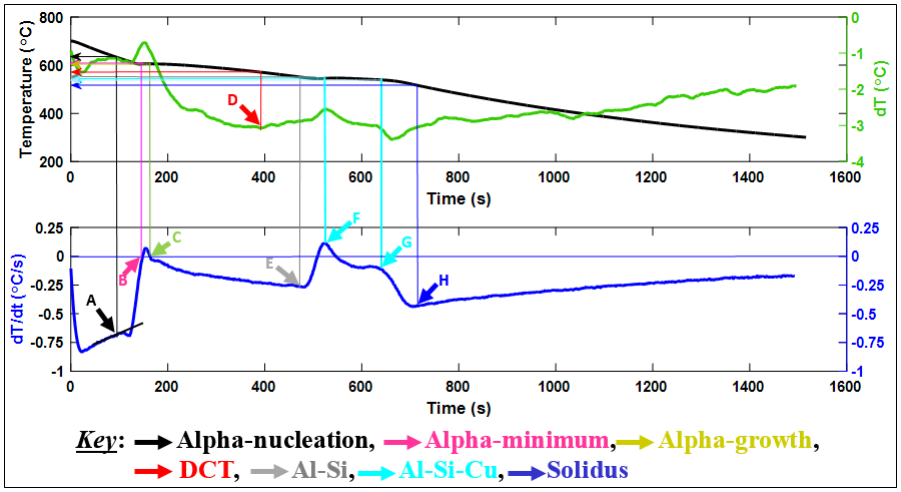

Figure 4.28: Phases' nucleation temperatures of alloy 356X0.5CuCr

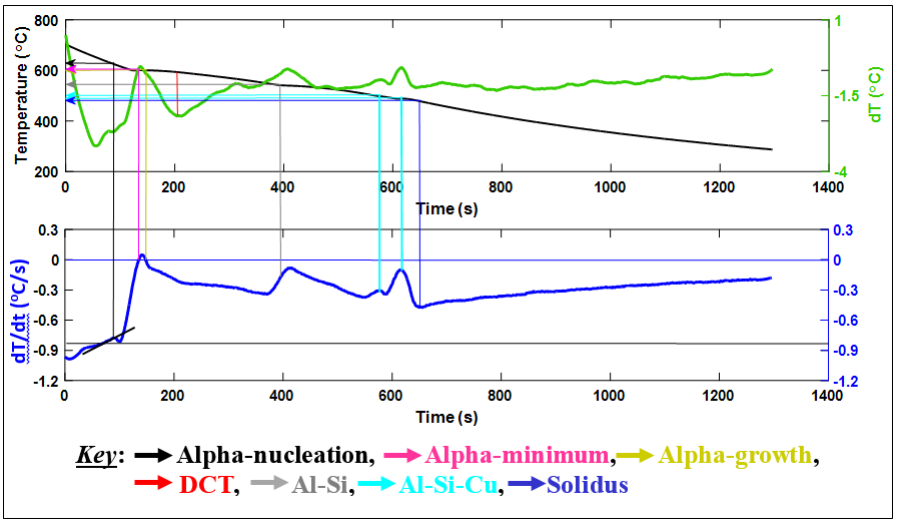

Figure 4.29: Phases' nucleation temperatures of alloy 356X3.5CuCr

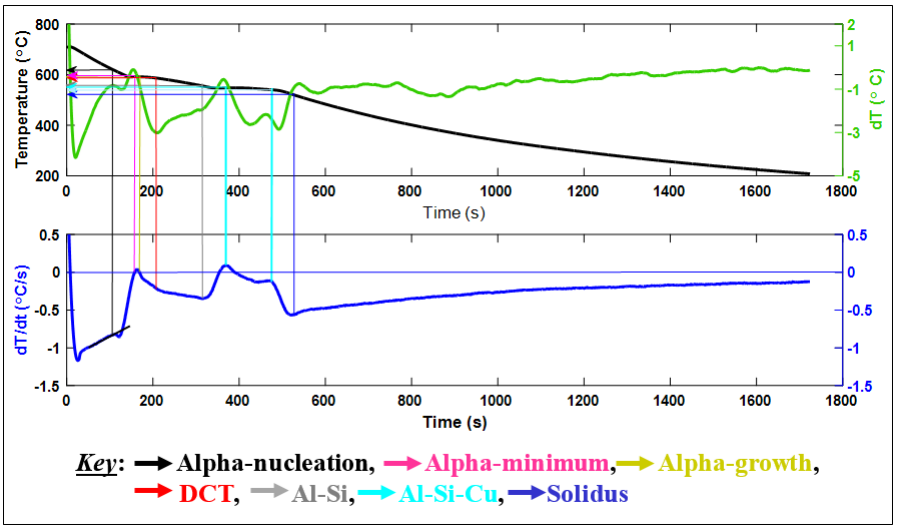

Figure 4.30: Phases' nucleation temperatures of alloy 356TiSr

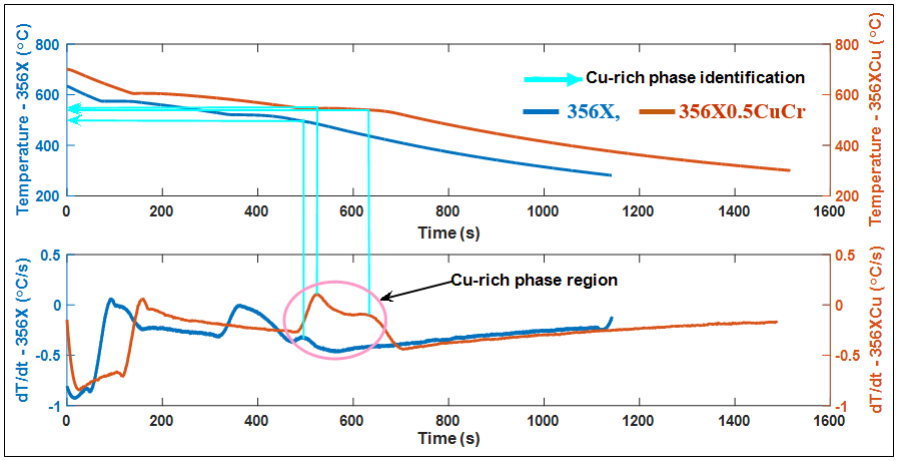

Figure 4.31: Impact of 0.5wt.% Cu + 0.15wt.% Cr on alloy 356X's phases nucleation temperatures

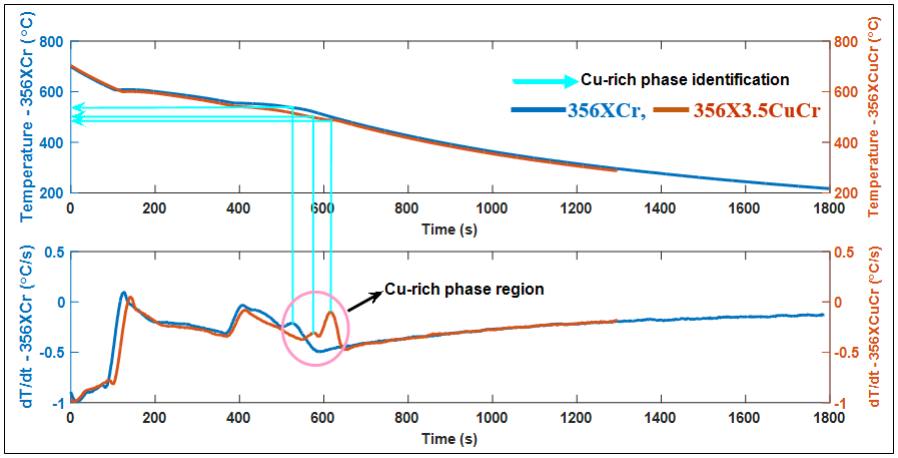

Figure 4.32: Impact of 3.5wt.% Cu on alloy 356XCr phases nucleation temperatures

Table 4.2 shows the tabulated temperatures at which nucleation of the various

phases occurred in the respective alloys.

Table 4.2: Solidification characteristic temperatures of the investigated alloys

Solidification phase	Phases' solidification temperatures (°C)					
	356	356X	356XCr	356X0.5CuCr	356X3.5CuCr	356TiSr
Alpha-nucleation	622.9	603.6	628.8	625.9	624.7	618.2
Alpha-minimum	603.5	579.4	605.3	604.7	603.6	601.2
Alpha-growth	599.8	575.9	598.3	597.1	600.6	595.9
DCT	593.5	578.1	589.5	584.2	593.0	591.2
Al-Si	547.1	534.7	557.7	547.7	550.0	552.5
Al-Si-Cu	513.5	501.0	537.1	536.2	517.7	538.3
				530.6	511.8	526.5
Solidus	482.6	474.1	508.8	510.0	496.5	510.0

In this research, thermodynamically strong metallurgical reactions that were noticeable on the T vs. t, $\triangle$T vs. t, and $\frac{dT}{dt}$ vs. t plots included: α-Al (nucleation, minimum, and growth temperatures), DCT, Al-Si eutectic, Al-Si-Cu eutectic, and solidus temperatures. These were mostly identified using the criteria mentioned in Section 2.3.2. The reactions that registered weak signals, such as the Fe-phases and Mg-phases, were not identifiable. However, this did not impact this research since Fe and Mg were not the major elemental additions of focus. In cases when an important reaction could not be identified directly on the cooling curve, it was traced from any other curve then it was projected to the cooling curve and the corresponding temperature and time obtained (Djurdjevic, 2012; Djurdjevic, 2013). The temperature readings were done by drawing lines from the points of interest to the cooling curve, with each color signifying a given phase's solidification. For instance, taking a look at the curves in Figs. 4.25 to 4.32, the key shows that color red was used to show how DCT was identified (from a given point of interest of a curve to the cooling curve and finally to the corresponding temperature). Similar readings shown in the keys were read off using the lines drawn using the colors indicated in the key. Appendix 6 shows an example of how these temperatures were read off for alloy 356TiSr. The differences in shape of the various curves plotted can be noted by the differences in temperatures brought about by the various elemental additives. Appendix 7 shows the solidification temperatures of the various alloys and the differences in temperature between these alloys and alloy 356. These temperature differences of the various phase nucleation temperatures are discussed hereafter to bring out the variation in the patterns of the curves of the various alloys.

The beginning of solidification was marked by solidification of the α-Al phase. The general α-Al temperatures ranged from 628.8 to 575.9 °C for all the six alloys. These temperatures signified the beginning of solidification of phases and are important in specifying the temperature at which pouring should be conducted to avoid premature solidification during casting.

Combined addition of 0.5Cu+0.15Cr+X or 3.5Cu+0.15Cr+X added to alloy 356 led to an increase in α-Al (nucleation and minimum) temperatures, Al-Si, Al-Si-Cu, and solidus temperature. A decrease was only registered in DCT. On the other hand, addition of 3.5Cu to 356+X+0.15Cr led to a decrease in all the solidification temperatures except α-growth and DCT which were increased. This was unlike the addition of 0.5Cu to 356+X+0.15Cr which led to a decrease in all the solidification temperatures. Addition of Cu to Al-Si alloys has been associated with a decrease in solidification characteristic temperatures (α-Al, DCT, Al-Si, and Al-Si-Cu) which contradicts these results, especially for high Cu additions. This can be attributed to the effects of other alloying elements used apart from Cu such as Cr which led to an increase in all solidification temperatures relative to alloy 356 (except for α-Al dendrite growth and DCT).

The general DCT values ranged from 593.5 to 578.1 °C for all the six alloys. This temperature range was high because as the solutes increased, the DCT decreased. More specifically, alloy 356 has the highest DCT at 593.5 °C with all its variants exhibiting lower values. When X+3.5Cu+0.15Cr, 0.15Ti+0.015Sr, X+0.15Cr, X+0.5Cu+0.15Cr, and X, were added to alloy 356, the DCT dropped by 0.5 °C, 2.3 °C, 4.0 °C, 9.3 °C, and 15.4 °C respectively. Thus, the highest temperature drop was observed when X was added exclusively to the base alloy 356 and the lowest temperature drop was observed when X+3.5Cu+0.15Cr was added to alloy 356. The decrease was attributed to increase in space between the α-Al dendrite arms to accommodate the increasing solute levels thus lowering the coherency temperature as postulated by other researchers (Backerud et al., 1990; Djurdjevic et al., 2012). Cu addition also contributed to lower DCT. However, in the presence of equal amounts of Cr, this decrease seemed to be more with decrease in Cu content such that the decrease was higher in alloy 356+X+0.5Cu+0.15Cr (9.3 °C) than it was in alloy 356+X+3.5Cu+0.15Cr (0.5 °C). Cr in the presence of combined addition of 0.15%Ti + 0.15%Zr + 0.25%V + 0.015%Sr also led to a lower temperature decrease than sole combined addition of X. More specifically, there was a decrease of 15.4 °C and 4 °C when X and XCr were added to alloy 356

respectively. Further, as much as TiSr addition to 356 reduced the DCT, X which has an additional 0.15%Zr + 0.25%V, lowered it further. This meant that as much as combined addition of X lowers DCT, the effect of adding TiSr contributes less to this temperature decrease than addition of 0.15%Zr + 0.25%V.

The general Al-Si nucleation temperatures for the studied set of alloys ranged from 534.7 to 557.7 °C for all the six alloys. The nucleation of Fe-rich and Mg-related phases was not noticed in this research due to weak signals and the presence of minor Fe quantities in the investigated alloys. The rigidity temperature was also not a focus of this research and therefore it was not identified. It can be noted that addition of X to alloy 356 led to a decrease in Al-Si eutectic solidification temperature by 12.4 °C but a further addition of 0.15Cr, 0.5Cu+0.15Cr, and 3.5Cu+0.15Cr led to an increase of 10.6, 0.6, 2.9, and 5.4 °C respectively. An increase of 5.4 °C was also noted when TiSr was added to alloy 356. Thus, addition of 0.15%Zr + 0.25%V seems to be what led to the decrease.

In this research, at least one Cu-rich phase peak was identified for each alloy. For alloy 356, 356X, and 356XCr, only one peak was identified for each at 513.5, 501.0, and 537.1 °C respectively. For alloys 356X0.5CuCr, 356X3.5CuCr, and 356TiSr, two peaks were identified for each at 536.2 and 530.6, 517.7, and 511.8 and at 538.3 and 526.5 °C respectively. The inability to identify the third and in some cases the second peak can be associated with weak latent signals during Cu-rich phases' precipitation in 356 alloys and the low Cu content in alloys 356, 356X, and 356XCr. The inability to identify some peaks for the nucleation of the Cu-rich phase does not pose as a limitation in this research because the peaks identified rely heavily on the Cu content. For instance, for alloys 356X and 356XCr, only one Cu-rich peak is identified while two peaks are noted for alloys 356X0.5CuCr and 356X3.5CuCr (see Figs. 4.31 and 4.32). In addition, the results obtained were sufficient to inform solution heat treatment temperatures. More specifically, basing on the Cu-rich solidification temperatures, the maximum recommended solution heat treatment temperatures which the tested alloys can be subjected to while minimizing incipient melting is 500 °C.

The solidus temperatures were identified so that they could inform the temperatures at which the various alloys would no longer be in molten state, a concept that is very crucial in foundry practice. General solidus temperatures ranged from 474.1 to 510.0 °C for all the six alloys. This temperature decreased with

addition of X but increased with all other additions i.e. XCr, TiSr, X0.5CuCr, and X3.5CuCr. The decrease can be associated with the lowered temperature for α-Al and Al-Si solidification temperatures for alloy 356X relative to alloy 356 thus increasing the solidification time and consequently lowering the temperature for the last drop to solidify. Addition of TiSr addition to 356 increased the solidus temperature while X which has an additional 0.15%Zr + 0.25%V lowered it. This means that as much as addition of X decreases solidus temperature, adding TiSr or ZrV leads to a temperature increase implying that sole addition of 0.15%Zr + 0.25%V may lead to a decrease.

Sr addition to alloy 356 (in the presence of 0.15%Ti + 0.15%Zr + 0.25%V) recorded a decrease in all solidification temperatures as shown in Table 4.2. For instance, relative to alloy 356, α-Al nucleation, α-Al minimum, α-Al growth, DCT, Al-Si, Al-Si-Cu, and solidus temperatures of alloy 356X reduced by 19.3, 24.1, 23.9, 15.4, 12.4, 12.5, and 8.5 °C respectively. Comparing the effects of X and TiSr, the later seems to increase Al-Si and solidus temperatures while Zr and V seems to decrease them. However, they all seem to lower α-Al nucleation and DCT temperatures with the decrease being more for X than for TiSr.

4.3 Tensile tests

From tensile tests, the actual mechanical test results (UTS, YS, and percentage elongation) and fractography results are presented and discussed. Table 4.3 shows the tabulated tensile test results calculated from the load-extension data and specimen dimensions.

In Table 4.3, a comparison of the tensile performance of the alloys under investigation was made whereby three specimens of a particular alloy were tested at 25 °C and 237 °C giving three differing results for each tensile property. This explains the three specimen test numbers. However, the discussion on tensile results are based on the average values. Since there is no distinct YS in these results, the value given is that of 0.2% proof stress. Fig. 4.33 shows the stress-strain plots obtained from tensile test results of alloys 356, 356X, and 356XCr at 25 °C and 237 °C. On the other hand, Fig. 4.34 shows plots of average values of UTS, YS, and El (%) for the investigated alloys as extracted from Table 4.3.

Table 4.3: Tensile test results

Tensile property	Specimen No.	25 °C			237 °C		
		356	356X	356XCr	356	356X	356XCr
Ultimate Tensile Strength (UTS) - MPa	(i)	214	237	257	149	167	174
	(ii)	223	242	265	156	173	177
	(iii)	217	241	270	151	170	180
	Average	218	240	264	152	170	177
Yield Strength (YS) - MPa	(i)	204	214	237	122	142	157
	(ii)	209	217	245	120	142	167
	(iii)	207	214	248	126	144	162
	Average	207	215	243	123	143	162
% Elongation	(i)	3.4	3.4	4.4	8.0	4.7	6.2
	(ii)	5.0	4.2	4.0	7.0	6.3	6.5
	(iii)	3.7	3.8	4.3	7.5	5.0	5.6
	Average	4.0	3.8	4.2	7.5	5.3	6.1

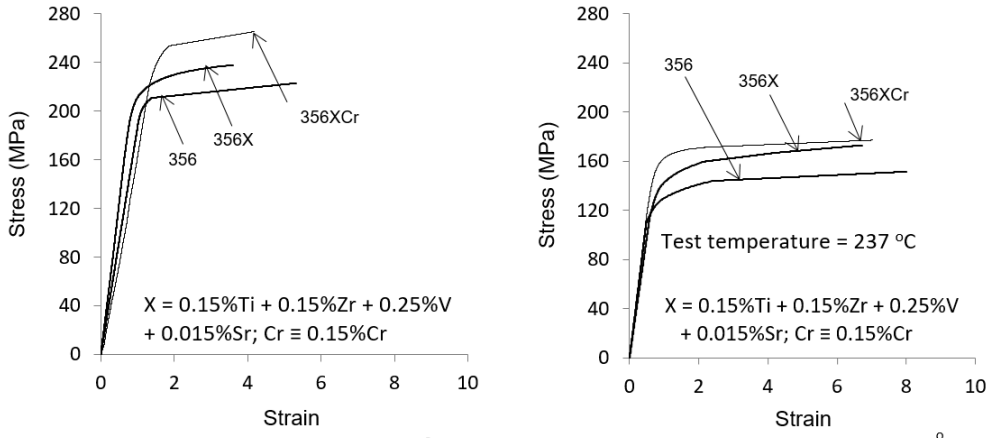

(a) Room temperature (25 °C) (b) High temperature (237 °C)

Figure 4.33: Stress-strain plots of alloys 356, 356X, and 356XCr (25 °C and 237 °C)

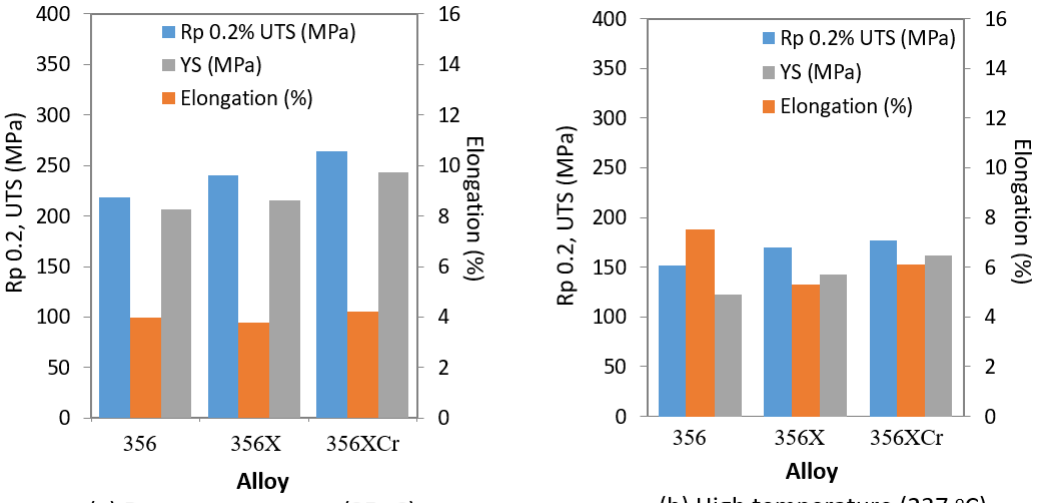

(a) Room temperature (25 °C) (b) High temperature (237 °C)

Figure 4.34: Plots of avg. UTS, YS, and El(%) for alloys 356, 356X, and 356XCr

4.3.1 Mechanical tensile tests

Generally, there is some scatter in the tensile test results due to the variability in the alloys such as differences in chemical composition and differences in solidification rate of samples obtained from different locations of the same thickness of the casting. However, this variability due to casting defects is not very pronounced since the porosity defects were minimized through HIPing.

From Fig. 4.34, it is seen that ductility increases with increase in temperature. The lowest ductility at room temperature is seen in alloy 356X (3.8%), the highest is exhibited by alloy 356XCr (4.2%) and the average of both is in alloy 356 (4.0%). For high temperature tensile tests, the lowest average elongation is seen in alloy 356X (5.3%), the highest in 356 (7.5%) and median value in alloy 356XCr (6.1%). Therefore, alloy 356X is the least ductile of the three tested alloys both at 25 and 237 °C. Alloy 356 is more ductile than alloy 356XCr at room temperature while the reverse is true at high temperature. It can therefore be said that these alloys are ductile and not brittle since their fracture strains are greater than 5%. Elongation decreased by 5.8% and 28.9% at room and elevated temperatures respectively when there was combined addition of 0.15%Ti, 0.15%Zr, 0.25%V, and 0.015%Sr to alloy 356. However, an additional 0.15Cr led to an increase of 5% at room temperature and a decrease of 18.7% at elevated temperatures. The low ductility for alloy 356X at room temperature is associated with the effect of adding 0.15%Ti, 0.15%Zr, 0.25%V, and 0.015%Sr as much as the transition elements have a low solubility and diffusivity in aluminium. The alloy containing Cr in addition to 0.15%Ti, 0.15%Zr, 0.25%V, and 0.015%Sr has a fairly high ductility because Cr is known to modify β-Al_5FeSi platelet inclusions to α-$Al_{13}(Fe,Cr)_4Si_4$ fish-bone like phase and it also decreases and increases the volume fraction of β and α-phases respectively (Yang et al., 2015).

Referring to Figs. 4.33 and 4.34 and Table 4.3, the strength of the alloys is generally higher at 25 °C than at 237 °C. This is because at high temperature there is an increase in thermal vibrations which promote movement of dislocations. Coarsening or dissolution of strengthening precipitates also plays a major role. The strongest alloy is 356XCr followed by 356X and the weakest is alloy 356 in order of decreasing magnitude of their YS and UTS both at room and high temperature. Simultaneous addition of Cr and X to alloy 356 led to an increase in UTS (21.1% at 25 °C and 16.4% at 237 °C) and YS (17.7% at 25 °C and

32.1% at 237 °C). Also, combined addition of 0.15%Ti, 0.15%Zr, 0.25%V, and 0.015%Sr to alloy 356 led to an increase in UTS (10.1% at 25 °C and 11.8% at 237 °C) and YS (4.0% at 25 °C and 16.3% at 237 °C). This can be associated with modification whereby alloy 356X and 356XCr were modified. Therefore, they contained rounded eutectic Si particles which have a low susceptibility to cracking unlike large coarse Si particles that characterized the unmodified alloy 356. These alloys are also grain refined and this results to uniform distribution of fine second phases which increases strength. The explanation behind the average UTS and YS being highest in alloy 356XCr followed by 356X and least in alloy 356 can also be explained by increase in solutes. This increase, brought about by alloying, increases strength of the soft α-Al matrix by hardening it through point defects, e.g., as substituted atoms and vacancies or by precipitation hardening with dispersion particles of the second phase (Sjolander & Seifeddine, 2010; Zamani, 2015). Therefore, the matrix was a key determinant of the alloy strength (Zamani, 2015). Additionally, the SDAS for alloy 356XCr is smaller than that for 356X, as much as the difference is not very significant, but as SDAS becomes smaller, there is a finer and more even dispersion of second phase particles. This enhances mechanical strength. Sr addition, in the company of other transition elements such as Cr, Ti, V, and Zr also led to a decrease in elongation for all the alloys except alloy 356XCr at room temperature.

4.3.2 Fractography

The fracture surfaces of the tensioned to failure alloy specimens are as shown in Fig. 4.35 for the three alloys that were tested. Overall, fracture occurred in a brittle-ductile manner whereby the solid solution α-matrix was dominated by ductile fracture with finely dimpled morphology and plastically transformed walls and brittle fracture of brittle intermetallic particles. Cleavage features resulting from transcrystalline brittle fracture were also scarcely evident. Fracture regions were generally characterized by a seldom occurrence of fatigue striations and flat surfaces with tear ridges characterizing most fractographs in the representative areas of focus of the micrographs. Cracked and debonded particles were also identified but casting defects were not identified in the specimen used.

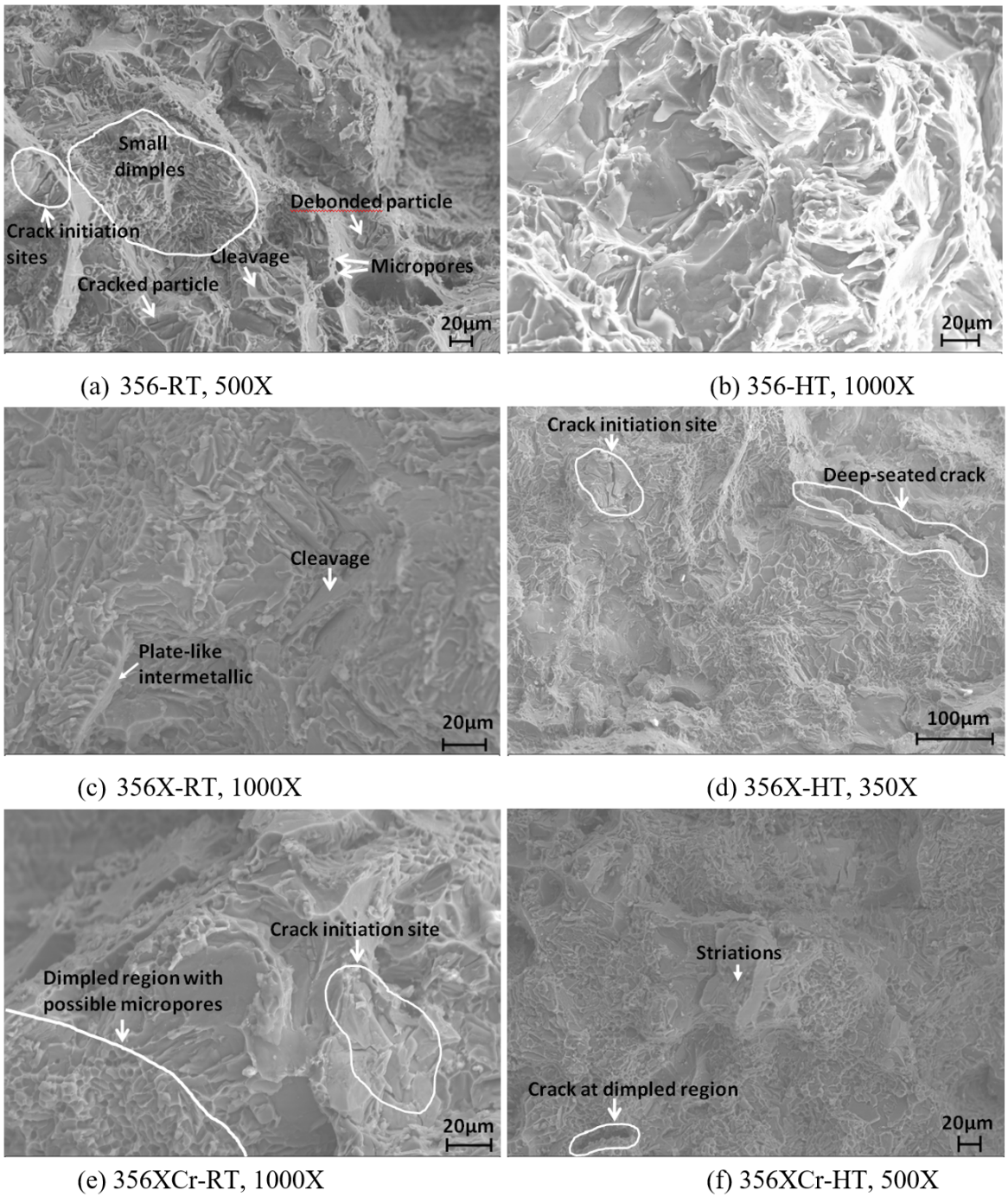

Figure 4.35: Fractographs of the tensioned to failure alloy specimens at room temperature and high temperature

A comparison of the high and low temperature tensile specimen fractographs showed that brittle fracture dominated the room temperature tested fracture surfaces, especially at intermetallics, with limited regions experiencing plastic deformation. At high temperature, there was a shift to a dominance of ductile fracture with dimple morphology (Fig. 4.35 (f)). Heat treatment following HIP

increased the volume fraction of nucleation sites (especially microscopic inhomogeneities) which promoted coalescence of microvoids as seen by other researchers (Tagirov et al., 2012; Mohamed et al., 2013). These microvoids grew, coalesced and ruptured at regions of high plastic deformation forming many depression microstructures on the fracture surfaces referred to as dimples. These dimples, assumed conical shapes and occurred in various sizes thereby dominating the fracture surfaces. The morphology and size of the dimples on the fracture surfaces are said to trace the morphology of eutectic silicon particles located beneath them (Tillova et al., 2012; Tagirov et al., 2012), which were spheroidized in this case due to heat treatment. The fracture path was also characterized by deep seated cracks (macro-cracks) that seemed to have initiated and propagated at dimpled and cracked particle regions or where microvoids or dimples were enjoined (Fig. 4.35 (d)). This is because micropores may act as areas of weakness along which cracks easily initiate and propagate especially when the Si particles beneath them are brittle. This increases susceptibility to cracking.

4.4 Fatigue tests

Fatigue test results for the three alloys are tabulated in Table 4.4 and graphically represented in Fig. 4.36.

Table 4.4: Fatigue test results tabulated for the three alloys investigated showing the stress applied to a failure or runout outcome and the numbers of cycles of each single test for each of the alloy's eight specimen tests

	356			356X			356XCr		
Specimen Test No.	Stress applied (MPa)	Status	Cycles x10^6	Stress applied (MPa)	Status	Cycles x10^6	Stress applied (MPa)	Status	Cycles x10^6
1	76	Failure	2.62	75	Runout	10.0000	74	Runout	10.00
2	67	Failure	8.69	84	Failure	4.6030	83	Runout	10.00
3	58	Runout	10.00	75	Failure	7.87	92	Failure	2.80
4	67	Runout	10.09	66	Failure	1.03	83	Failure	8.25
5	76	Failure	6.60	57	Runout	10.10	74	Runout	10.00
6	67	Runout	10.00	66	Failure	6.19	83	Failure	9.00
7	76	Runout	10.35	57	Runout	10.09	74	Runout	10.00
8	85	Failure	6.36	66	Runout	10.00	83	Runout	10.00
Fatigue strength	71.4 MPa			68.3 MPa			81.5 MPa		
Standard deviation	7.7 MPa			10.5 MPa			5.0 MPa		

The standard deviation values of alloys 356, 356X, and 356XCr were 7.7, 10.5, and 5.0 MPa respectively. A step size of 9 MPa was used in this research with the

calculated values of standard deviation obtained for alloy 356 having the smallest deviation from the actual applied step size. However, all the values of standard deviation obtained lied within 50% of the true standard deviation, as suggested by Pollak (2005), making this choice of step size adequate. Thus, stress results were distributed around the mean as intentioned by the staircase method.

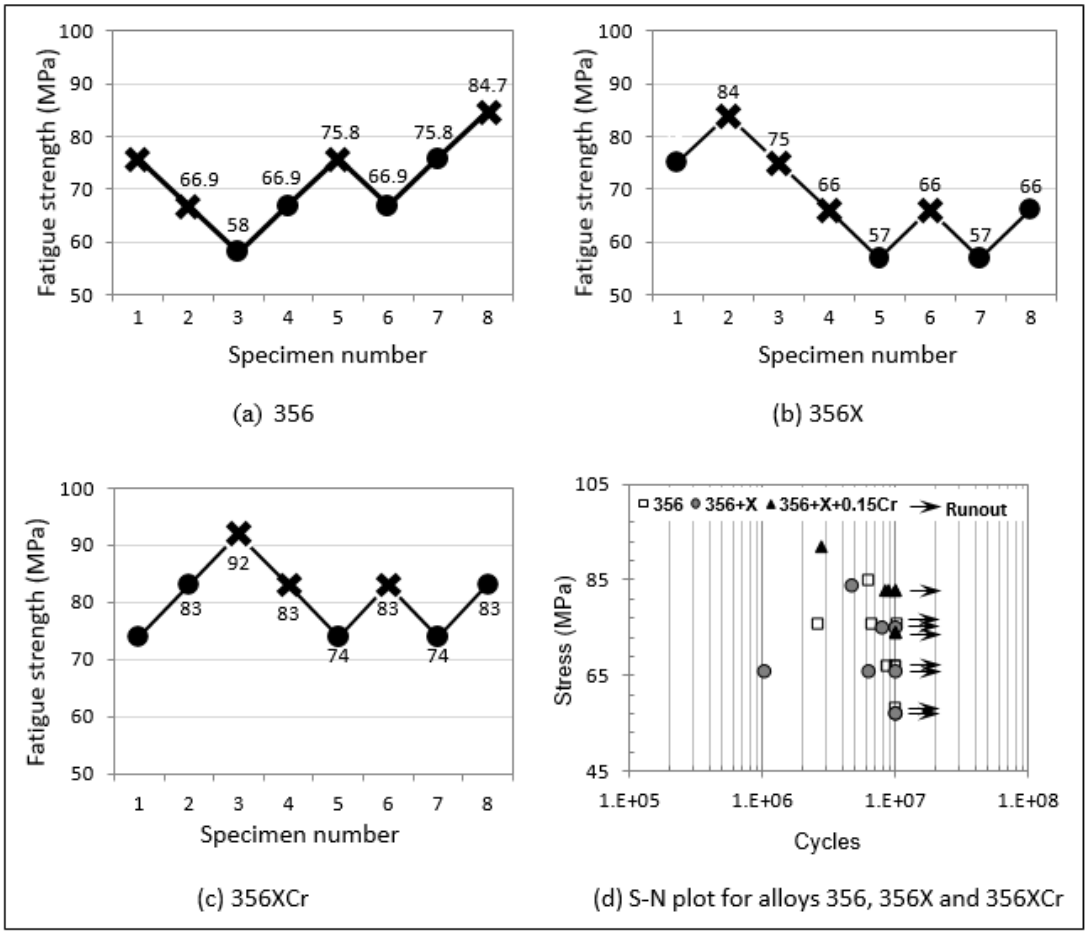

Figure 4.36: Graphical representation of the results obtained using the staircase method in fatigue strength determination tests (a) 356; (b) 356X; (c) 356XCr; (d) S-N plot of the three alloys investigated

The fatigue strengths of alloys 356, 356X, and 356XCr were 71.4, 68.3, and 81.5 MPa respectively. These values were above the normal 65 MPa common for 356 alloys (Tagirov et al., 2012; Tajiri et al., 2014). This high fatigue strength ($>$ 65 MPa) was attributed to HIPing that eliminated porosities and T6 heat treatment that reduced aspect ratio of Si particles thus making them less prone to cracking. Also, from microscopy results it was shown that the particle sizes and areas are heavily oriented towards small sizes and this undoubtedly plays a role in the high

fatigue strength since it reduces the probability of particle damage during loading. Clearly, the highest fatigue strength was obtained for alloy 356XCr followed by 356 and 356X had the least. Relative to alloy 356, combined addition of 0.15%Ti, 0.15%Zr, 0.25%V, and 0.015%Sr to alloy 356 thus decreased the fatigue limit by 3.1 MPa whereas a further addition of 0.15%Cr increased the fatigue limit by 10.1 MPa at room temperature. The increase is due to Cr addition which leads to formation of strengthening precipitates in the aluminium matrix. The unmodified base alloy was characterized by a higher fatigue strength than the modified alloy 356X. This is contrary to the individual addition effects of Ti, Zr, and V to 356 alloys which have been associated with increase in fatigue strength. This may be due to their combined effect which may lead to poor fatigue performance especially due to formation of related intermetallics. The fatigue strength for alloy 356XCr is also higher than that for 356X because it possesses a lower SDAS, as explained for tensile strength.

CHAPTER FIVE

CONCLUSIONS AND RECOMMENDATIONS

5.1 Conclusions

This research demonstrated the effect of combined addition of Ti, Zr, V, Cr and Cu on microstructure, mechanical performance and solidification properties of model secondary 356 alloys and the following key conclusions were made:

1. Presence of (AlSi)x(TiZr)Fe improved both fatigue and tensile properties.
2. High fatigue strength (>65 MPa) was also as a result of hipping, heat treatment, grain refinement, modification and alloying using strength forming precipitates such as Cr-related ones in α-Al matrix.
3. Generally, addition of XCr to 356 improved tensile and fatigue performance of 356 alloys than addition of TiSr or sole X .
4. Addition of X to alloy 356 is unfavourable for cases where high ductility is a prerequisite and XCr is not very ideal for high temp. elongation applications.
5. X and XCr additions are ideal for high strength applications both at room temperature and at 237 °C.
6. There is a likelihood of addition of Sr as a constituent of X decreasing elongation at room temperature.
7. Max. Feret dimension and deq do not have a perfectly linear relationship, AR and maximum Feret dimension/or area have no clear relationship but there is strong correlation between circularity and maximum Feret dimensions/or area.
8. X and ZrV decreased solidus temperatures while all other additions (XCr, TiSr, X0.5CuCr and X3.5CuCr) increased it.
9. X, ZrV and TiSr decreased α-Al nucleation temperature and DCT with the decrease by X being greatest followed by ZrV and finally TiSr.
10. Added X+Cu+Cr decreased DCT (higher decrease registered at lower Cu contents) while XCr increased α-Al nucleation, Al-Si, and solidus temperatures.

5.2 Recommendations

Based on the conclusions made, the following studies can further this research.

1. A thermal analysis set-up kit incorporated with appropriate software and phase identification capabilities be designed and fabricated to facilitate easy conduction of thermal analysis tests especially when arresting phases by quenching.
2. Vary the amounts of Cr so as to identify optimal additions in these set of alloys for maximum fatigue and tensile strength at both high and low temperatures.
3. Conduct short crack fatigue tests to further understand alloy failure.
4. Effect of additives on HIPed and friction stir processed alloys be investigated.
5. Subject the alloys to other mechanical tests such as creep and wear.

REFERENCES

Dahle, A.K., Nogita, K., McDonald, S.D., Dinnis, C., & Lu, L. (2005). Eutectic Modification and Microstructure Development in Al-Si Alloys. Materials *Science and Engineering A*, 413-414, 243-248.

Apelian, D., Shivkumar, S., & Sigworth, G. (1989). Fundamental Aspects of Heat Treatment of Cast Al-Si-Mg Alloys. *AFS Transactions, 2*, 727-742.

Bäckerud, L., Chai, G., & Tamminen, J. (1990). Solidification Characteristics of Aluminum Alloys. *AFS/Skanaluminium, 2*, 71-84.

Baradarani, B., & Raiszadeh, R. (2011). Precipitation Hardening of Cast Zr-Containing A356 Aluminium Alloy. *Materials and Design, 32*(2), 935-940.

Barlow, J. O., & Stefanescu, D. M. (2002). Computer-Aided Cooling Curve Analysis Revisited. *AFS Transactions,* 349-354.

C.H.Caceres, M.B.Djurdjevic, T.J.Stockwell, & Sokolowski, J. (1999). The Effect of Cu Content on the Level of Microporosity in Al-Si-Cu-Mg Casting Alloys. *Scripta Materialia, 42*(5), 631-637.

Choi, S. W., Cho, H. S., & Kumai, S. (2016). Titanium as an Intermetallic Phase Stabilizer and its Effect on the Mechanical and Thermal Properties of Al-Si-Mg-Cu-Ti Alloy. M*aterials Science and Engineering A*, 678, 267-272.

Cruz, H., Gonzalez, C., Juárez, A., Herrera, M., & Juarez, J. (2006). Quantification of the Microconstituents Formed During Solidification by the Newton Thermal Analysis Method. *Journal of Materials Processing Technology, 178*(1-3), 128-134.

Cupido, L. H. (2014). *Experimental and Numerical Investigation of Heat Treatment of Al-Si-Cu Alloy.* (Msc. thesis). Cape Peninsula University of Technology. Cape Town. South Africa.

Davis, J. R. (1993). J. R. Davis and Associates (Eds.). *Aluminium and Aluminium Alloys (ASM speciality handbook).* ASM International.

Devore, J. L., & Farnum, N. R. (1999). *Applied Statistics for Engineers and Scientists.* Duxbury. USA.

Djurdjevic, M., Byczynski, G., Schechowiak, C., Stieler, H., & Pavlovic, J. (2009). Quantification of the Impact of Strontium on the Solidification Path of the Aluminum-Silicon-Copper Alloys Using Thermal Analysis Technique. *Practical Metallography, 46*(3), 137-152.

Djurdjevic, M., Huber, G., & Odanovic, Z. (2012). Synergy Between Thermal

Analysis and Simulation. *Journal of Thermal Analysis and Calorimetry, 90*.

Djurdjevic, M. B., Huber, G., & Odanovic, Z. (2012). Synergy Between Thermal Analysis and Simulation. *Journal of Thermal Analysis and Calorimetry, 111*(2), 1365-1373.

Djurdjevic, M. B., Kasprzak, W., Kierkus, C. A., Kierkus, W. T., & Sokolowski, J. H. (2001). Quantification of Cu Enriched Phases in Synthetic 3XX Aluminum Alloys Using the Thermal Analysis Technique. *American Foundry Society*, 1-12.

Djurdjevic, M. B., & Manasijevic, S. (2014). Impact of Major Alloying Elements on the Solodification Parameters of Cast Hypoeutectic AlSi6Cu (1-4 wt.%) and AlSi8Cu(14 wt.%) Alloys. *Metallurgical and Materials Engineering, 20*(4), 235-246.

Djurdjevic, M. B., Manasijevic, S., Odanovic, Z., Dolic, N., & Radisa, R. (2014). Quantification of the Copper Phase(s) in Al-5Si-(1-4)Cu Alloys Using a Cooling Curve Analysis. *Materiali in Tehnologije, 48*(2), 299-304.

Djurdjevic, M. B., Manasijevic, S., Odanovic, Z., & Radisa, R. (2013). Influence of Different Contents of Si and Cu on the Solidification Pathways of Cast Hypoeutectic Al-(5-9)Si-(1-4)Cu (wt.%) Alloys. *International Journal of Materials Research, 104*(9), 865-873.

Djurdjevic, M. B., Odanovic, Z., & Talijan, N. (2011). Characterization of the Solidification Path of AlSi5Cu(1-4 wt.%) Alloys Using Cooling Curve Analysis. *JOM, 63*(11), 51-57.

Djurdjevic, M. B., Sokolowski, J. H., & Odanovic, Z. (2012). Determination of Dendrite Coherency Point Characteristics Using First Derivative Curve Versus Temperature. *Journal of Thermal Analysis and Calorimetry, 109*(2), 875-882.

Dobrzanski, L., Maniara, R., & Sokolowski, J. H. (2006). The Effect of Cast Al-Si-Cu Alloy Solidification Rate on Alloy Thermal Characteristics. *Journal of Achievements in Materials and Manufacturing Engineering , 17*(1), 217-220.

Donovan, R., Fortune, R., & Trout, R. (2015). *Elevated Temperature Effects on the Mechanical Properties of Age Hardened 6xxx Series Aluminum Alloy Extrusions.* (Bachelors Technical Report).California State University, San Luis Obispo. Long Beach. USA.

Doty, H.W., Samuel, A.M., & Samuel, F.H. (1996). Factors Controlling the Type

and Morphology of Copper-Containing Phases in the 319 Aluminum Alloy. *100th AFS Casting Congress*. Philadelphia, Pennsylvania. USA.

Edwards, G., Stiller, K., Dunlop, G., & Couper, M. (1998). The Precipitation Sequence in Al-Mg-Si Alloys. *Acta Materialia, 46*, 3893-3904.

Elhadari, H. A., Patel, H. A., Chen, D. L., & Kasprzak, W. (2011). Tensile and Fatigue Properties of a Cast Aluminum Alloy with Ti, Zr and V Additions. *Materials Science and Engineering A, 528*(28), 8128-8138.

Farahany, S., Ourdjini, A., & Idris, M. H. (2012). The Usage of Computer-Aided Cooling Curve Thermal Analysis to Optimise Eutectic Refiner and Modifier in Al-Si Alloys. *Journal of Thermal Analysis and Calorimetry, 109*(1), 105-111.

Farahany, S., Ourdjini, A., Idrsi, M. H., & Shabestari, S. G. (2013). Evaluation of the Effect of Bi, Sb, Sr and Cooling Condition on Eutectic Phases in an Al-Si-Cu Alloy (ADC12) by In Situ Thermal Analysis. T*hermochimica Acta, 559*, 59-68.

Genualdi, A. (2001). *Metallurgical Aspects of Aluminum Lost Foam Automotive Castings*. SAE- Technical Publication.

Gustafsson, G., Thorvaldsson, T., & Dunlop, G. L. (1986). The Influence of Fe and Cr on the Microstructure of Cast Al-Si-Mg Alloys. *Metallurgical Transactions A, 17*(1), 45-52.

Hatch, J. (1984). *Aluminum: Properties and Physical metallurgy*. Metals Park, Ohio: ASM International.

Svensson, I.L., & Seifeddine, S. (2009). The Influence of Fe and Mn Content and Cooling Rate on the Microstructure and Mechanical Properties of A380-die Casting Alloys. *Metallurgical Science and Technology, 27*(1), 11-20.

Lee, J.A., & Chen, P. S. (2005). *High Strength Aluminum Alloy for High Temperature Applications*. US patent, No. US 6918970 b2.

Jana, S., Mishra, R., Baumann, J., & Grant, G. (2009). Effect of Stress Ratio on the Fatigue Behavior of a Friction Stir Processed Cast Al-Si-Mg alloy. *Scripta Materialia, 61*, 992-995.

Javidani, M., & Larouche, D. (2014). Application of Cast Al-Si Alloys in Internal Combustion Engine Components. *International Materials Reviews, 59*(3), 132-158.

Jovid, R., Timelli, G., & Bonollo, F. (2016). The Effect of Transition Elements on High-Temperature Mechanical Properties of Al-Si Foundry Alloys: A

Review. *Advanced Engineering Materials, 18*(7), 1096-1105.

Kasprzak, W., Kierkus, C. A., Kierkus, W. T., Sokolowski, J. H., Kasprzak, M., & Evans, W. J. (2001). The Structure and Matrix Microhardness of the 319 Aluminum Alloy After Isothermal Holding During the Solidification Process. *American Foundry Society*, 1-11.

Knipling, K.E., Dunand,D.C., & Seidman, D. (2007). Nucleation and Precipitation Strengthening in Dilute Al-Ti and Al-Zr Alloys. *Minerals Metals and Materials Society*, 2552-2563.

Kim, H. Y., Park, T. Y., Han, S. W., & Lee, H. M. (2006). Effects of Mn on the Crystal Structure of α-Al(Mn, Fe)Si Particles in A356 Alloys. *Journal of Crystal Growth*, 207-211.

Some Aspects of Dendritic Growth in Binary Alloys: Study of the Aluminium Copper System. *Transactions of the Metallurgical Society of AIME, 245*, 309-318.

Lados, D. A., Apelian, D., & Wang, L. (2011). Aging Effects on Heat Treatment Response and Mechanical Properties of Al-(1 to 13 pct)SiMg Cast Alloys. *Metallurgical and Materials Transactions B, 42*(1), 181-188.

Li, Y., Yang, Y., Wu, Y., Wei, Z., & Liu, X. (2011). Supportive Strengthening Role of Cr-rich Phase on Al-Si Multicomponent Piston Alloy at Elevated Temperature. *Materials Science and Engineering A, 528*(13-14), 4427-4430.

Li, Z., Samuel, A., Samuel, F., Ravindran, C., & Valtierra, S. (2003). Effect of Alloying Elements on the Segregation and Dissolution of CuAl2 Phase in Al-Si-Cu 319 Alloys. *Journal of Material Science, 38*, 1203-1218.

Long, H., Chen, J., Liu, C., Li, D., & Li, Y. (2013). The Negative Effect of Solution Treatment on the Age Hardening of A356 Alloy. *Materials Science and Engineering A*, 112-118.

Ma, S. (2006). *A Methodology to Predict the Effects of Quench Rates on Mechanical Properties of Cast Aluminum Alloys.* (Phd thesis). Worcester Polytechnic Institute. Worcester, Massachusetts. US.

Majed, J., & C. Torbjörn (2005). Effect of Titanium Additions on the Microstructure of DC-Cast Aluminium Alloys. *Materials Science and Engineering A, 413*, 277-282.

Mattos, J., Uehara, A., Sato, M., & Ferreira, M. (2010). Fatigue Properties and Micromechanism of Fracture of an AlSiMg0.6 Cast Alloy Used in Diesel Engine Cylinder Head. *Procedia Engineering 2*, 759-765.

Mazahery, A., & Shabani, M. O. (2014). Modification Mechanism and Microstructural Characteristics of Eutectic Si in Casting Al-Si Alloys: A Review on Experimental and Numerical Studies. Minerals, Metals & *Materials Society, 66*(5), 726-738.

Mbuya, T. O. (2011). *Analysis of Microstructure and Fatigue Micromechanisms in Cast Aluminium Piston Alloys.* (Phd thesis). University of Southampton. UK.

Meng, Y., Cui, J., Zhao, Z., & Zuo, Y. (2013). Effect of Vanadium on the Microstructure and Mechanical Properties of an Al-Mg-SiCu-Cr-Ti Alloy of 6xxx Series. *Journal of Alloys and Compounds, 573*, 102-111.

Mohamed, A., & Samuel, F. (2012). A Review on the Heat Treatment of Al-Si-Cu / Mg Casting Alloys. *Heat Treatment*, 55-72.

Mohamed, A., Samuel, F., & Kahtani, S. A. (2013). Microstructure, Tensile Properties and Fracture Behavior of High Temperature Al-Si-Mg-Cu Cast Alloys. *Materials Science and Engineering A, 577*, 64-72.

Mose, B. R. (2009). *Effect of Minor Elements on Castability, Microstructure and Mechanical Properties of Recycled Aluminium Alloys.* (PhD thesis). Jomo Kenyatta University of Agriculture and Technology. Nairobi. Kenya.

Murty, B. S., Kori, S. A., & Chakraborty, M. (2002). Grain refinement of Aluminium and its Alloys by Heterogeneous Nucleation and Alloying. International *Materials Reviews, 47*(1), 3-29.

M.Zamani (2015). A*l-Si Cast Alloys-Microstructure and Mechanical Properties at Ambient and Elevated Temperature.* (Licentiate thesis). Jönköping University. Jönköping. Sweden.

Ngigi, N. T. (2018). *Effect of Transition Elements on Microstructure and Mechanical Properties of Secondary Al-7Si-Mg Cast Aluminium Alloy.* (Masters thesis). University of Nairobi. Nairobi. Kenya.

Nicoletto, G., Anzelotti, G., & Konecna, R. (2010). Xray Computed Tomography vs. Metallography for Pore Sizing and Fatigue of Cast Al-alloys. *Procedia Engineering 2*, 547-554.

Paray, F., & Gruzleski, J. (1993). Modification - A Parameter to Consider in the Heat Treatment of Al-Si Alloys. *Cast Metals*, 187-198.

Pelayo, G., Sokolowski, J. H., & Lashkari, R. (2009). A Case Based Reasoning aluminium thermal analysis platform for the prediction of W319 Al cast component characteristics. *Journal of Achievements in Materials and Manufacturing Engineering, 36*(36), 7-17.

Pollak, R. D. (2005). *Analysis of Methods for Determining High Cycle Fatigue Strength of a Material with Investigation of Ti-6Al-4V Gigacycle Fatigue Behavior.* (Phd dissertation). Air Force Institute of Technology Air. Colorado. US.

Prasada Rao, A. K. (2011). Influence of Vanadium on the Microstructure of A319 Alloy. *Transactions of the Indian Institute of Metals, 64*(4-5), 447-451.

Qasim, Z., Jabbar, M., & Hassan, J. (2017). Enhancement the Mechanical Properties of Aluminum Casting Alloys (A356) by Adding Nanorods Structures from Zinc Oxide. *Journal of Material Sciences and Engineering, 4*(6), 1-8.

Wang, Q.G., & Davidson, C. (2001). Solidification and Precipitation Behavior of Al-Si-Mg Casting Alloys. *Journal of Materials Science, 36*, 739-750.

Ragab, K. A., Samuel, A. M., Al-Ahmari, A. M., Samuel, F. H., & Doty, H. W. (2011). Influence of Fluidized Sand Bed Heat Treatment on the Performance of Al-Si Cast Alloys. *Materials and Design, 32*(3), 1177-1193.

Rambabu, P., Prasad, N. E., Kutumbarao, V.V. & Wanhill, R.J.H (2017). Aerospace Materials and Material Technologies. N. Eswara Prasad and R.J.H. Wanhill (Eds.). *Aluminium Alloys for Aerospace Applications* (pp.29-52). Springer Science+Business Media. Singapore.

Rana, R. S., Purohit, R., & Das, S. (2012). Reviews on the Influences of Alloying elements on the Microstructure and Mechanical Properties of Aluminum Alloys and Aluminum Alloy Composites. *International Journal of Scientific and Research Publications, 2*(6), 1-7.

Rao, A. K. P., Murty, B. S., Das, K., & Chakraborty, M. (2008). On the Modification and Segregation Behavior of Sb in Al-7Si Alloy During Solidification. *Materials Letters, 62*, 273-275.

Gowri, S., & Samuel, F. (1994). Effect of Alloying Elements on the Solidification Characteristics and Microstructure of Al-Si-Cu-Mg-Fe 380 Alloy. *Metallurgical and Materials Transactions A, 25A*, 437-448.

Shaha, S. K., Czwerwinski, F., Kasprzak, W., Friedman, J., & Chen, D. L. (2015). Ageing Characteristics and High-Temperature Tensile Properties of Al-SiCu-Mg Alloys with Micro-additions of Cr, Ti, V and Zr. *Materials Science and Engineering A*. 652.

Saheb, N., Laoui, T., Daud, A. R., Harun, M., Radiman, S., & Yahaya, R. (2001). Influence of Ti Addition on Wear Properties of Al-Si Eutectic. *Wear, 249*(8), 656-662.

Samuel, F. H., Ouellet, P., Samuel, A. M., & Doty, H. W. (1998). Effect of Mg and Sr Additions on the Formation of Intermetallics in AI-6 Wt Pet Si-3.5 Wt Pet Cu-(0.45) to (0.8) Wt Pet Fe 319-Type Alloys. *Metallurgical and Materials Transactions A, 29A*(12), 2871-2884.

Shaha, S., Czerwinski, F., Kasprzak, W., Friedman, J., & Chen, D. (2015). Low Cycle Fatigue of Aluminium-Silicon Alloys for PowerTrain Applications. *Minerals, Metals & Materials Society*, 999-1006.

Shaha, S. K., Czerwinski, F., Kasprzak, W., Friedman, J.,& Chen, D. L. (2014). Thermal Stability of (AlSi)x(ZrVTi) Intermetallic Phases in the Al-Si-Cu-Mg Cast Alloy with Additions of Ti, V, and Zr. *Thermochimica Acta*, 595, 11-16.

Shaha, S. K., Czerwinski, F., Kasprzak, W., Friedman, J., & Chen, D. L. (2015). Monotonic and Cyclic Deformation Behavior of the Al-Si-Cu-Mg cast Alloy with Micro-additions of Ti, V and Zr. *International Journal of Fatigue, 70*, 383-394.

Shivkumar, S., Jr., S. R., & Apelian, D. (1990). Influence of Solution Parameters and Simplified Supersaturation Treatment on Tensile Properties of A356 Alloy. *AFS Transactions*, 913-922.

Sigworth, G. (2011). Understanding Quality in Aluminum Castings. *American Foundry Society*, 1-17.

Sigworth, G., & Kuhn, T. (2007). Grain Refinement of Aluminum Casting Alloys. *International Journal of Metalcasting, 1*(1), 31-40.

Sjölander, E. (2011). *Heat Treatment of Al-Si-Cu-Mg Casting Alloys.* (Phd Thesis). Jönköping University. Jönköping. Sweden.

Sjolander, E., & Seifeddine, S. (2010). The Heat Treatment of Al-Si-Cu-Mg Casting Alloys. *Journal of Materials Processing Technology, 210*(10), 1249-1259.

Sreeja Kumari, S. S., Pillai, R. M., Rajan, T. P., & Pai, B. C. (2007). Effects of Individual and Combined Additions of Be, Mn, Ca and Sr on the Solidification Behaviour, Structure and Mechanical Properties of Al-7Si-0.3Mg-0.8Fe Alloy. *Materials Science and Engineering A, 460-461*, 561-573.

Struers website. *Struers: Knowledge.* Retrieved from http://www.struers.com/en/knowledge.

Sundman, B., Jansson, B., & Andersson, J. (1985). CALPHAD (Calculation of Phase Diagrams): A Comprehensive Guide. *Elsevier Science*, 153-190.

Tagirov, D., Lashina, E., & Kaibyshev, R. (2012). Effect of Liquid Hot Isostatic Pressing on Structure and Mechanical Properties of Aluminium Gravity Die Castings. *Materials Science Forum*, 706-709.

Tajiri, A., Nozaki, T., Uematsu, Y., Kakiuchi, T., Nakajima, M., Nakamura, Y., & Tanaka, H. (2014). Fatigue Limit Prediction of Large Scale Cast Aluminum Alloy A356. *Procedia Materials Science, 3*, 924-929.

Tamminen, J. (1988). *Thermal Analysis for Investigation of Solidification Mechanisms in Metals and Alloys.* (Phd thesis). University of Stockholm. Sweden.

Tillová, E., Chalupová, M., & Hurtalová, L. (2012). *Evolution of Phases in a Recycled Al-Si Cast Alloy During Solution Treatment*: Scanning Electron Microscopy. (Dr. viache ed.). Slovak Republic.

Tiryakioglu, M. (2008). Statistical Distributions for the Size of Fatigue-Initiating Defects in Al-7%Si-0.3%Mg Alloy Castings: A Comparative Study. *Materials Science and Engineering A, 497*(1-2), 119-125.

T.O.Mbuya (2011). *Analysis of Microstructure and Fatigue Micromechanisms of Cast Aluminum Piston Alloys.* (Phd thesis). University of Southampton. UK.

Mbuya, T.O., Odera, B.O., & S.P.Ng'ang'a (2003). Inuence of Iron on Castability and Properties of Aluminium Silicon alloys: literature review. *International Journal of Cast Metals Research, 16*(5), 451-465.

Wang, Q. G. (2003). Microstructural Effects on the Tensile and Fracture Behavior of Aluminum Casting Alloys A356 / 357. *Metallurgical and Materials Transactions A, 34A*, 2887-2899.

Wang'ombe, D., Maranga, S., Mose, B., & Mbuya, T. (2017). The Status of Kenyan Aluminum Recycling Industry. *Sustainable Research and Innovation Conference*, 194-199.

Xu-gang, D., Jie, Z., Yao-Jun, J., & Bin, L. (2012). Effect of Alloying on High Temperature Fatigue Performance of ZL114A(Al-7Si) Alloy. *Transaction of Non-ferrous Metals society of China, 22*, 661-667.

Yang, Y., Zhong, S.-Y., Chen, Z., Wang, M., Ma, N., & Wang, H. (2015). Effect of Cr Content and Heat-Treatment on the High Temperature Strength of Eutectic Al-Si Alloys. *Journal of Alloys and Compounds, 647*, 63-69.

Yoshida, K., & Arrowood, R. (1995). Microstructure and Mechanical Properties of A356 Aluminum Castings as Related to Various T6-Type Heat Treatments, in Light Weight Alloys for Aerospace Application III. *The*

Minerals, Metals, and Materials Society, 77-87.

Zamani, M. (2015). *Al-Si Cast Alloys-Microstructure and Mechanical Properties at Ambient and Elevated Temperature.* (Licentiate thesis). Jönköping University. Sweden.

Cordero, Z.C., Knight, B.E., & Schuh, C.A. (2016). Six Decades of the Hall-Petch Effect - a Survey of Grain-size Strengthening Studies on Pure Metals. *International Materials Reviews, 61* (8), 495-512.

Zhang, D., & Zheng, L. (1996). The Quench Sensitivity of Cast Al-7Wt Pet Si-0.4 Wt pct Mg Alloy. *Metallurgical and Materials Transactions A, 27*, 3983-3991.

APPENDICES

Appendix I. Sample calculation of the amount of master alloy to be added to the 356 base alloy ingot

$$Weight\ of\ master\ alloy\ to\ be\ added = \frac{(\%\ of\ additive\ desired) * (Weight\ of\ melt)}{\%\ of\ element\ in\ master\ alloy} \tag{5.1}$$

Weight of master alloy + Weight of ingot = Weight of melt
Weight of master alloy = 50 % Cu * g (Where "g" is the weight in Kgs of the Cu - master alloy)
Weight of ingot = Amount of Cu in the base alloy * Weight of the ingot = 0.09 % Cu * 4.3 Kg
Weight of melt = Weight of the melt within the crucible capacity (4.5 Kg in this case) * Amount of Cu desired = 4.5 Kg * 3.5 % Cu

Thus, (50 % Cu * g)+ (0.09 % Cu * 4.3 Kg) = 4.5 Kg * 3.5 % Cu

$$g = \frac{((4.5Kg * 3.5\%Cu) - (0.09\%Cu * 4.3Kg))}{50\%Cu} = 0.30726Kg \tag{5.2}$$

Therefore, 0.30726 Kg of the Al-50 wt.% Cu should be added to the molten 356 base alloy to be able to obtain an alloy containing 3.5 % Cu

Appendix II. Identification of α-Al and Al-Si temperatures of an Al–Si–Cu alloy (Farahany et al., 2013)

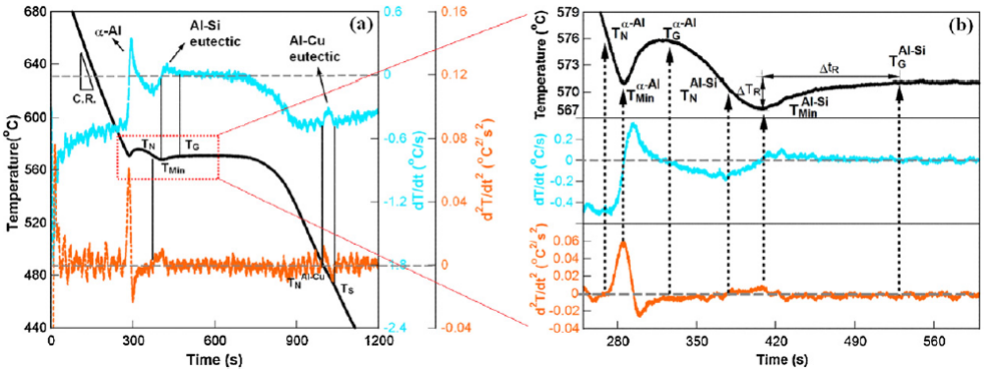

Figure I.1: Identification of α-Al and Al-Si temperatures of an Al–Si–Cu alloy (Farahany et al., 2013)

Appendix III. Illustration of identified dendrite coherency point for alloy AlSi8Cu2 (Djurdjevic et al., 2012)

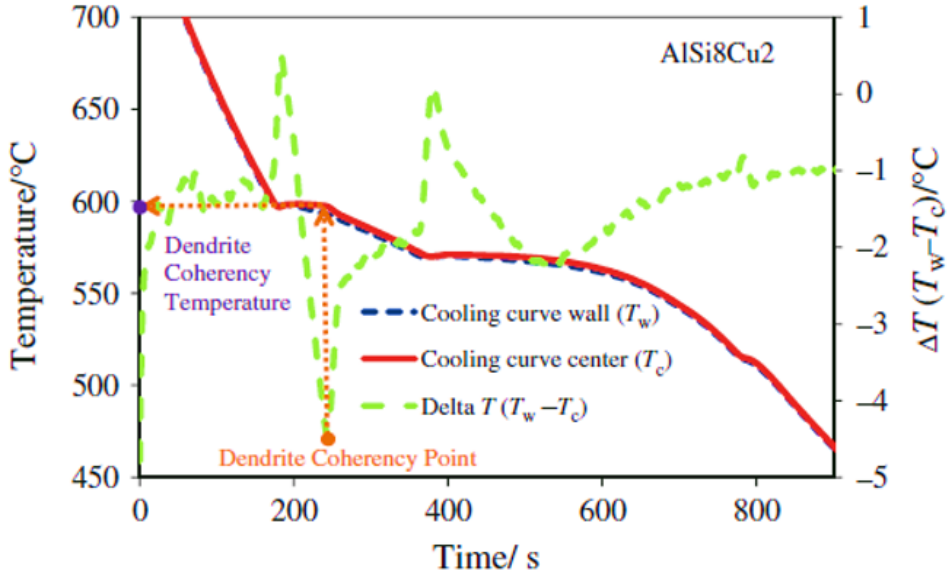

Figure II.1: Illustration of identified dendrite coherency point for alloy AlSi8Cu2 (Djurdjevic et al., 2012)

Appendix IV. Identification of Al-Si-Cu nucleation temperature for alloy Al-5Si-(1-4)Cu (Djurdjevic et al., 2014): (a) Trend identified in the cooling curve when Cu-phases are present at different Cu additions; (b) Identified Cu-rich phases in the $\frac{dT}{dt}$ vs. t curves

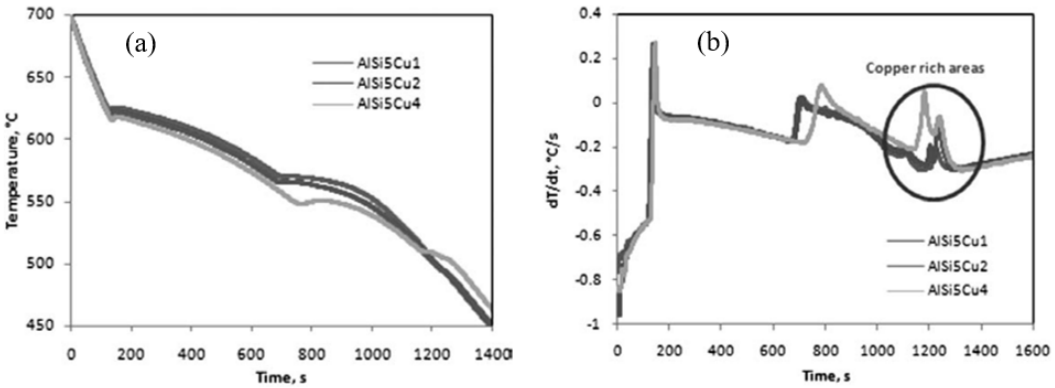

Figure III.1: Identification of Al-Si-Cu nucleation temperature for alloy Al-5Si-(1-4)Cu (Djurdjevic et al., 2014): (a) Trend identified in the cooling curve when Cu-phases are present at different Cu additions; (b) Identified Cu-rich phases in the $\frac{dT}{dt}$ vs. t curves

Appendix V. Identification of end of solidification region as a minimum on the first derivative curve (region around "TES") for alloy Al-6.5% Si (Barlow & Stefanescu, 2002)

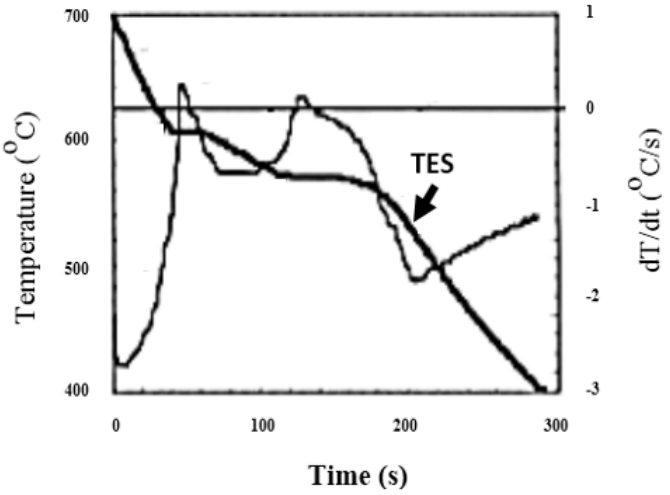

Figure IV.1: Identification of end of solidification region as a minimum on the first derivative curve (region around "TES") for alloy Al-6.5% Si (Barlow & Stefanescu, 2002)

Appendix VI. Sample identification of nucleation temperatures using alloy 356TiSr

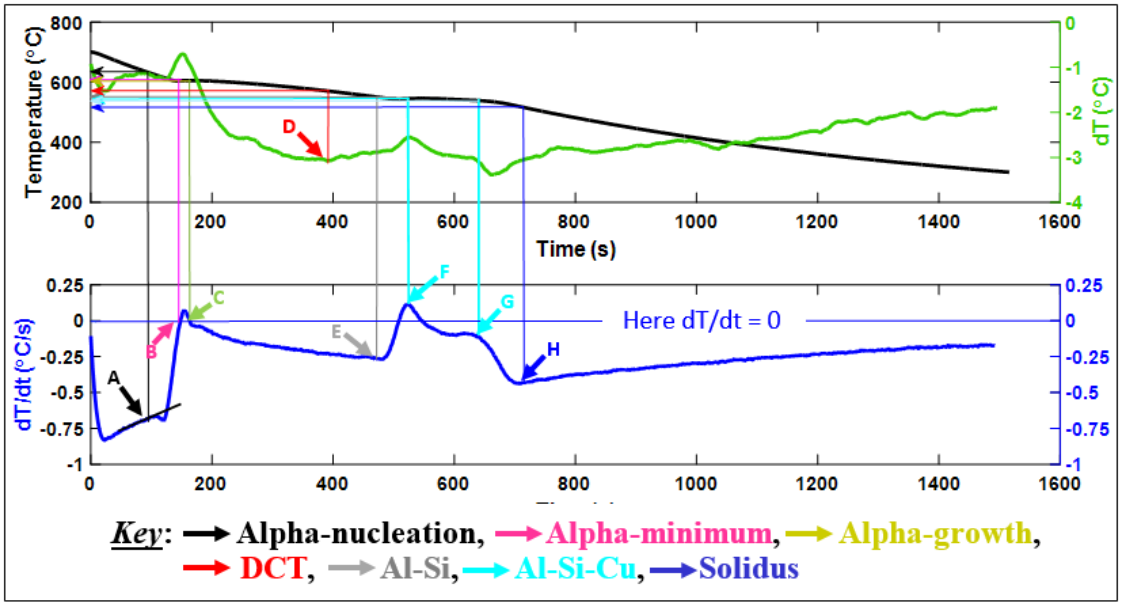

Figure VI.1: Sample identification of nucleation temperatures using alloy 356TiSr's cooling curve, $\frac{dT}{dt}$ vs. t curve and $\triangle$T vs. t curve

1. Beginning of solidification (α-Al phase)
   - α-Al dendrite nucleation temperature ($T_N{}^{\alpha\text{-Al}}$) – slope change in cooling curve and slight deviation from linearity of $\frac{dT}{dt}$ vs. t curve. (See point "A")
   - α-Al dendrite minimum temperature ($T_{Min}{}^{\alpha\text{-Al}}$) - a local min. on cooling curve, coincident with the first point where $\frac{dT}{dt} = 0$ (see point "B")
   - α-Al dendrite growth temperature - a local max. on cooling curve, 2nd point where $\frac{dT}{dt} = 0$ and came after $T_{Min}{}^{\alpha\text{-Al}}$ (see point "C")
2. The DCP/DCT - where $\triangle T = T_w - T_c = 0$ (see point "D")
3. Al-Si eutectic - point of sudden increase in $\frac{dT}{dt}$ vs t. (see point "E")
4. Cu-rich phases -1/2 peaks towards end of $\frac{dT}{dt}$ vs. t (see point "F" and "G")
5. Solidus - region closest to last distinct min. on $\frac{dT}{dt}$ curve and where tangent drawn on $\frac{dT}{dt}$ curve just begins to stabilize. (see point "H")

Appendix VII: Effect of addition of elements to alloy 356's solidification characteristic temperatures

Table VII.1: Effect of addition of elements to alloy 356's solidification characteristic temperatures

Phase Temp.	356	356X	356X – 356 (X)	356XCr	356XCr – 356 (XCr)	356X0.5CuCr	356X0.5CuCr - 356 (X0.5CuCr)	356X3.5CuCr	356X3.5CuCr – 356 (X3.5CuCr)	356TiSr	356TiSr – 356 (TiSr)	ZrV vs TiSr
α-Al nucl.	622.9	603.6	- 19.3	628.8	5.9	625.9	3	624.7	1.8	618.2	- 4.7	>- 4.7
α-Al min.	603.5	579.4	- 24.1	605.3	1.8	604.7	1.2	603.6	0.1	601.2	- 2.3	>- 2.3
α-Al growth	599.8	575.9	- 23.9	598.3	- 1.5	597.1	- 2.7	600.6	0.8	595.9	- 3.9	>- 3.9
DCT	593.5	578.1	- 15.4	589.5	- 4	584.2	- 9.3	593	- 0.5	591.2	- 2.3	>- 2.3
Al-Si	547.1	534.7	- 12.4	557.7	10.6	547.7	0.6	550	2.9	552.5	5.4	decreases
Al-Si-Cu	513.5	501	- 12.5	537.1	23.6	536.2	22.7	517.7	4.2	538.3	24.8	decreases
						530.6		511.8		526.5		
Solidus	482.6	474.1	- 8.5	508.8	26.2	510	27.4	496.5	13.9	510	27.4	decreases